PEN-ON-PAPER ELECTRONICS

BY

ANALISA RUSSO

DISSERTATION

Submitted in partial fulfillment of the requirements
for the degree of Doctor of Philosophy in Materials Science and Engineering
in the Graduate College of the
University of Illinois at Urbana-Champaign, 2014

Urbana, Illinois

Doctoral Committee:

Professor Jennifer A. Lewis, Chair
Professor Kenneth S. Schweizer
Professor Shen J. Dillon
Professor Ralph G. Nuzzo

ABSTRACT

Printed electronics constitute a class of electronic devices that are made by printing or etching conductive materials on a substrate. Printed circuit boards (PCBs) are typically made on rigid fiberglass sheets, however plastic and paper substrates have emerged as alternative materials that are flexible, lightweight, and disposable. To date, metallic and carbon-based features have been patterned by metal evaporation, sputter coating, inkjet printing, screen printing, or roll-to-roll transfer. Most methods either require sophisticated equipment or employ dilute inks that wet and spread on smooth plastics (resulting in poor resolution) or readily permeate paper (resulting in poor conductivity). There is a need for facile, inexpensive printing methods that yield conductive and resistive traces on flexible substrates. In this thesis, we develop two platforms for patterning conductive silver and resistive carbon inks for flexible electronics: (1) rollerball pen printing and (2) direct ink writing (DIW).

Conductive silver and resistive carbon particle-based inks are created for direct writing of flexible electronics. Specifically, a new silver ink is synthesized that enables printing of high conductivity features, approximately 1% of bulk silver, at ambient conditions. A complementary carbon nanoparticle ink is formulated that exhibits an electrical conductivity that is six orders of magnitude lower than the silver ink. The rheological properties of these inks can be widely tuned to facilitate uniform flow through commercial rollerball pens or printing of continuous filaments via direct writing. Both the solids loading and hydroxyethyl cellulose (HEC) content within these inks strongly influence their rheological and printing behavior. Importantly, by blending these two inks, we can form composite inks, whose electrical resistivity can be systematically varied over several orders of magnitude between $2\text{x}10^{-4}$ Ω-cm (pure silver ink) to 200 Ω-cm (pure carbon ink).

Pen-on-Paper electronics offers an inexpensive and intuitive approach to creating paper electronic devices. By filling commercial rollerball pens with conductive silver and resistive carbon inks, we can pattern functional features on low-cost substrates. Direct observation of the ink transfer during printing revealed that conductive silver dispensed from rollerball pen inks undergo a well known printers instability, in which the trailing edge of the ink breaks up into two fin-like meniscuses, above a critical printing speed. We find that a balance between viscous and surface forces determines the meniscus shape and corresponding printed line morphology; specifically, this transition occurs at $Ca \sim 0.1$. The influence of the paper substrate on printed line morphology is also investigated. Semi-gloss photo paper provides a unique writing surface, in which solvent is rapidly wicked through a microporous plastic film, pinning the edges of the printed ink traces and preventing ink spreading. In this study, semi-gloss photo paper is used as a model surface for ink printing dynamics. We demonstrate multiple examples of Pen-on-Paper electronic devices, including electronic art, analog filters, tactile and visual user interfaces, and a paper Arduino circuit board (i.e., Paperduino) printed using an inexpensive desktop pen plotter.

To create novel photovoltaic devices, silver interconnects and busbars are printed onto glass and polyimide substrates (6 diameter) that are populated with an array of InGaP micro solar cells by direct writing a concentrated silver ink. We introduce an optical profilometry method to map the topography of the complex surface and dynamically adjust the height of the printing nozzle to within 15 ± 5 μm of the surface during printing. The flexible polyimide PV devices are thermally annealed at 175°C for 30 minutes, yielding silver traces with conductivity 2.5x10^{-5} Ω-cm. The PV cell current-voltage (I-V) response is analogous to measurements performed on cells wired with evaporated gold interconnects, confirming the quality of our printed silver features. This research opens new avenues for patterning low-cost, flexible electronics for applications ranging from science education to advanced technologies.

ACKNOWLEDGMENTS

I would like to acknowledge my advisor, Jennifer Lewis, for allowing me to pursue a research topic that I am passionate about and for guiding me towards developing P-o-P electronics in two directions: as an educational tool and as a fascinating area of research.

I would like to express my appreciation for my thesis committee, Kenneth Schweizer, Shen Dillon, and Ralph Nuzzo for their valuable insights and guidance for my proposed and completed research.

I would also like to acknowledge Lewis Group members past and present. I feel fortunate to have been part of such an energetic, compassionate, and collaborative group. I am particularly appreciative of Bok Yeop Ahn for his invaluable guidance on conducting research, Ashley Gupta for her kindness, creativity, and hard work, Thomas Ober for his in-depth discussion on fluid dynamics, Michael Bell for sharing his knowledge of PCB fabrication, and Scott Slimmer for his consistent help and advice.

I would also like to thank my parents, Ralph and Mary Russo, for their constant encouragement while I pursued my PhD and for our visits between Urbana and Iowa City. Finally, I would like to thank my brother, Peter, for his support since day one. Not only has his engineering career been an inspiration for me, he also challenges me to be confident, creative, and ambitious.

TABLE OF CONTENTS

CHAPTER 1

INTRODUCTION

Printed electronics are an emerging class of electronic devices that are finding widespread application in thermochromic displays[1], radio frequency identification (RFID) tags,[2–4] and batteries.[5–8] Plastic and paper substrates have recently emerged as new substrate materials that are flexible, lightweight, and disposable. Paper is a particularly versatile platform given the wide variety of paper compositions, coatings, and textures, which be exploited to achieve specific functions in flexible electronics. For example, highly absorbent paper is suitable for disposable microfluidic and diagnostic devices[9–12] and cell cultures,[13] whereas smooth photo-quality paper or plastic-coated films are used for colored electrowetting pixels.[14]

To date, metallic and carbon-based traces and contacts have been patterned on by metal evaporation[1], sputter coating, inkjet printing[2, 15], screen printing[16], or roll-to-roll transfer[17]. However, these methods have many disadvantages for printing on heat-sensitive and porous substrates like plastic and paper. For example, many of these deposition methods employ dilute inks that readily permeate paper, resulting in poor conductivity. Nanoparticle inks, such as those used in inkjet printing, typically require thermal annealing (>150°C) to enhance conductivity, which can degrade paper or polymer substrates. Hence, new ink designs coupled with facile, inexpensive printing methods for patterning conductive and resistive traces on flexible paper and plastic substrates are needed.

1.1 Thesis Scope

The aim of my PhD research is to develop functional inks and low-cost patterning tools for creating flexible electronic devices. Particle-based conductive silver and resistive carbon inks are produced for both rollerball pen printing and DIW. The silver ink is used to print the

primary circuit traces, while the carbon ink enables direct patterning of resistive elements on flexible substrates. In addition, these inks can be mixed to create composite inks whose electrical conductivity can be tuned over six orders of magnitude.

We introduce a new class of flexible electronics produced by rollerball pen drawing of conductive silver and resistive carbon inks, known as Pen-on-Paper Electronics. We developed a fundamental understanding of the ink properties required to print uniform, conductive traces from silver ink-filled rollerball pens mounted to a robotic stage that is translated at different printing speeds. The shape of the trailing ink meniscus is imaged using a high-magnification camera. We find that high ink viscosity paired with high printing rates results in the breakup of the trailing ink trace into a double meniscus, akin to the well known printers instability [18, 19]. Several examples of this new class of pen-drawn paper electronics are created to demonstrate the power of this approach, including electronic art, programmable LED displays and capacitive touch sensors, antennas, and high and low pass filters (which include resistors printed from the carbon ink).

We also design a more concentrated silver ink for direct ink writing (DIW). Using this approach, we pattern silver interconnects and bus bars over an sparse array of photovoltaic micro cells on flexible polyimide sheets. The inherently contoured surface of the PV array poses a significant challenge for printing fine circuit traces, because the ink deposition nozzle must be translated at a constant fly height over the substrate. To achieve this, we first mapped the topography of the plastic film via optical profilometry and then used this data to dynamically adjust the nozzle height during printing. This approach yielded high-resolution conductive traces whose electrical performance matches that of evaporated gold interconnects.

1.2 Thesis Organization

In Chapter 2, a literature review is presented that focuses on conductive silver inks, carbon-based resistive inks, and relevant printing and annealing methods. In Chapter 3 the design, rheology, and electrical properties of conductive silver inks, resistive carbon inks, and their composite blends are described. In Chapter 4, a new class of flexible electronic devices

known as Pen-on-Paper electronics is reported. We elucidate the ink properties and printing conditions required to create uniform traces using function ink-filled rollerball pens and avoid the well known printer instability that leads to double meniscus formation. Several device embodiments, including programmable Pen-on-Paper devices are highlighted. In Chapter 5, direct ink writing of conductive silver interconnects for photovoltaic microcell arrays that are sparsely populated on polyimide is presented. Finally, the key conclusions of my PhD thesis are summarized in Chapter 6.

1.3 References

[1] Adam C. Siegel, Scott T. Phillips, Benjamin J. Wiley, and George M. Whitesides. Thin, lightweight, foldable thermochromic displays on paper. *Lab on a Chip*, 9(19):2775–2781, October 2009.

[2] A Rida, Li Yang, R. Vyas, and M.M. Tentzeris. Conductive inkjet-printed antennas on flexible low-cost paper-based substrates for RFID and WSN applications. *IEEE Antennas and Propagation Magazine*, 51(3):13–23, June 2009.

[3] Li Yang, Amin Rida, and Manos M. Tentzeris. Design and development of radio frequency identification (RFID) and RFID-enabled sensors on flexible low cost substrates. *Synthesis Lectures on RF/Microwaves*, 1(1):1–89, January 2009.

[4] Katherine Bourzac. Bringing graphene to market, August 2009.

[5] Gustav Nystrm, Aamir Razaq, Maria Strmme, Leif Nyholm, and Albert Mihranyan. Ultrafast all-polymer paper-based batteries. *Nano Letters*, 9(10):3635–3639, October 2009.

[6] Nicole K. Thom, Gregory G. Lewis, Matthew J. DiTucci, and Scott T. Phillips. Two general designs for fluidic batteries in paper-based microfluidic devices that provide predictable and tunable sources of power for on-chip assays. *RSC Advances*, 3(19):6888–6895, April 2013.

[7] Qian Cheng, Zeming Song, Teng Ma, Bethany B. Smith, Rui Tang, Hongyu Yu, Hanqing Jiang, and Candace K. Chan. Folding paper-based lithium-ion batteries for higher areal energy densities. *Nano Letters*, 13(10):4969–4974, October 2013. WOS:000326356300061.

[8] Thu H. Nguyen, Arwa Fraiwan, and Seokheun Choi. Paper-based batteries: A review. *Biosensors & Bioelectronics*, 54:640–649, April 2014. WOS:000333071500096.

[9] Andres W. Martinez, Scott T. Phillips, Benjamin J. Wiley, Malancha Gupta, and George M. Whitesides. FLASH: A rapid method for prototyping paper-based microfluidic devices. *Lab on a Chip*, 8(12):2146–2150, 2008. WOS:000261686200020.

[10] Andres W. Martinez, Scott T. Phillips, Zhihong Nie, Chao-Min Cheng, Emanuel Carrilho, Benjamin J. Wiley, and George M. Whitesides. Programmable diagnostic devices made from paper and tape. *Lab on a Chip*, 10(19):2499–2504, September 2010.

[11] Audrey K. Ellerbee, Scott T. Phillips, Adam C. Siegel, Katherine A. Mirica, Andres W. Martinez, Pierre Striehl, Nina Jain, Mara Prentiss, and George M. Whitesides. Quantifying colorimetric assays in paper-based microfluidic devices by measuring the transmission of light through paper. *Analytical Chemistry*, 81(20):8447–8452, October 2009.

[12] Andres W. Martinez, Scott T. Phillips, and George M. Whitesides. Three-dimensional microfluidic devices fabricated in layered paper and tape. *Proceedings of the National Academy of Sciences of the United States of America*, 105(50):19606–19611, December 2008. WOS:000261802300009.

[13] Ratmir Derda, Sindy K. Y. Tang, Anna Laromaine, Bobak Mosadegh, Estrella Hong, Martin Mwangi, Akiko Mammoto, Donald E. Ingber, and George M. Whitesides. Multizone paper platform for 3d cell cultures. *PLoS ONE*, 6(5):e18940, May 2011.

[14] Duk Young Kim and Andrew J. Steckl. Electrowetting on paper for electronic paper display. *ACS Applied Materials & Interfaces*, 2(11):3318–3323, November 2010.

[15] Yoshihiro Kawahara, Steve Hodges, Benjamin S. Cook, Cheng Zhang, and Gregory D. Abowd. Instant inkjet circuits: Lab-based inkjet printing to support rapid prototyping of UbiComp devices. In *Proceedings of the 2013 ACM International Joint Conference on Pervasive and Ubiquitous Computing*, UbiComp '13, pages 363–372, New York, NY, USA, 2013. ACM.

[16] Kamran ul Hasan, Omer Nur, and Magnus Willander. Screen printed ZnO ultraviolet photoconductive sensor on pencil drawn circuitry over paper. *Applied Physics Letters*, 100(21):211104, 2012.

[17] Jolke Perelaer, Robert Abbel, Sebastian Wnscher, Robin Jani, Tim van Lammeren, and Ulrich S. Schubert. Roll-to-roll compatible sintering of inkjet printed features by photonic and microwave exposure: From non-conductive ink to 40% bulk silver conductivity in less than 15 seconds. *Advanced Materials*, 24(19):2620–2625, May 2012.

[18] L.H. Pan and J.R. Debruyn. Broken-parity waves at a driven fluid-air interface. *Physical Review Letters*, 70(12):1791–1794, March 1993.

[19] R. L. Santos, U. Agero, and J. M. A. Figueiredo. Pattern dynamics in a perturbed printer's instability experiment. *Physical Review. E, Statistical, Nonlinear, and Soft Matter Physics*, 77(6 Pt 2):066310, June 2008.

CHAPTER 2

LITERATURE REVIEW

2.1 Introduction

This chapter begins with a review of recent advances in conductive silver and resistive carbon inks. Next, strategies for annealing silver inks to create highly conductive features are presented. Finally, methods for the production of printed flexible electronics and their applications are discussed.

2.2 Conductive Inks

Particle-based conductive inks enable flexible electronics to be patterned on plastic or paper substrates via techniques such as roll-to-roll[1], screen printing[2], and inkjet printing[3]. Silver particle inks are of particular interest, because silver possesses the highest conductivity of any metal (6.3×10^5 S/cm) and it is highly stable to oxidation, enabling annealing in air. Myriad silver particle sizes and shapes as well as post-processing techniques have been employed to ensure high conductivity traces. To date, three types of conductive silver inks have been reported: (1) nanoparticle inks, (2) anisotropic particle inks, and (3) particle-free precursor inks. Each ink type has advantages and disadvantages for in printed electronics, as described below.

2.2.1 Silver Nanoparticle Inks

Nanoparticle inks are suitable for fine-scale printing by inkjet or direct-write extrusion through fine nozzles (<100 μm diameter), where the use of nanoparticles is preferred over larger particles that may clog these printheads. A common method for creating uniform

silver nanoparticles in water is the polyol method. In this route, heated ethylene glycol acts as both a solvent and a reducing agent for silver nitrate ($AgNO_3$), while polyvinylpyrrolidone (PVP) is used as a capping agent.[4–6] This process yields silver particles with diameters below 100 nm. In general, the silver particle size increases with $AgNO_3$ concentration in the reaction vessel and decreases with increasing PVP concentration. The role of PVP in the synthesis is two-fold: PVP provides nucleation sites for particle formation (increased concentration leads to a higher number of small particles) and it acts as a capping agent that limits particle growth.[7] It has also been reported that higher ethylene glycol temperature leads to larger particles, on average: generally, the increased mobility of silver atoms at the surface of the particles at high temperature increases the probability of particle coalescence, and particles as large as 50 nm have been produced.[6]

Carboxylic acid-based species have also been widely used as capping agents to stabilize the formation of silver nanoparticles in water. One representative process involves injecting trisodium citrate into a heated aqueous solution of silver nitrate. A typical resulting particle size is 40 nm.[8] Prior work by Ahn, *et al.* has built on the concept of carboxylic acid capping agents by employing long-chain polyacrylic acid (PAA). The initial silver particle size is quite small (<10 nm), but can be increased via a ripening process at elevated temperature. In its concentrated state, this ink is well suited for direct ink writing (DIW) a continuous filamentary printing approach in which inks are extruded through microscale nozzles (**Figure 2.1a**). As the ink dries after printing, the continuous ink filaments become increasingly stiff. As such, a filament can span gaps of several millimeters in the underlying substrate as well as create vertical features without buckling. However, the high polymer content (10% by weight) disrupts percolation between the silver nanoparticles and yields ink that is highly resistive after printing and drying at room temperature. Annealing temperatures in excess of 250°C are required to decompose the PAA binder and initiate particle sintering.[9] A plot of ink resistivity as a function of annealing time at different temperatures is shown in **Figure 2.1b**.

2.2.2 Anisotropic Silver Particle Inks

The use of anisotropic silver particles may enable higher conductivity. First, there is a reduced percolation threshold required for high aspect ratio particles compared to spherical particles, which improves conductivity even in inks with low solids loading. Second, the contact area between high aspect ratio particles is larger than those between spherical particles, thus facilitating current flow between adjacent particles.[10–12]

The polyol reduction method, previously described, is typically used to create anisotropic silver microwires and nanorods in water. Extensive work done by Xia, *et al.*, has elucidated the role of PVP and chloride ions in the growth of anisotropic particles.[13, 14] First, the reduction of silver ions to silver atoms in ethylene glycol results mostly in nuclei with a 5-fold twinned decahedron shape. As the particles grow in size, PVP interacts most strongly with the {100} facet of the crystal, passivating the nanorod surfaces thereby promoting growth at the bare ends. The presence of chloride ions stabilizes the initial silver seeds, providing an opportunity for anisotropic growth rather than rapid aggregation that favors the formation of spherical particles.[14] By carefully controlling the $AgNO_3$, PVP, and salt concentrations as well as the reaction temperature and time, the length and diameter of the silver rods can be tuned over a broad range. Generally, lower temperatures slow the reaction kinetics, enabling the formation of larger diameter rods (maximum of 70 nm at 130°C and 50 nm at 160°C). At longer reaction times, the rod length increases; lengths as high as 25 μm are observed after reacting at 130°C for 11 h.[15] One emerging application for silver microwires is transparent conductive films, which take advantage of their low percolation threshold. In this application, a sparse network of silver microwires maintains electrical conductivity across a large area yet is porous enough to transmit up to 90% of incident light.[12, 16–19] A micrograph of silver microwires and a transparent conductive film created by Meyer rod spreading is shown in **Figure 2.2a-b**.

Silver flakes are another widely used form of anisotropic particles.[11, 20–22] They are produced by ball milling spherical particles. Upon impact, ductile metal particles flatten into flakes with diameters that are 10s of microns wide with sub-micron thicknesses.[11] The sheet resistance of printed films decreases as the surface area of the constituent flakes

increases.[11] In addition to their high conductivity, silver flake-based inks are highly shear thinning since the individual particles align in the direction of fluid flow. These properties make them well suited for screen printing applications. A representative image of silver flakes and the corresponding sheet resistance of a conductive silver flake ink used in screen printing are provided in **Figure 2.2c-d**.[11]

2.2.3 Particle-Free Reactive Inks

Several silver precursor-based inks have been developed, which are particle-free prior to printing. During printing, particle nucleation ensues leading to a particle-based trace that requires sintering. Due to a lack of discrete particles, these traces have a thin, smooth morphology. For example, Xerox created a precursor ink composed of silver acetate mixed with a weak reducing agent, ethanolamine, that is stabilized by caprylic acid. Upon heating to modest temperatures (∼150°C), the reducing agent and acid complex break down, enabling formation of a conductive silver film that is approximately 10% as conductive as bulk silver.[23]

Walker and Lewis recently created a new type of reactive silver ink based on a modified Tollens reagent.[24] This ink, which has a significantly longer shelf life than previously reported precursor inks, contains silver acetate dissolved in aqueous ammonium hydroxide with formic acid. Upon printing, silver particles precipitate onto the substrate surface and coalesce. After drying at room temperature, the conductivity of the printed traces is approximately 10% of the conductivity of bulk silver. However, upon annealing the traces to 90°C, they achieve approximately 90% bulk silver conductivity. These inks possess low viscosity (∼2-4 mPa-s) making them suitable for inkjet printing, spray coating, and even meniscus-based deposition through ultrafine 100 nm diameter nozzles. An image of silver electrodes spray coated through a shadow mask onto ethyl vinyl acetate (EVA) is shown in **Figure 2.3**.[24]

2.3 Annealing Methods

Most silver particle-based inks require thermal or photonic annealing to increase the electrical conductivity of as-printed traces. Thermal annealing at elevated temperatures of 150-550°C is the most common approach. However, this method is not suitable for inks printed on flexible paper and plastic substrates, which tend to soften or degrade at the low end of this range. To enable the use of low-cost substrates, alternative methods such as photonic annealing can be used. An additional approach that has recently emerged involves self-sintering aided by chemical interactions with the substrate.

2.3.1 Thermal Annealing

During thermal annealing, several mechanisms occur that enhance the electrical conductivity of printed silver traces. First, residual solvent is removed from the ink. Second, organic capping agents are degraded and volatilized. Finally, particle sintering occurs.[25, 26] For example, silver nanoparticle inks with high PAA content are not conductive after printing and drying at room temperature. However, upon heating to 250°C, the printed traces achieve a conductivity that is 1% of silver, and they achieve nearly bulk silver conductivity after annealing at 550°C where polymer removal is completed and the silver particle network has achieved high density. Due to these constraints, these inks can only be used on substrates such as glass and silicon that can withstand high temperatures.[9]

2.3.2 Photonic Annealing

Photonic annealing has recently emerged as an alternative annealing approach, especially for high throughput methods such as roll-to-roll printing. It is of significant interest for printed electronics, because it allows conductive traces to be rapidly heated locally without affecting the underlying substrate.[27–33] Specifically, the conductive features are flash exposed to a high intensity ($\sim$1 J/cm^2) broadband light source. The conductive material reaches temperatures near 1000°C for short durations ($\sim$0.001 s).[31, 32] This method is well suited for substrates, such as plastic or paper, that have low thermal diffusivity. [30] **Figure 2.4a-d**

show the microstructure of inkjet printed silver features that are either thermally sintered at 130°C for 6 minutes or photonically annealed for 5 seconds. Only the photonic annealed film exhibits particle sintering, with traces exhibiting a conductivity of 40% of bulk silver. A representative example of a flexible inkjet printed and photonically annealed circuit is shown in **Figure 2.4e**. The flexible circuit board was created using roll-to-roll processes.[28]

2.3.3 Low-Temperature Sintering Enhanced via Substrate Reactivity

High conductivity silver films have recently been created by self-sintering of silver nanoparticles at room temperature. [34, 35] It is well known that self-sintering is hindered by the presence of polymer capping agents and viscosity modifiers present within the ink, since these additives must be thermally decomposed (typically above 200°C) to induce good contacts between adjacent particles.[36–38] To facilitate room temperature sintering, the polymer capping agents must be removed from the particles after printing. Kawahara, et al. recently reported a technique called "Instant Inkjet Circuits" in which a commercial ink composed of silver nanoparticles suspended in a polymer latex/halide emulsion, deposited on glossy photo paper, and then dried at room temperature.[3] **Figure 2.5a** shows a printed device in which z-axis conductive tape is used to adhere a chip to the printed electrodes. Instant particle sintering ensues upon drying the ink, resulting in printed traces with an electrical conductivity that is approximately 25% of bulk silver. However, their approach requires the use of a special polymer-coated paper, which acts to desorb the particle capping agent and promote inter-particle contacts. Printed traces produced from this ink are not conductive, when patterned on regular photocopy paper or plastic substrates.[3]

Another approach for creating conductive silver features at room temperature, involves inkjet printing an ink composed of silver nanoparticles with a polyanion capping agent (PAA) onto a flexible substrate. Subsequent printing of polycation (PDAC) solution onto the printed film promotes the desorption of the polyanion capping agent from the particle surfaces, thereby allowing the particles to spontaneously coalesce. A schematic of this process is shown in **Figure 2.5b**. Using this approach, a maximum conductivity of 20% of bulk silver can be obtained. Printed devices were produced on both paper and polymer substrates.

While this process yields high conductivity printed traces, it requires a second printing step to deliver the polycation stripping agent.[39]

2.4 Resistive Carbon Inks

Resistive inks are typically composed of carbon particles in the form of carbon black suspended in a solvent with a binder. There are many applications in which resistive inks are preferred to highly conductive inks. For example, carbon inks are less costly, and hence preferred for applications where high conductivity traces are not necessary. Carbon traces are also suitable for mechanical sensing applications in which a change in resistance is detected based on deformation. A broader range of electrical resistance can be achieved by blending carbon particle inks with conductive silver inks.[40]

Carbon black is elemental carbon in the form of spherical primary nanoparticles that are weakly aggregated. While it is primary used as a dark pigment, its conductivity makes it a good choice as a filler in conductive inks and pastes. The performance of a carbon black ink depends on the primary structure of the nanoparticles and the secondary structure of the branching aggregates.[41] Generally, particles with small primary particle size and high structure (open) aggregates result in more highly conductive inks than carbon black with large particle size and low structure (dense) aggregates.[42, 43] On the other hand, lower structure aggregates are easier to disperse at high concentration, which is another factor that affects ink conductivity. A summary of carbon black properties is shown in **Figure 2.6**.[41]

Beyond variations in primary particle and aggregate size, their surface chemistry can be tuned to enable dispersion in aqueous or non-aqueous solvents. In one embodiment, carbon black screen-printing paste contains a fast-drying solvent and a UV curable component. An active matrix sensor network is screen-printed using five different electronic inks, including an array of carbon electrodes. The ink used is Dupont C7102.[44] In another embodiment, paper soaked with India ink, a water-based writing ink composed of dark carbon and ceramic pigments, was used in vacuum tube radios as a grid leak resistor.[45] Finally, carbon inks can be used simply for printing resistor components along side highly conductive circuit traces.

2.5 Patterning Methods for Printed Electronics

The prominent techniques for depositing conductive and resistive inks onto plastic and paper substrates, include screen printing[2, 21], inkjet printing [3], airbrushing [46], and roll-to-roll printing [28]. As a benchmark, we begin with a brief introduction of metal evaporation and sputtering methods, which are commonly used in advanced electronic devices.

2.5.1 Metal Evaporation and Sputter Coating

Conductive metal traces are deposited conformally onto the substrate in a high-vacuum chamber via metal evaporation and sputter coating.[46–48] One notable example used this approach to deposit nickel traces on paper to create resistive heaters; which activate a thermochromic pattern on the opposite side of the paper.[46] An example of a foldable thermochromic display is shown in **Figure 2.7a**. Traces deposited by this technique have low resistance (1 Ω - 1 kΩ) without need for thermal annealing.

2.5.2 Screen Printing

Screen printing is a widely used technique in printed electronics. In this method, a highly viscous conductive ink is squeezed through a fine mesh screen that is patterned with a circuit design. For example, Hasan, *et al.*, used this approach to pattern a zinc oxide slurry over graphite electrodes to create a UV light sensor.[2] Images of the screen printed ink and the patterned device are shown in **Figure 2.7c**. Because this resistive sensor is meant to operate at high impedance (∼106 Ω), a large concentration of binder can remain in the ink, thus yielding functional features as-printed at room temperature. Moreover, the electrodes used in this system have 106 resistance, so a graphite pencil was used to create the interdigitated electrode array in this device.

2.5.3 Inkjet Printing

Inkjet printing is a drop-on-demand process in which a thermal or piezo driven pulses eject uniform ink droplets onto a surface.[33] Recently, inkjet printing has found use in paper-based

devices as a high-throughput method for creating disposable electronics and diagnostic tools. However, this method requires small particle size and dilute inks to ensure reliable printing through small orifices.[49] In one example, radio-frequency antennas are created by printing silver nanoparticle inks.[50] The target application is rapid construction of disposable RFID tags (**Figure 2.7b**). In this work, researchers use commercially available Cabot conductive silver ink with an average particle size of 12 nm. The as-printed inks are not conductive enough for RF applications, and must be annealed to at least 150 or 200°C in order to achieve even moderate resistivities of 3×10^{-2} to 5×10^{-3} Ω-cm.[51]

2.5.4 Roll-to-Roll Printing

In roll-to-roll printing, electronic materials are deposited on continuous films at a very high rate (>1 m/s).[28] Roll-to-roll techniques are used high throughput printing of low-cost electronics incorporating organic semiconductors as well as metallic inks. However, these methods generally suffer from poor resolution (50-100 μm) in addition to technique-specific disadvantages.[50] This class of printing techniques encompasses flexographic printing, offset lithography, and gravure printing of conductive inks, which are described below.

Offset printing employs a cylinder patterned with hydrophobic and hydrophilic regions.[52–54] First, water wets the hydrophilic regions of the roller, then the remaining hydrophobic areas are filled with conductive ink. Both materials are then transferred to an intermediate rubber roller, and finally to the substrate (**Figure 2.8a**). Typically, this method is used for porous substrates like paper: the water regions are absorbed by the substrate, providing a barrier to spreading of an oil-based ink. On non-porous plastic films, the water and oil combination actually leads to a loss of resolution because the liquid barrier distorts upon contact with a smooth surface.[53]

Flexographic printing uses a rubber relief plate, similar to a rubber stamp, to transfer ink to a substrate.[55, 56] An inking cylinder continuously replenishes the surface of the stamp during printing (**Figure 2.8b**). The rubber stamp form is relatively easy to produce, making this an attractive printing method. However, the types of ink that can be used are limited because organic solvents could deform the rubber surface. In addition, the width

and thickness of printed features is heavily dependent on the printing pressure, which can be difficult to control.

In gravure printing, an embossed metal cylinder is loaded with ink that is then transferred directly to the substrate stock (**Figure 2.8c**). A line pattern is broken into discrete pits or wells and the deposited dots merge on the substrate. Because this technique uses a rigid rather than flexible printing form, it offers the highest resolution of the three common roll-to-roll printing techniques.[57–59] In addition, there is no loss of fidelity associated with transferring the ink to an intermediate roller. Many ink types can be used with gravure printing, including water-based inks. The main disadvantage of gravure printing is the relatively higher cost of embossing a metal printing roller. **Figure 2.8d** shows an example of a silver oxide ink pattern formed by gravure printing.[50]

2.5.5 Airbrushing

Airbrush spraying of inks through a shadow mask is another way to create conformal features on paper. In one example, nickel or silver flakes suspended in an acrylic base were loaded into an aerosol deposition wand.[1] The ink was sprayed through a shadow mask in order to create a foldable circuit board. Electronic paper origami structures created using this method are shown in **Figure 2.7d**. Other low-viscosity ink formulas, such as particle free inks described in **Section 2.3.3**, are also suitable for airbrushing application.[24]

2.6 Figures

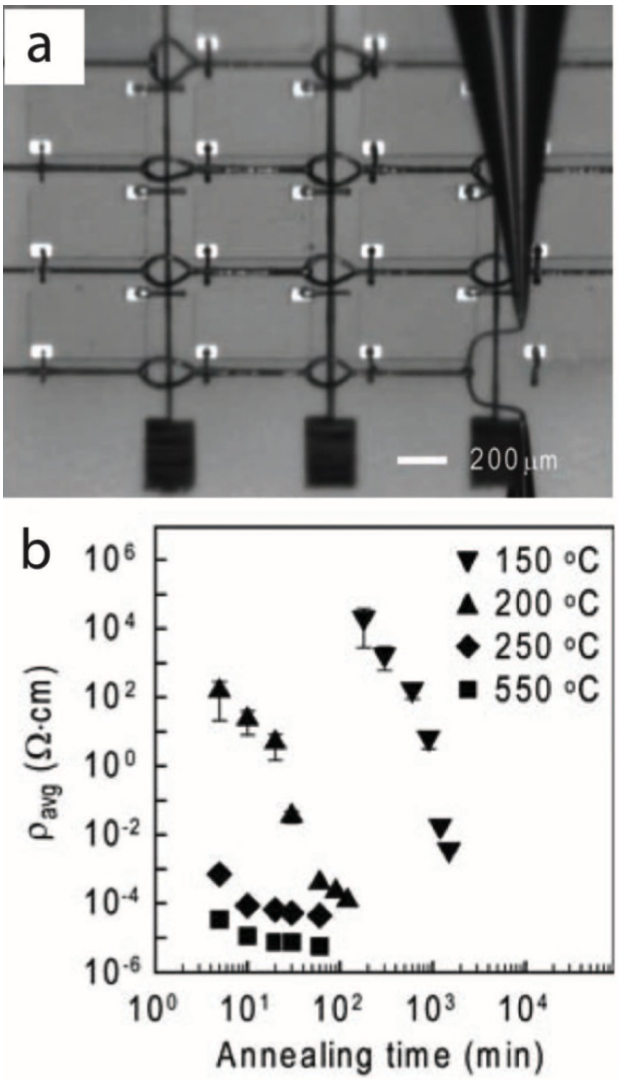

Figure 2.1: Omnidirectional printing of silver ink. (a) Spanning electrodes printed by a silver nanoparticle ink. (b) Average electrical resistivity of printed microelectrodes as a function of annealing temperature and time. [9]

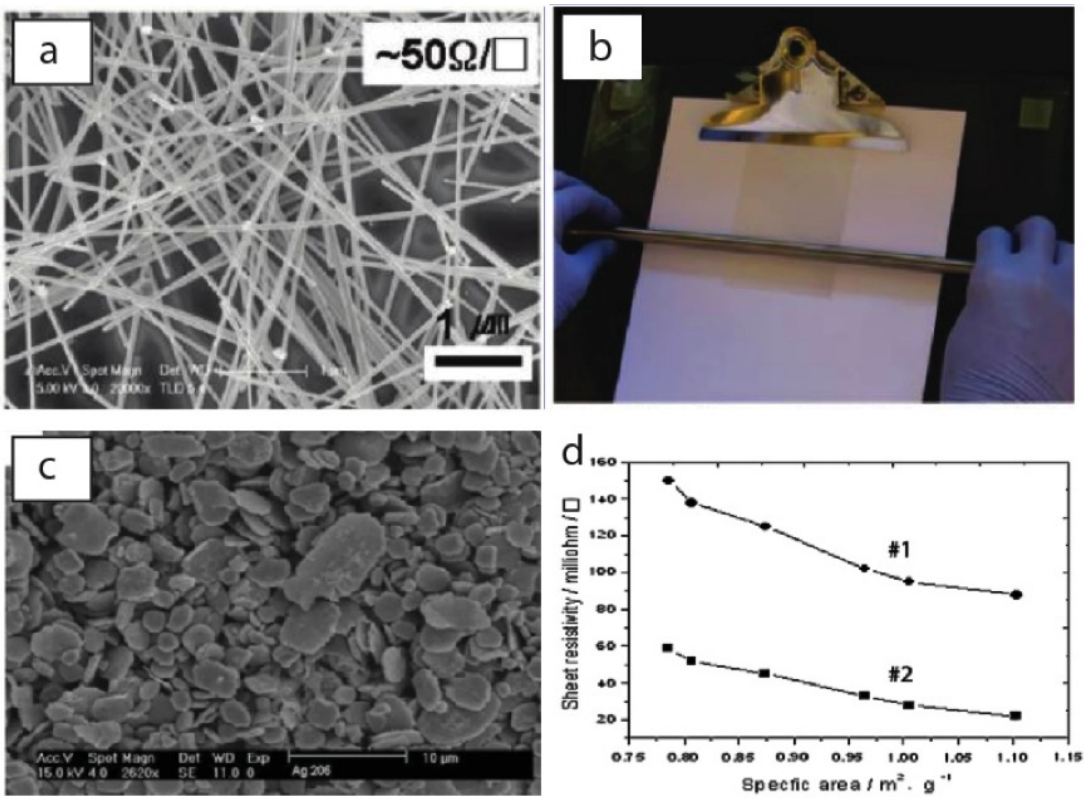

Figure 2.2: High-aspect ratio silver particles. (a) Silver microwires grown using the polyol process. (b) Silver microwire film formed by a Meyer rod. Silver microwires are used to create transparent conductors. [16] (c) A silver flake-based screen printing ink; flakes are produced by ball milling.[11] (d) Sheet resistance of two inks as a function of flake diameter.[11]

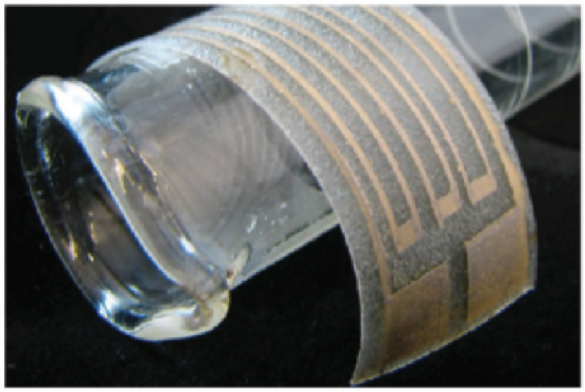

Figure 2.3: Spray coated reactive silver ink on an ethyl vinyl acetate (EVA) substrate. Silver particle formation occurs upon drying the ink in air.[24]

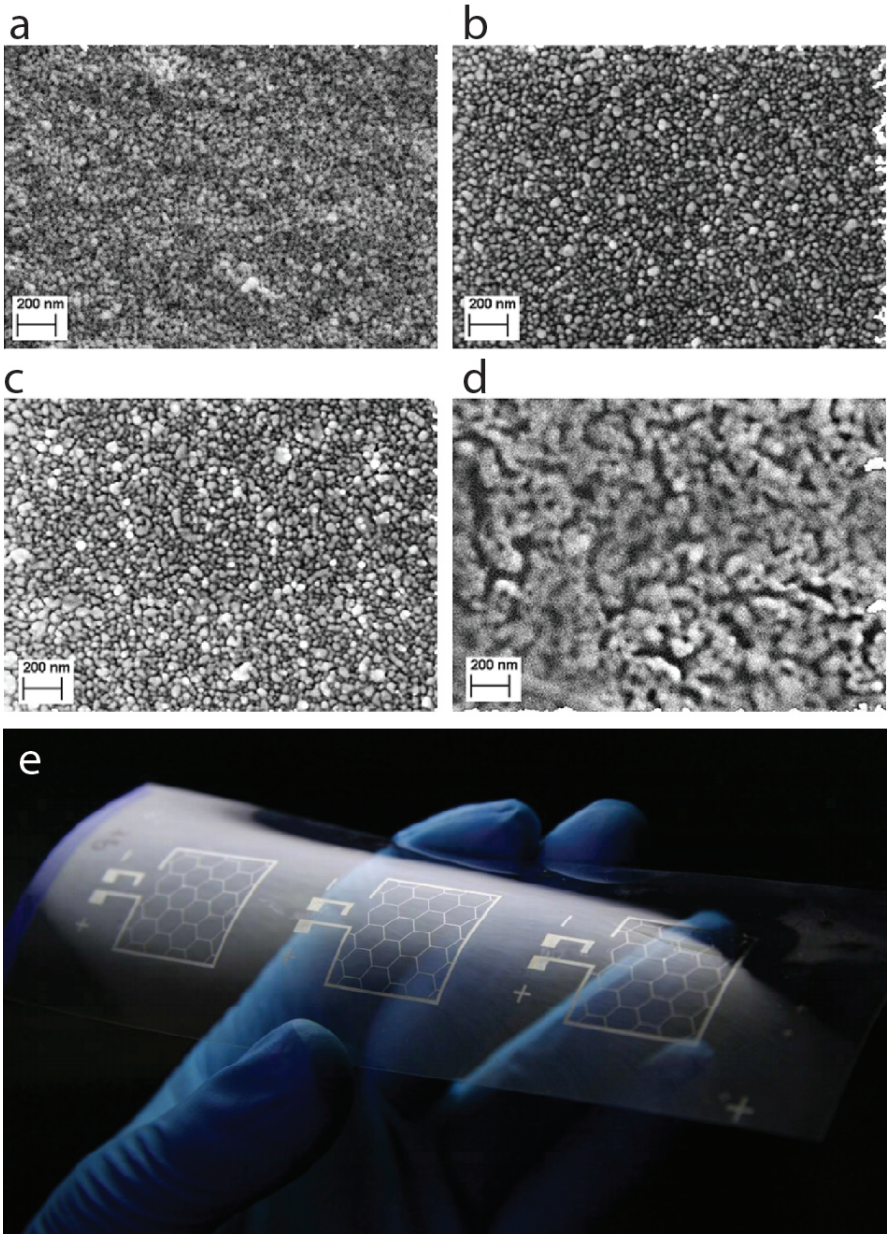

Figure 2.4: Photonic annealing. (a) SEM images of an inkjet printed silver track after 10 min thermal annealing at 130°C, (b) 30 min thermal annealing, (c) 360 min thermal annealing, and (d) 5 seconds of flash sintering. [29] (e) Inkjet printed circuit pattern after 15 seconds of sequential microwave and photonic sintering.[28]

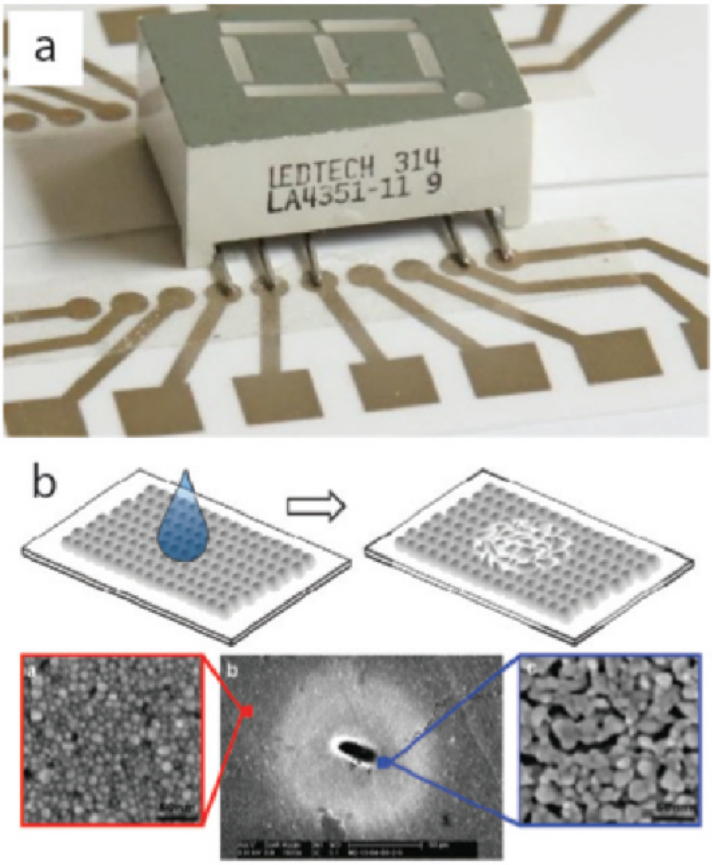

Figure 2.5: Representative examples of silver nanoparticle inks designed to sinter at room temperature. (a) Instant inkjet circuits printed by a commercial inkjet print head. Seven-segment display component is attached using z-axis tape. [3] (b) Chemical sintering of an inkjet printed silver nanoparticle ink using oppositely charged polyelectrolyte solution.[39]

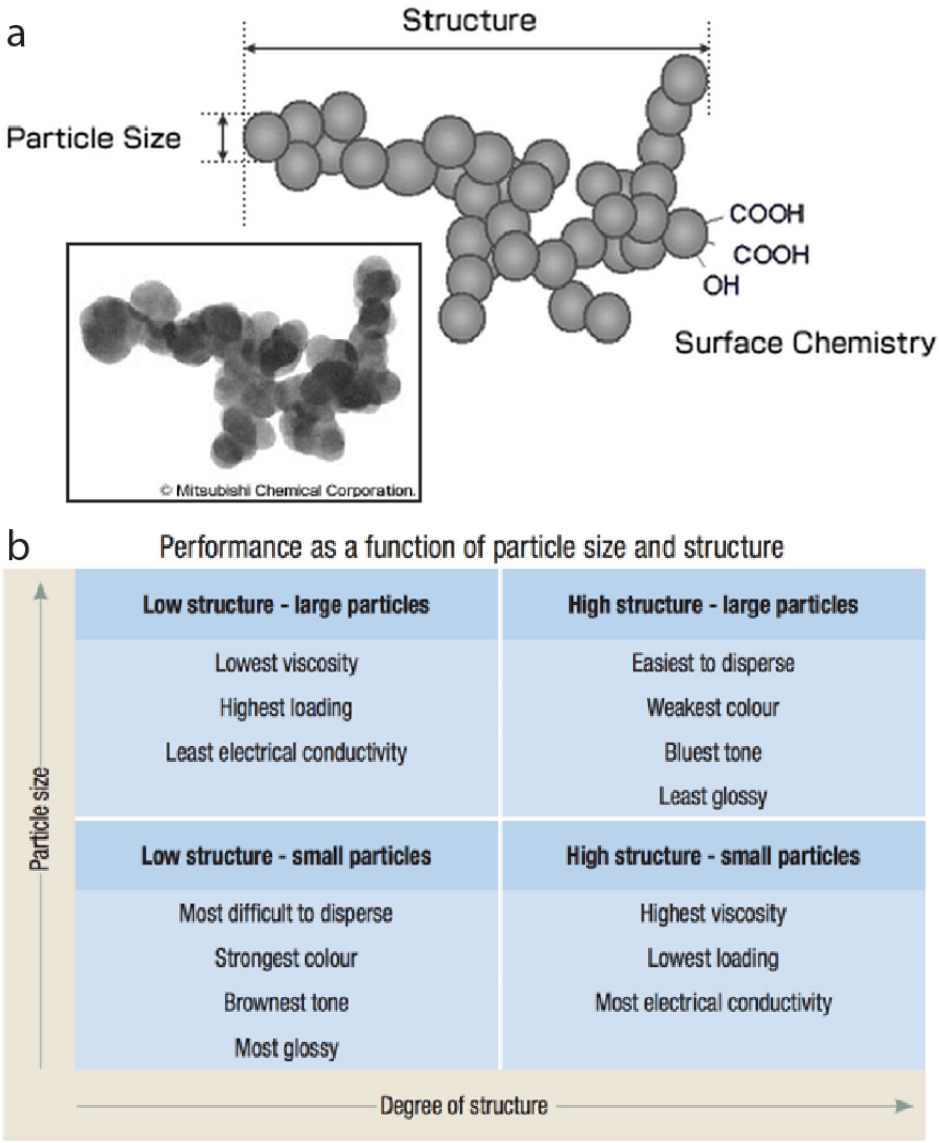

Figure 2.6: The properties of carbon black particles and aggregates with high structure (branched) and low structure (dense) morphologies. (a) A diagram of the primary and secondary structure of carbon black. inset: TEM micrograph of carbon black aggregate.[42] (b) The effect of particle size and aggregate structure on the dispersibility, viscosity, and conductivity of carbon black inks.[41]

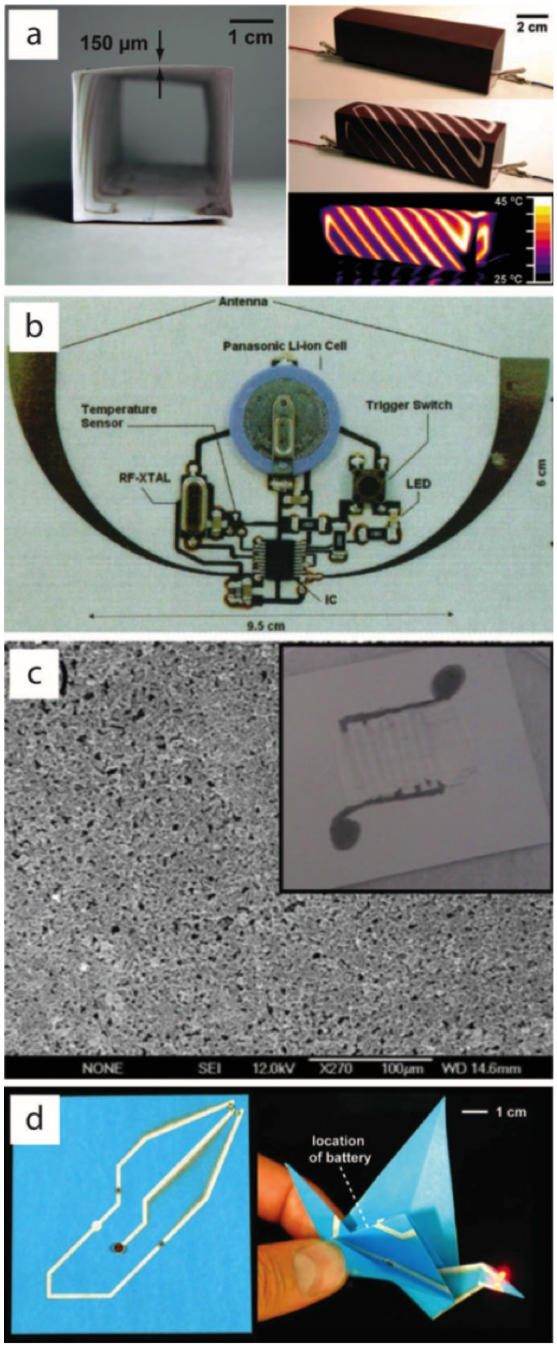

Figure 2.7: Examples of paper electronic devices. (a) A thermochromic display operated via restive heating of nickel traces,[46] (b) inkjet-printed RFID tag on paper,[60] (c) screen printed zinc oxide UV sensor with graphite electrodes,[2] and (d) electronic origami.[1]

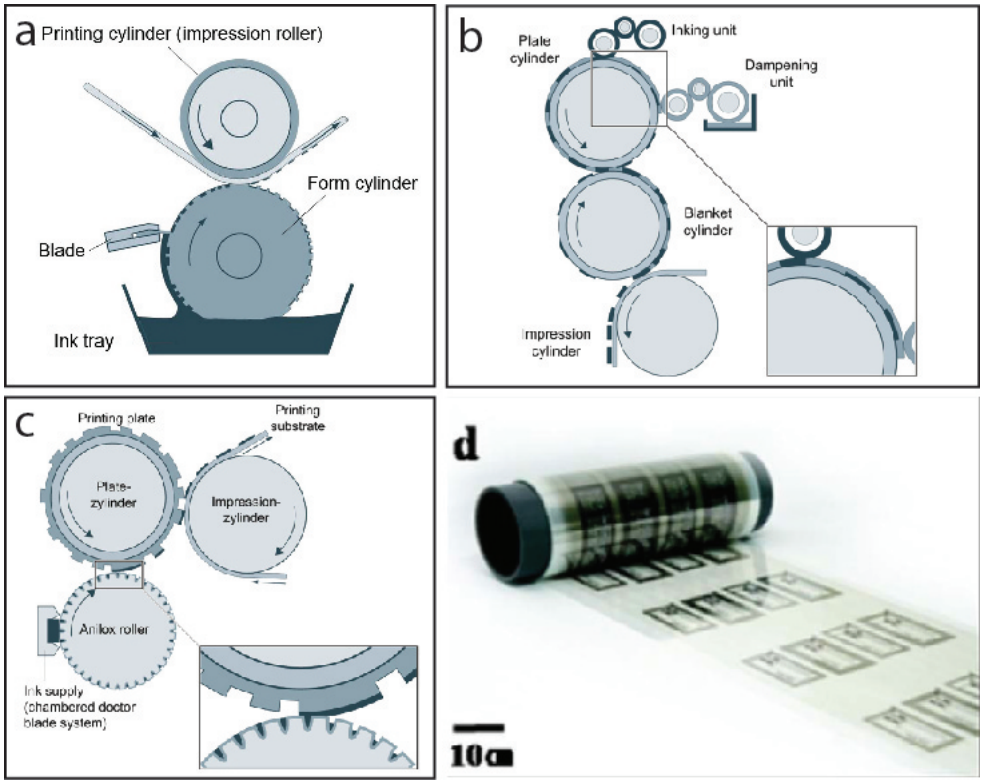

Figure 2.8: Roll-to-roll printing methods. (a) Flexographic lithography, (b) offset printing, and (c) gravure printing.[52] (d) Example of a silver oxide particle ink patterned using a gravure printing plate.[50]

2.7 References

[1] Adam C. Siegel, Scott T. Phillips, Michael D. Dickey, Nanshu Lu, Zhigang Suo, and George M. Whitesides. Printable electronics: Foldable printed circuit boards on paper substrates (adv. funct. mater. 1/2010). *Advanced Functional Materials*, 20(1):n/a–n/a, January 2010.

[2] Kamran ul Hasan, Omer Nur, and Magnus Willander. Screen printed ZnO ultraviolet photoconductive sensor on pencil drawn circuitry over paper. *Applied Physics Letters*, 100(21):211104, 2012.

[3] Yoshihiro Kawahara, Steve Hodges, Benjamin S. Cook, Cheng Zhang, and Gregory D. Abowd. Instant inkjet circuits: Lab-based inkjet printing to support rapid prototyping of UbiComp devices. In *Proceedings of the 2013 ACM International Joint Conference on Pervasive and Ubiquitous Computing*, UbiComp '13, pages 363–372, New York, NY, USA, 2013. ACM.

[4] F. Fievet, J.p. Lagier, and M. Figlarz. Preparing monodisperse metal powders in micrometer and submicrometer sizes by the polyol process. *MRS Bulletin*, 14(12):29–34, 1989.

[5] Tao Zhao, Rong Sun, Shuhui Yu, Zhijun Zhang, Limin Zhou, Haitao Huang, and Ruxu Du. Size-controlled preparation of silver nanoparticles by a modified polyol method. *Colloids and Surfaces A: Physicochemical and Engineering Aspects*, 366(13):197–202, August 2010.

[6] Dongjo Kim, Sunho Jeong, and Jooho Moon. Synthesis of silver nanoparticles using the polyol process and the influence of precursor injection. *Nanotechnology*, 17(16):4019, August 2006.

[7] Pierre-Yves Silvert, Ronaldo Herrera-Urbina, Nicolas Duvauchelle, Venugopal Vijayakrishnan, and Kamar Tekaia Elhsissen. Preparation of colloidal silver dispersions by the polyol process. part 1synthesis and characterization. *Journal of Materials Chemistry*, 6(4):573–577, January 1996.

[8] Alexander Pyatenko, Munehiro Yamaguchi, and Masaaki Suzuki. Laser photolysis of silver colloid prepared by citric acid reduction method. *The Journal of Physical Chemistry B*, 109(46):21608–21611, November 2005.

[9] Bok Y. Ahn, Eric B. Duoss, Michael J. Motala, Xiaoying Guo, Sang-Il Park, Yujie Xiong, Jongseung Yoon, Ralph G. Nuzzo, John A. Rogers, and Jennifer A. Lewis. Omnidirectional printing of flexible, stretchable, and spanning silver microelectrodes. *Science*, 323(5921):1590–1593, March 2009.

[10] Chang Chen, Li Wang, Ruilin Li, Guohua Jiang, Haojie Yu, and Tao Chen. Effect of silver nanowires on electrical conductance of system composed of silver particles. *Journal of Materials Science*, 42(9):3172–3176, May 2007.

[11] Wu Songping. Preparation of micron size flake silver powders for conductive thick films. *Journal of Materials Science: Materials in Electronics*, 18(4):447–452, April 2007.

[12] Sukanta De, Thomas M. Higgins, Philip E. Lyons, Evelyn M. Doherty, Peter N. Nirmalraj, Werner J. Blau, John J. Boland, and Jonathan N. Coleman. Silver nanowire networks as flexible, transparent, conducting films: Extremely high DC to optical conductivity ratios. *ACS Nano*, 3(7):1767–1774, July 2009.

[13] Yugang Sun and Younan Xia. Shape-controlled synthesis of gold and silver nanoparticles. *Science*, 298(5601):2176–2179, December 2002.

[14] Benjamin Wiley, Yugang Sun, and Younan Xia. Synthesis of silver nanostructures with controlled shapes and properties. *Accounts of Chemical Research*, 40(10):1067–1076, October 2007.

[15] Stephen M. Bergin, Yu-Hui Chen, Aaron R. Rathmell, Patrick Charbonneau, Zhi-Yuan Li, and Benjamin J. Wiley. The effect of nanowire length and diameter on the properties of transparent, conducting nanowire films. *Nanoscale*, 4(6):1996–2004, March 2012.

[16] Yuan-Jun Song, Jing Chen, Jing-Yuan Wu, and Tong Zhang. Applications of silver nanowires on transparent conducting film and electrode of electrochemical capacitor. *Journal of Nanomaterials*, 2014:e193201, June 2014.

[17] David S. Hecht, David Thomas, Liangbing Hu, Corinne Ladous, Tom Lam, Youngbae Park, Glen Irvin, and Paul Drzaic. Carbon-nanotube film on plastic as transparent electrode for resistive touch screens. *Journal of the Society for Information Display*, 17(11):941–946, November 2009.

[18] Liangbing Hu, Han Sun Kim, Jung-Yong Lee, Peter Peumans, and Yi Cui. Scalable coating and properties of transparent, flexible, silver nanowire electrodes. *ACS Nano*, 4(5):2955–2963, May 2010.

[19] Cai-Hong Liu and Xun Yu. Silver nanowire-based transparent, flexible, and conductive thin film. *Nanoscale Research Letters*, 6(1):75, January 2011.

[20] Behnam Meschi Amoli, Ehsan Marzbanrad, Anming Hu, Y. Norman Zhou, and Boxin Zhao. Electrical conductive adhesives enhanced with high-aspect-ratio silver nanobelts. *Macromolecular Materials and Engineering*, 299(6):739–747, June 2014.

[21] Rita Faddoul, Nadege Reverdy-Bruas, and Anne Blayo. Formulation and screen printing of water based conductive flake silver pastes onto green ceramic tapes for electronic applications. *Materials Science and Engineering B-Advanced Functional Solid-State Materials*, 177(13):1053–1066, August 2012.

[22] Hui-wang Cui, Qiong Fan, and Dong-sheng Li. Novel flexible electrically conductive adhesives from functional epoxy, flexibilizers, micro-silver flakes and nano-silver spheres for electronic packaging. *Polymer International*, 62(11):1644–1651, November 2013.

[23] Yiliang Wu, Yuning Li, and Beng S. Ong. A simple and efficient approach to a printable silver conductor for printed electronics. *Journal of the American Chemical Society*, 129(7):1862–1863, February 2007.

[24] S. Brett Walker and Jennifer A. Lewis. Reactive silver inks for patterning high-conductivity features at mild temperatures. *Journal of the American Chemical Society*, 134(3):1419–1421, January 2012.

[25] Sebastian Wnscher, Tobias Rasp, Michael Grouchko, Alexander Kamyshny, Renzo M. Paulus, Jolke Perelaer, Torsten Kraft, Shlomo Magdassi, and Ulrich S. Schubert. Simulation and prediction of the thermal sintering behavior for a silver nanoparticle ink based on experimental input. *Journal of Materials Chemistry C*, 2(31):6342–6352, July 2014.

[26] Julia R. Greer and Robert A. Street. Thermal cure effects on electrical performance of nanoparticle silver inks. *Acta Materialia*, 55(18):6345–6349, October 2007.

[27] Thomas hlund, Jonas rtegren, Henrik Andersson, and Hans-Erik Nilsson. Sintering methods for metal nanoparticle inks on flexible substrates. *NIP & Digital Fabrication Conference*, 2009(2):614–617, January 2009.

[28] Jolke Perelaer, Robert Abbel, Sebastian Wnscher, Robin Jani, Tim van Lammeren, and Ulrich S. Schubert. Roll-to-roll compatible sintering of inkjet printed features by photonic and microwave exposure: From non-conductive ink to 40% bulk silver conductivity in less than 15 seconds. *Advanced Materials*, 24(19):2620–2625, May 2012.

[29] Yulia Galagan, Erica W. C. Coenen, Robert Abbel, Tim J. van Lammeren, Sami Sabik, Marco Barink, Erwin R. Meinders, Ronn Andriessen, and Paul W. M. Blom. Photonic sintering of inkjet printed current collecting grids for organic solar cell applications. *Organic Electronics*, 14(1):38–46, January 2013.

[30] Robert Abbel, Tim van Lammeren, Rob Hendriks, Jeroen Ploegmakers, Eric J. Rubingh, Erwin R. Meinders, and Wilhelm A. Groen. Photonic flash sintering of silver

nanoparticle inks: a fast and convenient method for the preparation of highly conductive structures on foil. *MRS Communications*, 2(04):145–150, December 2012.

[31] J West, M Carter, S Smith, and J Sears. Photonic curing of silver nanoparticle based inks deposited by m3d. *Nanotech*, 2, 2010.

[32] K.A. Schroder, S.C. McCool, and W.R. Furlan. Broadcast photonic curing of metallic nanoparticle films. *Proceedings of the 2006 NSTI Nanotechnology Conference*, 3, 2006.

[33] Juha Niittynen, Robert Abbel, Matti Mntysalo, Jolke Perelaer, Ulrich S. Schubert, and Donald Lupo. Alternative sintering methods compared to conventional thermal sintering for inkjet printed silver nanoparticle ink. *Thin Solid Films*, 556:452–459, April 2014.

[34] X Zhao and S Wang. *Journal of the Physical Society of Japan*, 70, 2001.

[35] K. S. Moon, H. Dong, R. Maric, S. Pothukuchi, A. Hunt, Y. Li, and C. P. Wong. Thermal behavior of silver nanoparticles for low-temperature interconnect applications. *Journal of Electronic Materials*, 34(2):168–175, February 2005. WOS:000227103700008.

[36] Sankaran Sivaramakrishnan, Perq-Jon Chia, Yee-Chia Yeo, Lay-Lay Chua, and Peter K.-H. Ho. Controlled insulator-to-metal transformation in printable polymer composites with nanometal clusters. *Nature Materials*, 6(2):149–155, February 2007.

[37] Dongjo Kim, Sunho Jeong, Bong Kyun Park, and Jooho Moon. Direct writing of silver conductive patterns: Improvement of film morphology and conductance by controlling solvent compositions. *Applied Physics Letters*, 89(26):264101, December 2006.

[38] Thijs H. J. van Osch, Jolke Perelaer, Antonius W. M. de Laat, and Ulrich S. Schubert. Inkjet printing of narrow conductive tracks on untreated polymeric substrates. *Advanced Materials*, 20(2):343–+, January 2008.

[39] Shlomo Magdassi, Michael Grouchko, Oleg Berezin, and Alexander Kamyshny. Triggering the sintering of silver nanoparticles at room temperature. *ACS Nano*, 4(4):1943–1948, April 2010.

[40] Alexander Bessonov, Marina Kirikova, Samiul Haque, Ilya Gartseev, and Marc J. A. Bailey. Highly reproducible printable graphite strain gauges for flexible devices. *Sensors and Actuators a-Physical*, 206:75–80, February 2014.

[41] Pigment blacks selection guide for printing ink applications. *Cabot Corp.*

[42] Three main properties of carbon black. *Mitsubishi Chemical*.

[43] D Weingarth, D Cericola, F.C.F. Mornaghini, T Hucke, and R Kotz. Carbon additives for electrical double layer capacitor electrodes. *Journal of Power Sources*, 266, 2014.

[44] Martin Zirkl, Anurak Sawatdee, Uta Helbig, Markus Krause, Gregor Scheipl, Elke Kraker, Peter Andersson Ersman, David Nilsson, Duncan Platt, Peter Bod, Siegfried Bauer, Gerhard Domann, and Barbara Stadlober. Touchless interfaces: An all-printed ferroelectric active matrix sensor network based on only five functional materials forming a touchless control interface (adv. mater. 18/2011). *Advanced Materials*, 23(18):2023–2023, May 2011.

[45] Henry Smith Williams. *Practical Radio*. Funk and Wagnalls, 1925.

[46] Adam C. Siegel, Scott T. Phillips, Benjamin J. Wiley, and George M. Whitesides. Thin, lightweight, foldable thermochromic displays on paper. *Lab on a Chip*, 9(19):2775–2781, October 2009.

[47] S. Shahidi, M. Ghoranneviss, B. Moazzenchi, A. Anvari, and A. Rashidi. Aluminum coatings on cotton fabrics with low temperature plasma of argon and oxygen. *Surface and Coatings Technology*, 201(911):5646–5650, February 2007.

[48] J. Scholz, G. Nocke, F. Hollstein, and A. Weissbach. Investigations on fabrics coated with precious metals using the magnetron sputter technique with regard to their antimicrobial properties. *Surface and Coatings Technology*, 192(23):252–256, March 2005.

[49] Hsien-Hsueh Lee, Kan-Sen Chou, and Kuo-Cheng Huang. Inkjet printing of nanosized silver colloids. *Nanotechnology*, 16(10):2436–2441, October 2005.

[50] F.C. Krebs. *Journal of Materials Chemistry*, 19, 2009.

[51] Li Yang, Amin Rida, and Manos M. Tentzeris. Design and development of radio frequency identification (RFID) and RFID-enabled sensors on flexible low cost substrates. *Synthesis Lectures on RF/Microwaves*, 1(1):1–89, January 2009.

[52] Products and solutions for printing press - machine building - siemens.

[53] Juraj Gigac, Miroslava Kasajova, and Monika Stankovska. The influence of paper surface energy on multicolor offset print mottling. *Tappi Journal*, 13(2):55–64, February 2014.

[54] B. J. Ramsey P. M. Harrey. Capacitive-type humidity sensors fabricated using the offset lithographic printing process. *Sensors and Actuators B-chemical - SENSOR ACTUATOR B-CHEM*, 87(2):226–232, 2002.

[55] M. N. Nodin and M. S. Yusof. A preliminary study of PDMS stamp towards flexography printing technique: An overview. In C. Nakason, A. Thitithammawong, and S. Wisunthorn, editors, *Advances in Rubber*, volume 844, pages 201–204. Trans Tech Publications Ltd, Stafa-Zurich, 2014.

[56] Arved C. Huebler, Maxi Bellmann, Georg C. Schmidt, Stefan Zimmermann, Andre Gerlach, and Christian Haentjes. Fully mass printed loudspeakers on paper. *Organic Electronics*, 13(11):2290–2295, November 2012.

[57] Donna Clark. Major trends in gravure printed electronics. *Graphic Communication*, June 2010.

[58] M. Hambsch, K. Reuter, M. Stanel, G. Schmidt, H. Kempa, U. Fgmann, U. Hahn, and A. C. Hbler. Uniformity of fully gravure printed organic field-effect transistors. *Materials Science and Engineering: B*, 170(13):93–98, June 2010.

[59] Ethan B. Secor, Sooman Lim, Heng Zhang, C. Daniel Frisbie, Lorraine F. Francis, and Mark C. Hersam. Gravure printing of graphene for large-area flexible electronics. *Advanced Materials*, 26(26):4533–4538, July 2014.

[60] A Rida, Li Yang, R. Vyas, and M.M. Tentzeris. Conductive inkjet-printed antennas on flexible low-cost paper-based substrates for RFID and WSN applications. *IEEE Antennas and Propagation Magazine*, 51(3):13–23, June 2009.

CHAPTER 3

DESIGN AND CHARACTERIZATION OF CONDUCTIVE SILVER AND RESISTIVE CARBON INKS

3.1 Introduction

Particle-based metallic and carbon inks are widely used in airbrush spraying[1], inkjet printing[2–4], screen printing[5, 6], and most recently rollerball pens[7] for the creation of paper-based electronics. To date, most conductive inks developed for printed electronics exhibit high resistivity and hence require post-processing steps such as thermal or photonic annealing.[8, 9] This limiting behavior arises from the use of polymer capping or viscosifying agents that disrupt the percolating network of metallic particles.

Here we design and characterize silver particle inks that enable direct patterning of highly conductive features. The ink viscosity is specifically tuned for use in multiple printing techniques including (1) rollerball pen writing[7] and (2) direct ink writing (DIW)[8, 10]. To complement this conductive ink, we also design and characterize a carbon nanoparticle resistive ink that exhibits an electrical resistivity that is six orders of magnitude higher than the conductive silver ink. Our resistive carbon ink enables direct writing of resistive traces on paper and plastic substrates. Furthermore, by combining these two inks, we can achieve specifically targeted conductivities by varying the volume ratio of silver to carbon particles.

3.2 Experimental Methods

3.2.1 Silver Inks

Silver inks are synthesized by mixing 1.915 g of polyacrylic acid (PAA, MW = 1,800 g/mol, 65 wt% aqueous solution) with 50 g water and 40 g diethanolamine (DEA) and stirring for 2 h in a water bath at room temperature. In this formulation, PAA serves as a capping

agent for the silver particles and DEA serves as a reducing agent for the silver salt. A silver nitrate solution (20 g $AgNO_3$ in 15 ml H_2O) is then injected into this solution, while stirring vigorously. The initially clear solution is gently stirred for 22 h at room temperature. The solution gradually becomes dark black, coinciding with the formation of silver nanoparticles ($\sim$5 nm in diameter). These silver nanoparticles are then ripened by sonicating the solution in a water bath heated to 65°C for 1.5 h. This step results in a mean particle size of 400 ± 124 nm, as determined using transmission electron microscopy (JEOL 2100 Cryo TEM, JEOL Ltd) combined with image analysis (Adobe Photoshop).[7]

After cooling, 300 ml of ethanol, a poor solvent for the PAA-capped particles, is titrated at 10 ml/min to induce particle coagulation. After decanting the supernatant, the precipitate is centrifuged at 9,000 rpm for 20 minutes to concentrate the ink. The ink is then re-dispersed in 25 ml of water by vortexing and sonication at room temperature. The resulting solution is centrifuged again at 9,000 rpm for 20 minutes to remove excess capping agent, PAA. This washing step is performed a total of three times and the polymer content is assessed using thermogravimetric analysis (TGA) of dried and powdered samples heated in air to 600C at a rate of 10°C per minute (TA Instruments). The final washed product is dispersed in 15 ml of water and filtered through a 10 m polycarbonate filter. A separate viscosifying solution is prepared by dissolving 2 wt% hydroxyethyl cellulose (HEC) in a 1:1 mixture of water and methanol and stirring at 70°C until a transparent liquid forms. The solution is cooled to room temperature and filtered through a 5 μm pore teflon filter. The HEC solution is added to the silver ink to achieve the desired ratio of HEC to silver of 3:100 by weight. The influence of HEC:Ag ratio on ink resistivity is characterized by creating inks with a broader range of HEC content. The mixture is homogenized (Thinky ARE-250 Conditioning Planetary Mixer) at 2000 rpm for 3 min and allowed to dry under vacuum until a solids loading between 35-65 wt% silver is obtained.[7]

3.2.2 Carbon Inks

Carbon inks are prepared using conductive carbon black powder (Cabot Mogul-L). The powder is composed of high-structure carbon black particles specifically engineered for high

conductivity composites[11]. First, the carbon powder is dispersed in water (1 wt%) using a sonic dismembrator (Fisher) for 5 minutes with 1-second on/off pulses. Next, the solution pH is increased to pH = 9 using a dilute solution of sodium hydroxide. The solution is allowed to stir for 10 minutes and is sonicated again for 5 minutes. After dispersing the carbon black at high pH, no individual particle clusters are visible and the resulting fluid appears similar to a darkly pigmented India ink. Next, the dilute carbon dispersion is gradually added to a 3 wt% solution of hydroxyethyl cellulose (HEC) in water. The solution is homogenized by a planetary mixer (Thinky) and allowed to partially dry under vacuum. The process of adding carbon, homogenizing, and drying is sequentially performed until a HEC:carbon ratio of 2:1 by weight and a desired viscosity are reached.

3.2.3 Composite Inks With Tunable Resistivity

Separate batches of silver and carbon inks are formulated and their composition is determined by thermogravametric analysis (TGA, Mettler-Toledo). The two inks are then mixed together to produce composite inks with Ag:carbon volumetric ratios ranging from 1:0 to 0:1. Mixtures are formulated assuming a silver particle density of 10.49 g/ml and a carbon particle density of approximately 2 g/ml.

3.2.4 Rheological Properties of Conductive Silver Inks

The rheological properties of silver inks with solids loading ranging from 35-65 wt% silver and HEC:Ag ratio 3:100 by weight were measured using a controlled-stress rheometer (AR-EX 2000) fitted with a cone and plate geometry (60 mm diameter, 2° pitch). The temperature is set to 25°C and a solvent trap is used to minimize water evaporation. The rheological properties of HEC solutions with concentration ranging from 0.1 to 8.0 wt% in water are measured under the same conditions. Likewise, silver particle solutions with concentrations corresponding to the range of ink formulas (35, 45, 55, and 65wt% in water, without HEC) are also studied.

3.2.5 Thermal Annealing of Conductive Silver Inks

Silver films (1 cm × 1 cm wide, ∼12 μm in height) are produced by doctor blading the ink onto a glass slide, using Scotch tape to define the borders of the conductive patch. Films are allowed to dry in air at room temperature and then annealed on an aluminum-topped hotplate (Torrey Pines) to various temperatures ranging from 110° to 200°C.

3.2.6 Electrical Property Characterization

The sheet resistance of the annealed silver films and the carbon-silver blends are measured by a four-point-probe method (Multiheight Probe, Jandel Engineering Ltd.) and using a corresponding power supply (RM3-AR, Jandel Engineering Ltd.). The film thickness is measured either using a contact stylus profilometer (Dektak) or a laser profilometer (Keyence). The electrical resistivity of each sample is obtained by multiplying the sheet resistance (Ω/square) by the film thickness (cm).

3.3 Results and Discussion

3.3.1 Synthesis and Properties of Conductive Silver Inks

The solution-grown silver particles in the conductive silver ink are washed with water a total of three times in order to remove residual PAA capping agent. The PAA content in the ink after each washing step is determined by TGA and reported in **Figure 3.1a**. The as-synthesized silver particles, which have been concentrated by ethanol and centrifuged, contain 97% silver and 3% residual PAA capping agent. However, upon washing these particles, there is no measurable PAA content. The mean particle size after all washing steps are complete is 400 ± 200 nm. A representative TEM micrograph and histogram of particle sizes are shown in **Figure 3.1b-c**.

Hydroxyethyl cellulose (HEC) is added to the conductive silver inks to increase their solution or "carrier fluid" viscosity (relative to water) as well as enhance their adhesion to paper and polymer substrates. The viscosifier HEC is selected for its high viscosity index.[12]

An optimal HEC:Ag ratio of 3:100 is sufficient to produce homogenous inks that adhere well to paper and polyimide substrates.

To explore the effects of ink composition on viscosity, inks with a constant HEC:Ag ratio of 3:100 are produced. The ink composition is tuned by diluting dense inks with water so both the total silver concentration and the HEC concentration of the carrier fluid change simultaneously. The ink compositions ranging from 35-65 wt% silver are summarized in **Table 3.2**. Due to batch-to-batch variation in ink properties, this experiment is associated with *Batch A*. The apparent ink viscosity measured at a shear rate of 1 s^{-1} over a range of solids loading (35-65 wt% Ag) is shown in **Figure 3.2**. We observed that inks composed of 45-55 wt% silver are suitable of rollerball pen printing, while inks with higher silver concentration are used for direct ink writing (DIW) of conductive patterns. Both techniques wil be described in **Chapters 4-5**.

Figure 3.3 shows the apparent viscosity of silver inks composed of 40-55 wt% silver as a function of shear rate. Note that these inks are from a different production batch, *Batch B*. These inks, which are formulated for rollerball pen writing **(Ch. 4)** are shear thinning. The data corresponds well to a Carreau model for fluid viscosity.[13] The viscosity function for each ink reaches a unique zero-shear-rate plateau (η_o) that increases with increased silver solids loading. At intermediate shear rates, the ink is shear thinning and we assume that at extremely high shear rates the viscosity (η_∞) approaches that of the ink solvent (water, 8.89×10^{-4} Pa-s). In this model, expressed in **eq. 3.1**, λ is the relaxation time of the ink (i.e., it defines the length of the shear thinning regime) and n is a power index ($n < 1$ for shear thinning fluids). A fit to the measured data is represented in the plot in **Figure 3.3** and the plateau viscosities η_o and fitting parameters λ and n are reported in **Table 3.2**.

$$\eta(\dot{\gamma}) = \eta_\infty + (\eta_o - \eta_\infty)(1 + (\lambda\dot{\gamma})^2)^{\frac{n-1}{2}} \tag{3.1}$$

At intermediate shear rates, which are of interest to DIW and rollerball pen writing, the ink viscosity is well fitted by a power-law model for fluid viscosity. The Carreau model simplifies to **eq. 3.2** when the shear rate ($\dot{\gamma}$) is significantly larger than the inverse relaxation time, $1/\lambda$. The power-law model is applied to the ink viscosity data at shear rates between

33 and 3333 s^{-1} and the fitting parameter m is reported in **Table 3.2** for the four ink concentrations. Note that the power index n matches that of the Carreau model and the parameter m is nearly equal to $\eta_o \lambda^{n-1}$. The simplified power law model will be utilized in the analysis of rollerball pen printed inks in **Ch. 4**.

$$\eta(\dot{\gamma}) = m\dot{\gamma}^{(n-1)} \tag{3.2}$$

We find that there is an exponential increase in viscosity with increasing silver solids loading. This trend is evident in silver ink *Batch A* and illustrated in the plot of ink viscosity as a function of silver content at a single shear rate of 1 s^{-1} (**Figure 3.2**). The trend is again seen in a third ink batch, *Batch C* which is shown in (**Figure 3.5**). The viscosity at the shear rate plateau (sampled at ∼0.1 s^{-1}) varies from 0.1 to 311, or over three orders of magnitude, across the tunable concentration range.

As the ink composition is altered due to water evaporation, there are two contributing factors to an increase in viscosity; first, the particle concentration increases from 35–65 wt% silver (4.8–15 vol% silver) and second the HEC concentration in the carrier fluid increases from 1.6–5.5 wt%. The particle and polymer concentrations are summarized in **Table 3.1**. Henceforth, the weight% solids loading of silver is used as an index number to identify the particular ink formula, whereas the volume loading of silver is more relevant to the analysis of rheological properties of the inks. In the analysis of our inks, η is the apparent viscosity of the ink, ϕ is the volume fraction of silver particles, ϕ_{HEC} is the HEC concentration in the carrier fluid, and η_s is the solution viscosity (water+HEC).

First we consider the contribution of the carrier fluid viscosity (η_s) on the ink viscosity. The structure of the HEC molecule is shown in **Figure 3.4a**. It is composed of a stiff cellulose backbone decorated with hydroxyethyl groups of various length. The polymer is uncharged, and we expect that it does not adsorb to or interact with the silver particles in the ink. **Figure 3.4b** shows the apparent viscosity of HEC polymer solutions (1.6–5.5 wt%) as a function of shear rate. HEC solutions in this concentration range are shear thinning at intermediate shear rates, much like the corresponding silver inks studied for rollerball pen writing (**Figure 3.3**).

The apparent viscosity of HEC solutions at the zero shear plateau, as a function of HEC concentration, is shown in **Figure 3.4c**. The range of HEC concentrations measured is 0.5–8.0 wt% in water. Notably, the viscosity of these solutions increases exponentially between 1.0-8.0 vol% HEC, scaling with concentration to the power of 4.06. This exponent is indicated as a slope on the log-log plot in **Figure 3.4c**. There is a shoulder in the data at 1.0 vol% where a slow increase in viscosity becomes very rapid. At concentrations below 1.0 wt%, viscosity increases approximately linearly with concentration (a slope of 0.95 is shown on the plot). Above this concentration, the HEC solution undergoes a transition between a dilute state in which the polymer chains are non-interacting to a state in which strong interactions or entanglements exist. Across the composition range relevant to silver inks (1.6–5.6 vol%) the polymer chains are interacting and viscosity increases markedly from 0.12 to 21.9 Pa-s, or by a factor of 182. The data corresponding to silver ink compositions is duplicated in **Figure 3.5** to compare to the silver ink viscosity. The power law model is reported in **Eq. 3.3** below.

$$\eta_s = 3\times10^6(\phi_{HEC})^{4.06} \tag{3.3}$$

Next we consider the contribution of the silver particles on the viscosity of the inks. The apparent viscosity of silver particle solutions of varied concentration (4.8-15 vol%) is measured at the zero shear plateau (**Figure 3.5**). The viscosity increases from 0.0018 to 0.006 Pa-s over this range, or by a factor of 3.3.

Figure 3.5 compares the viscosities of the HEC and silver particle solutions to the ink viscosity *(Batch C)*. Note that the alternate axis on the top the plot indicates the composition of the HEC carrier fluids that are associated with each ink composition. Our data indicates that the silver content has an amplified effect on the ink viscosity when it is mixed with the HEC carrier fluid, compared to water alone. Nevertheless, the HEC content has a stronger influence on the magnitude of the ink viscosity in the measured range and also contributes signficiantly to the shear thinning behavior of the silver ink.

3.3.2 Electrical Properties of Silver Inks

The electrical resistivity of silver films formed from the optimized silver ink (50 wt% solids loading and HEC:Ag ratio of 3:100) is measured as a function of annealing temperature and time, as shown in **Figure 3.6**. The ink films are conductive upon drying at room temperature for 30 min, exhibiting an electrical resistivity of 1.99×10^{-4} Ω-cm. Upon annealing at 110°C, a slight decrease in resistivity is observed, likely due to evaporation of residual solvent. Annealing at higher temperatures (170°C) resulted in a significant decrease in the electrical resistivity (4.34×10^{-5} Ω-cm) as the polymer binder degrades and particle sintering ensues. SEM micrographs in **Figure 3.7** show the microstructural evolution of cast films with increasing annealing temperature. Under ambient conditions, the silver particles form a conductive percolated network; solid necks between particles start to form at temperatures above 200°C.

Finally, the resistivity of silver inks is measured as a function of HEC:Ag ratio. The HEC:Ag weight ratios of the inks are varied between 3:100 (∼22:78 by volume) and 22:100 (∼64:36 by volume) and cast films were allowed to dry at room temperature. The resistivity of the ink films as a function of ink film composition is shown in **Figure 3.8a**. The resistivity of the ink films increase until conductivity is cut off at a HEC:Ag ratio of 64:36 by volume. At this composition the percolating network of silver particles is disrupted by the HEC polymer film. **Figure 3.8b-c** compare the morphologies of cast films with lowest (18:82) and highest (64:36) HEC content. In the first film, the SEM micrograph reveals that there are particle-particle contacts and that globules of the dried polymer cling to the exposed surfaces. In SEM micrograph of the polymer rich film, on the other hand, the HEC matrix is clearly visible between the particles and the continuous network of particles is disrupted.

3.3.3 Carbon Inks

Carbon inks are composed of carbon nanoparticles that form high-structure branched aggregates. The microstructure of the carbon particles, as well as an ink film, are shown in **Figure 3.9a-c**. The constituent nanoparticles are approximately 20 nm in diameter, and the aggregates shown are up to 600 μm in one dimension.

The carbon ink contains a HEC:carbon ratio of 1:1 by weight (∼2:1 by volume). The total solids loading is 3.6 wt% carbon (∼1.9 vol%). The electrical resistivity of the carbon ink is measured on films formed by doctor blading this material onto glass substrates and using four-point probe method. The bulk resistivity of the carbon ink is 1.86×10^2 Ω-cm.

3.3.4 Silver-Carbon Ink Blends

To create silver-carbon blends, we combined the carbon ink described above with a silver ink with 53.6 wt% silver (9.9 vol%) and a HEC:Ag ratio of 3:100. The respective compositions of each ink are confirmed using TGA, as shown in **Figure 3.10**. Note that the silver ink has a higher total solids loading than the carbon ink and the carbon ink has a higher polymer (HEC) content compared to solids in order to aid long-term particle stability.

The electrical resistivity of composite films cast from inks of varying Ag:carbon ratios is shown in **Figure 3.11a** and three examples of blended ink films are shown in **Figure 3.11b**. A visible gradient in film color between uniform gray (100% silver) and uniform black (100% carbon) can be observed. The electrical resistivity of the silver-rich films (0-30% carbon) increases slowly with increasing carbon content. Between 30 and 40 vol% carbon, there is a dramatic rise in the electrical resistivity of the composite films, which we attribute to a reduction in the percolative network between silver particles caused by both increased carbon and HEC content. The electrical resistivity of the carbon-rich films (50-100 vol% carbon) gradually plateaus to a value of 1.86×10^2 Ω-cm, which is the bulk conductivity of the 100% carbon (0% silver) ink film.

3.4 Conclusions

We have created conductive silver and resistive carbon inks with highly tunable rheological properties, printing behavior, and electrical resistivity. We find that both their solids loading and HEC content has a strong influence on these properties. Both inks, as well as their blends, can be used for rollerball pen writing and direct ink writing, which will be described in detail in **Chapters 4 and 5**, respectively.

3.5 Tables

Table 3.1: Composition of conductive silver inks. *Ink index # is the weight percentage of silver in the ink, as mixed. **The value in parentheses is the concentration of HEC in the viscous HEC-water carrier fluid in g/ml.

Ink index # *wt% silver*	Silver conc. *vol% silver in ink*	HEC conc. *vol% HEC in ink*	Water conc. *vol% water in ink*
35*	4.9	1.1 (1.6)**	94.0
40	6.0	1.4 (2.0)	92.6
45	7.3	1.6 (2.4)	91.1
50	8.8	2.0 (3.0)	89.2
55	10.5	2.4 (3.6)	87.1
60	12.7	2.8 (4.5)	84.5
65	15.3	3.4 (5.6)	81.3

Table 3.2: Carreau (η_o, λ, and n) and power-law fluid (m and n) fitting parameters. *Ink index # is the weight percentage of silver in the ink, as mixed.

Ink index # *wt% Ag*	η_o *Pa-s*	λ *seconds*	m *(Pa-s)^n*	n -
40*	0.3	0.055	0.76	0.681
45	0.8	0.090	2.0	0.612
50	2.1	0.115	5.6	0.547
55	5.0	0.145	15.3	0.467

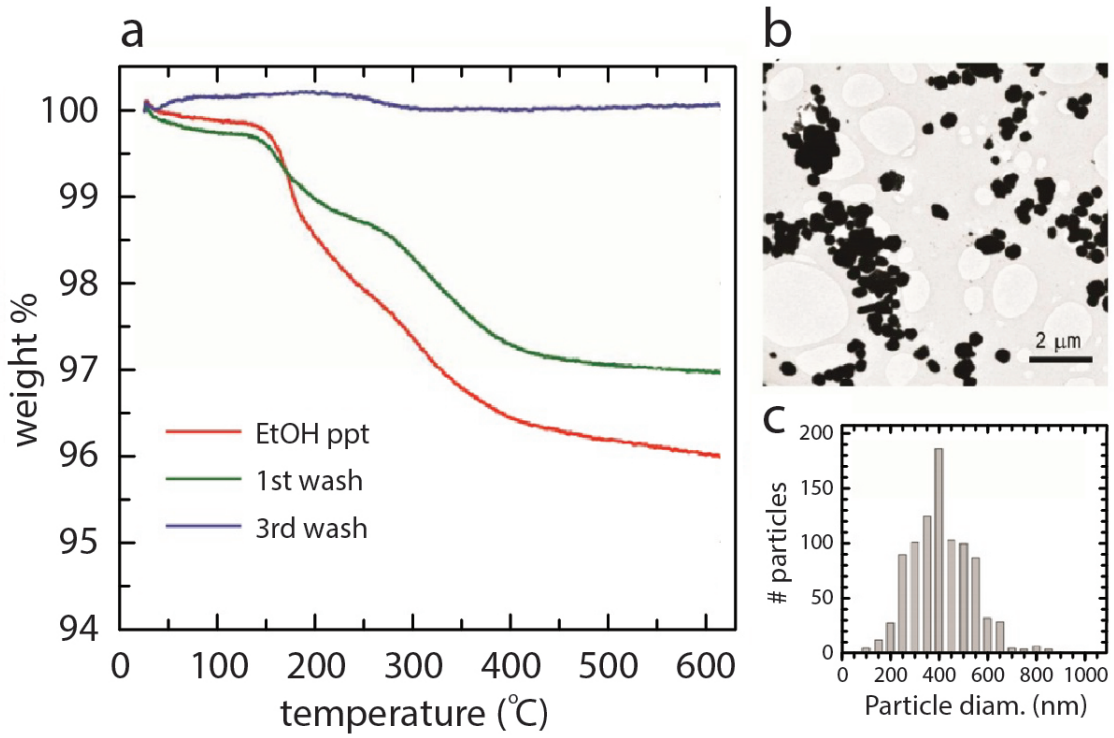

Figure 3.1: Silver ink synthesis. (a) Thermogravimetric analysis (TGA) of the precipitate of the PAA-capped particles with ethanol (red), and after the first (green) and third (blue) washing steps. (b) TEM image of colloidal silver particles present in the ink solution after ripening at 65C for 1.5 h. (c) Plot of average particle size distribution determined from TEM micrographs.

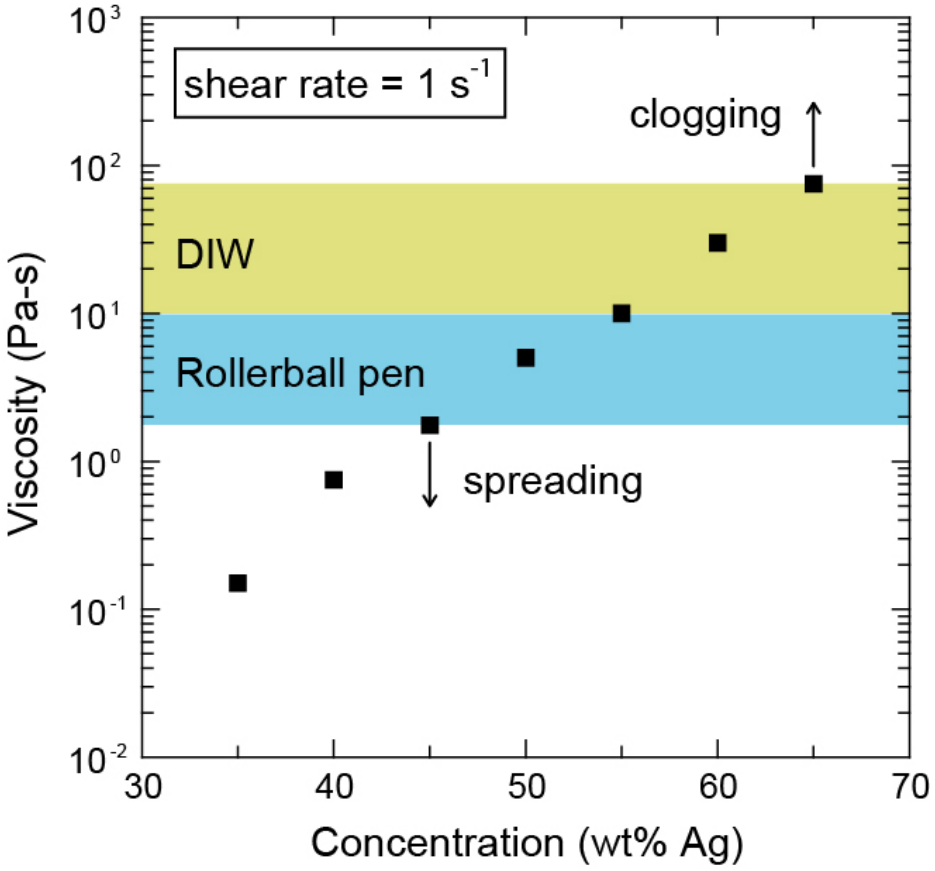

Figure 3.2: Apparent viscosity of conductive silver inks composed of HEC:Ag ratio of 3:100 as a function of silver particle concentration. Shear rate is $1s^{-1}$.

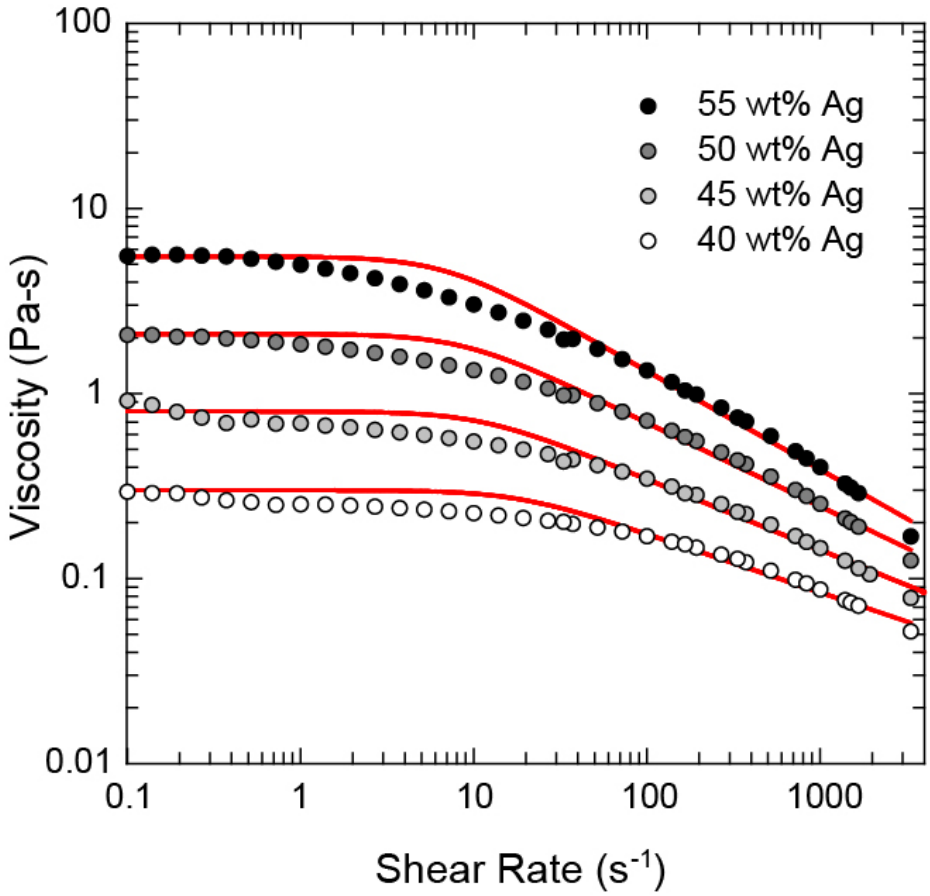

Figure 3.3: Apparent viscosity as a function of shear rate for silver inks of varying silver content. The red lines are a fit of the Carreau model. Fitting parameters are listed in **Table 3.2**

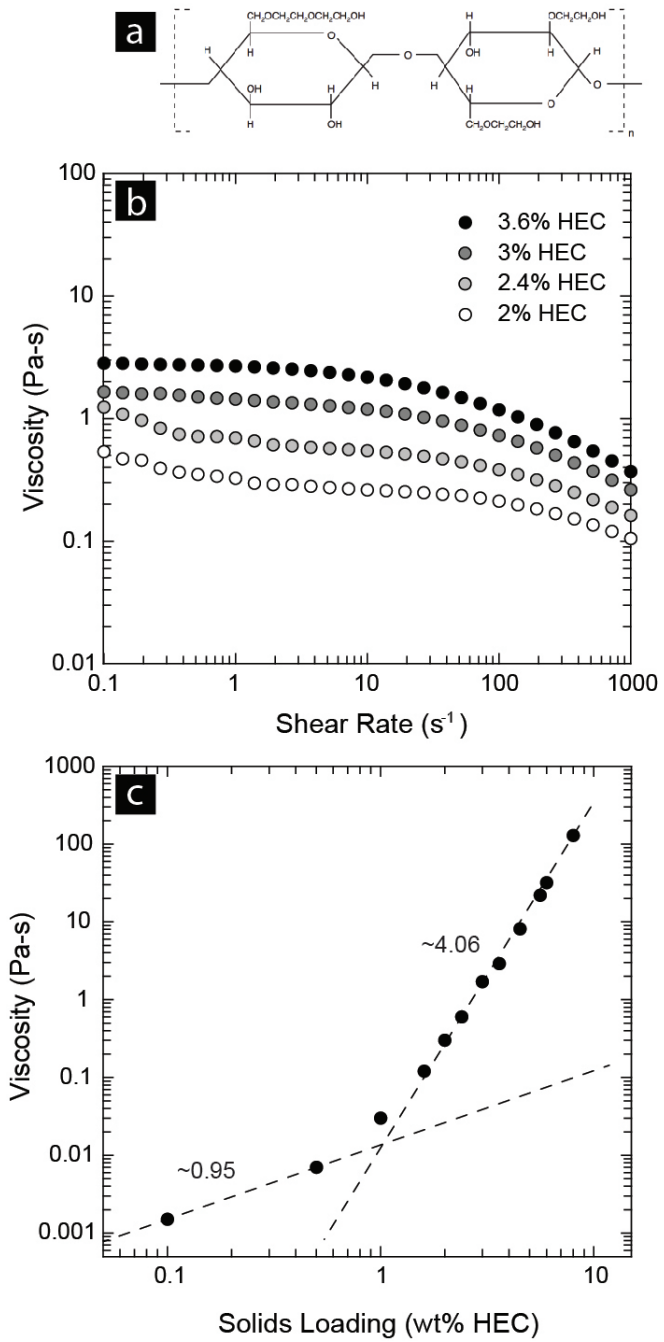

Figure 3.4: HEC structure and rheology. (a) Molecular structure of a stiff HEC chain. (b) Apparent viscosity as a function of shear rate for HEC solutions of varying concentration. These concentrations correspond to silver inks used in rollerball pen writing. (c) Apparent viscosity as a function of solution concentration, sampled at the zero shear rate plateau.

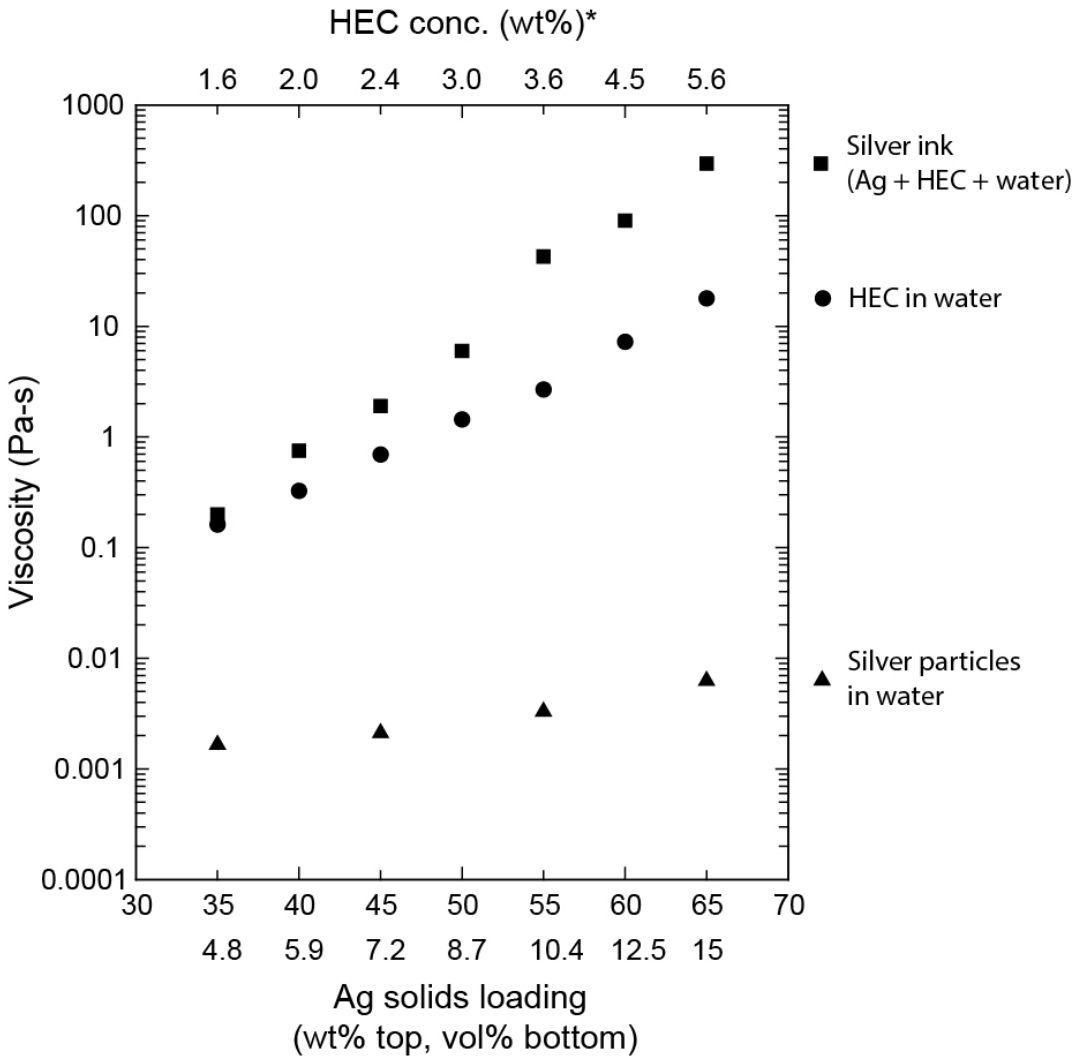

Figure 3.5: Apparent viscosity as a function of fluid composition, including silver inks as well as pure HEC and silver particle solutions. *The HEC concentrations correspond to the viscous carrier fluids of the silver inks (wt% in water).

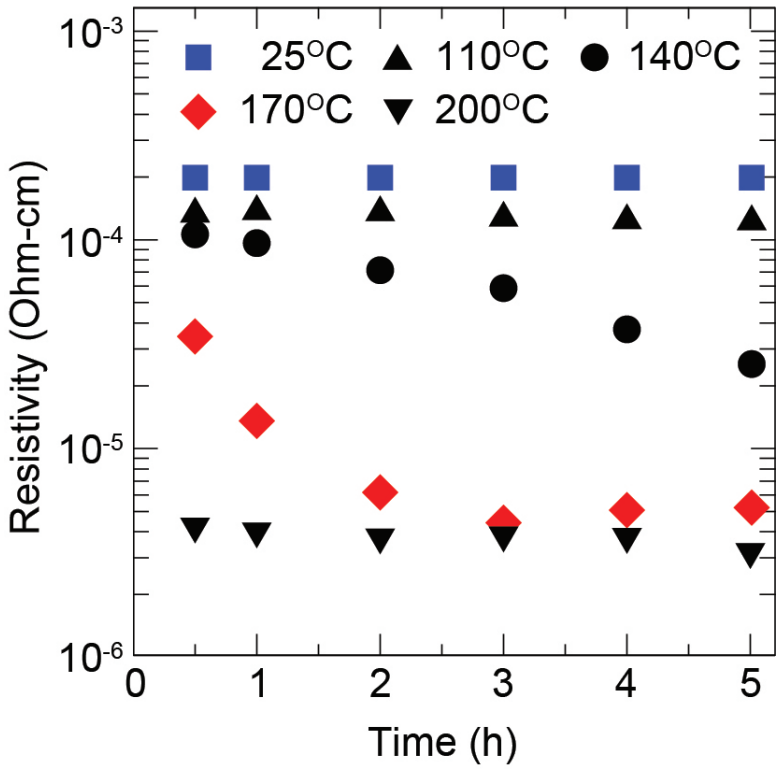

Figure 3.6: Electrical resistivity of silver inks (50 wt% silver) as a function of annealing temperature and time.

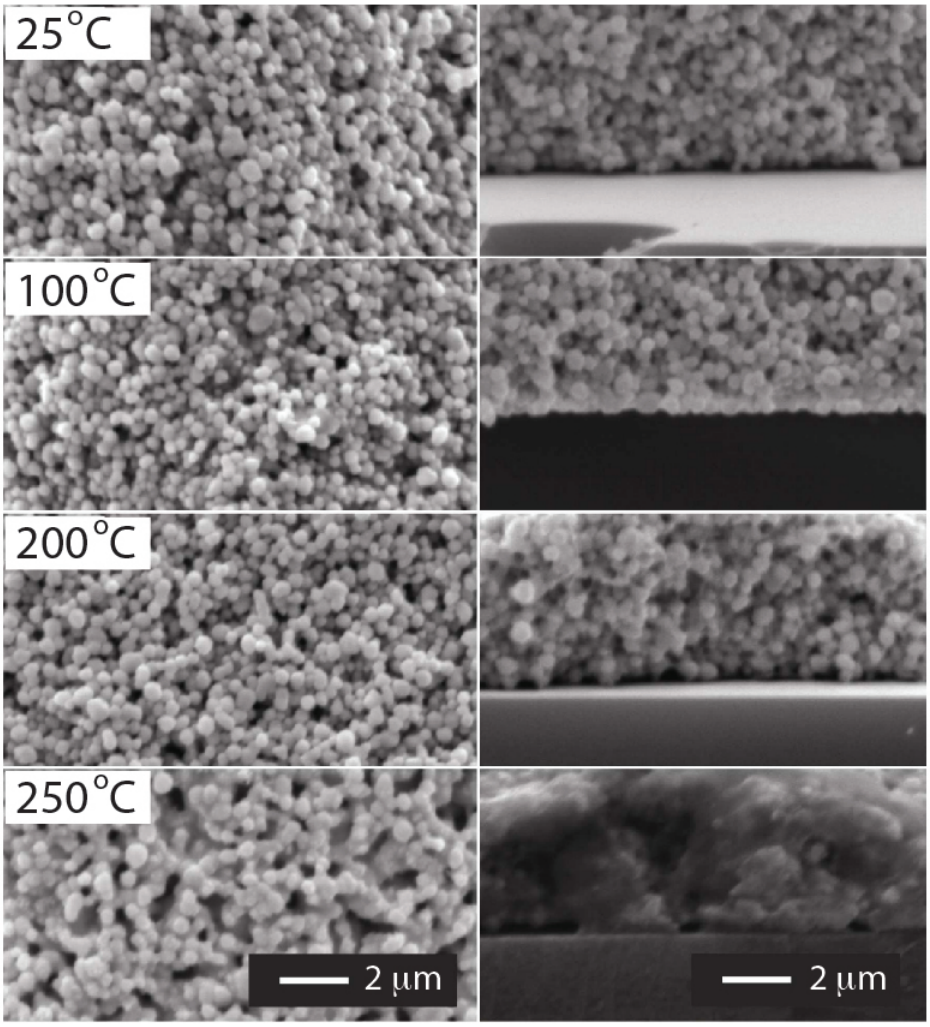

Figure 3.7: SEM images of the top and cross-sectional views of silver films dried and annealed at different temperatures.

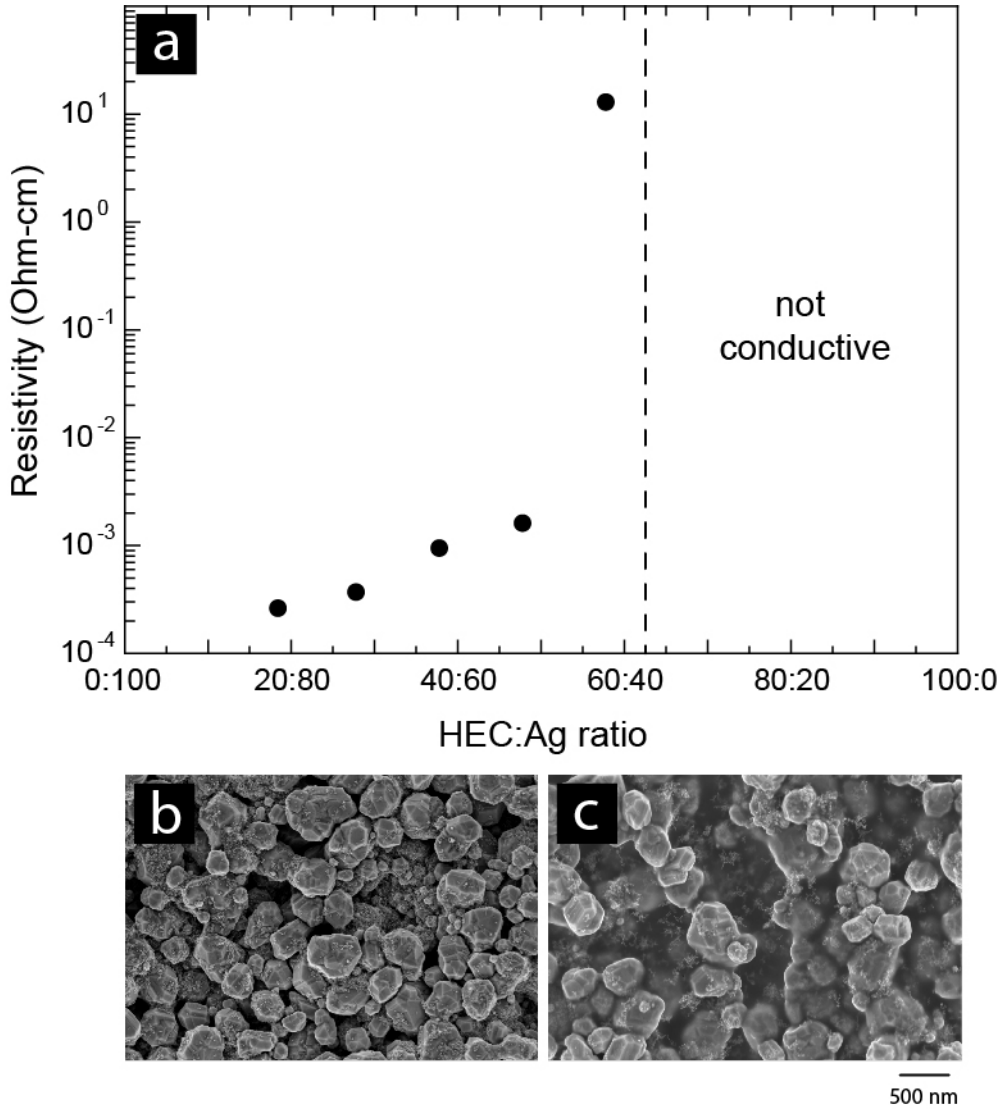

Figure 3.8: (a) Silver ink film resistivity as a function of HEC:Ag volume ratio. Films with HEC:Ag ratio of 64:36 and above are not conductive. (b) SEM micrograph of a 18:82 film (lowest HEC concentration studied). (c) SEM micrograph of a 64:36 film (highest HEC concentration studied). The HEC polymer matrix is clearly visible.

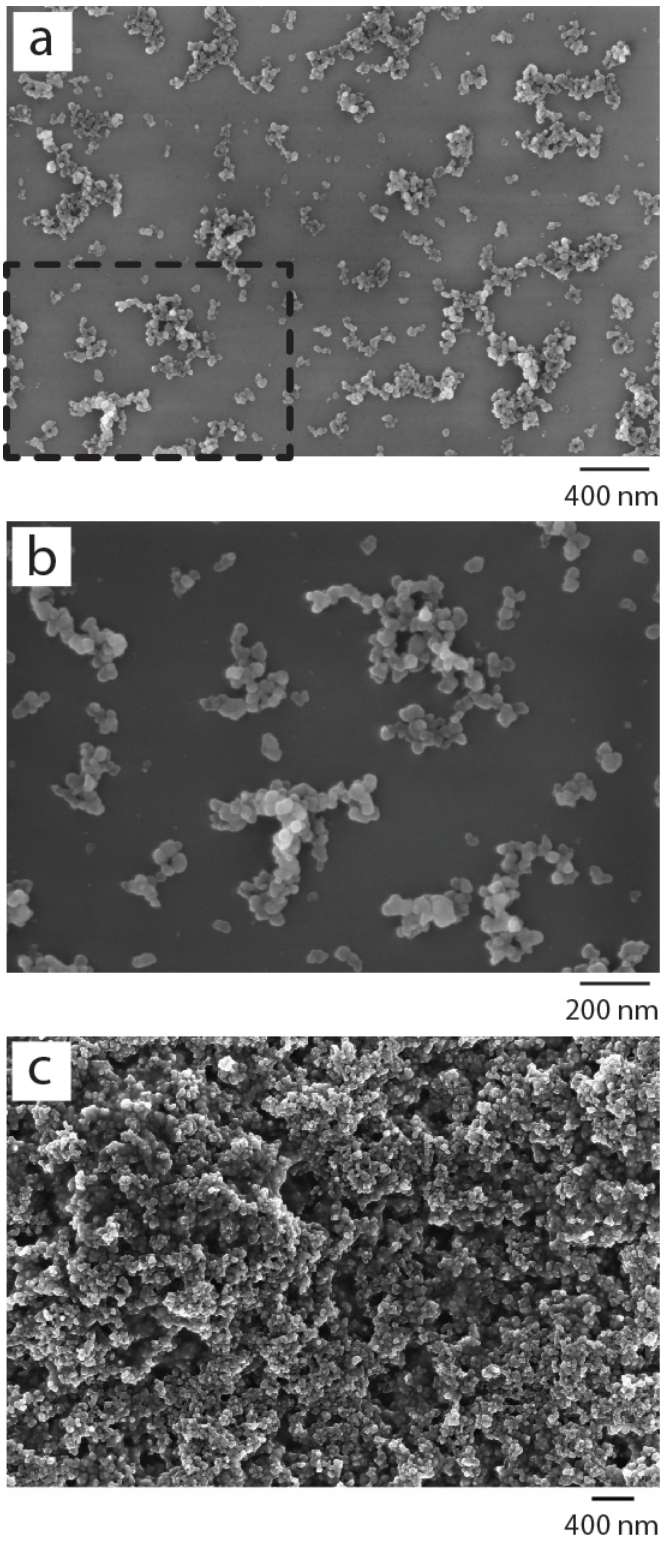

Figure 3.9: Carbon particles and cast film. (a-b) SEM micrographs of carbon nanoparticles. The constituent particles form branched aggregates. (c) A cast film of carbon ink containing HEC viscosifier.

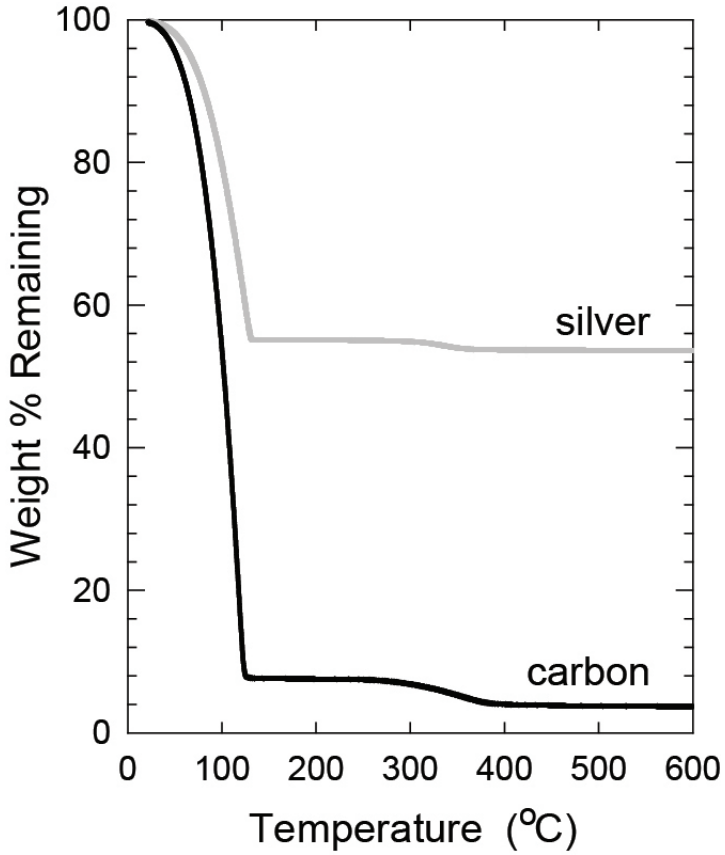

Figure 3.10: Composition of silver and carbon inks determined by thermogravimetric analysis (TGA).

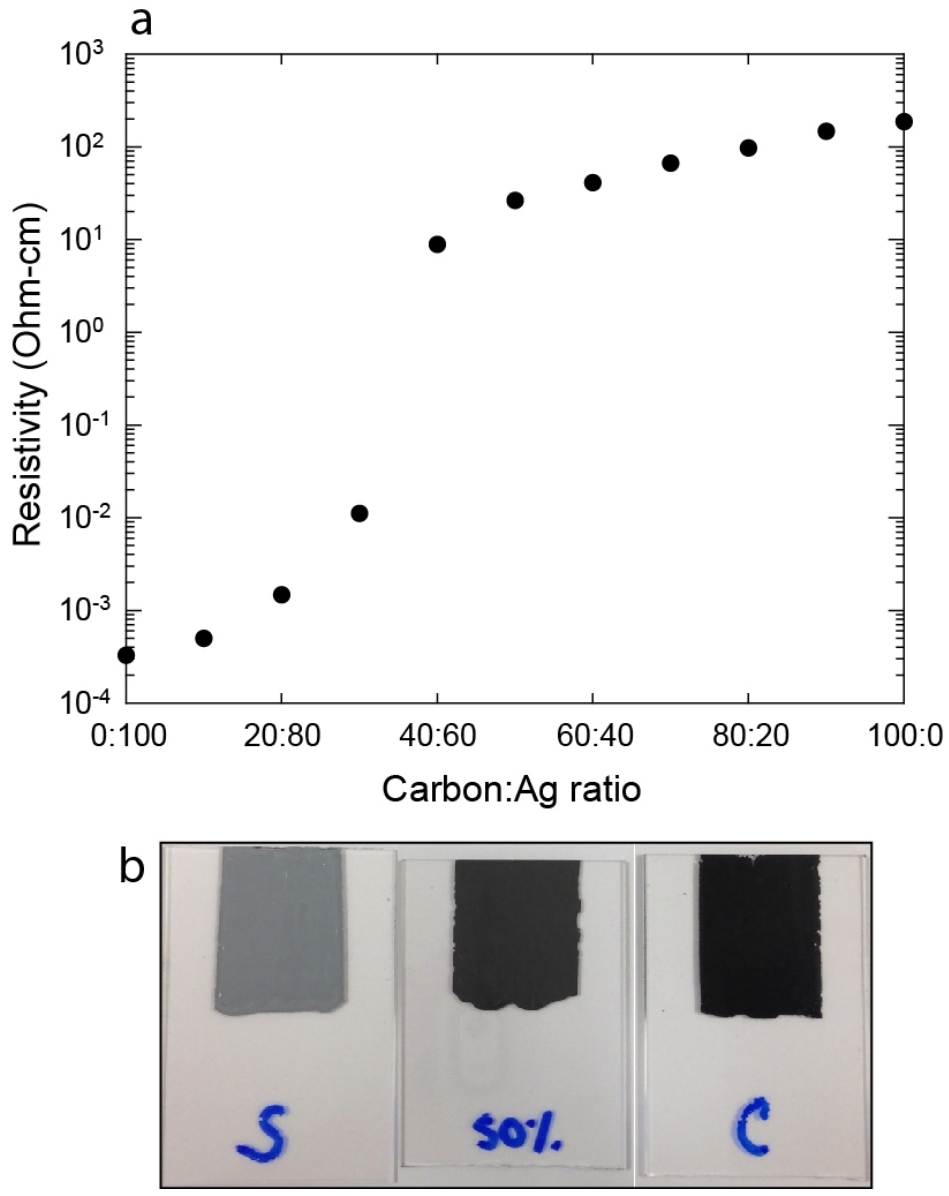

Figure 3.11: Silver-carbon ink blends. (a) Electrical resistivity of silver and carbon ink blends with compositions (carbon:Ag by volume) ranging from 0:100 (100% silver) to 100:0 (100% carbon). (b) Conductive and resistive ink films with composition 100% silver, 50:50, and 100% carbon.

3.7 References

[1] Adam C. Siegel, Scott T. Phillips, Benjamin J. Wiley, and George M. Whitesides. Thin, lightweight, foldable thermochromic displays on paper. *Lab on a Chip*, 9(19):2775–2781, October 2009.

[2] A Rida, Li Yang, R. Vyas, and M.M. Tentzeris. Conductive inkjet-printed antennas on flexible low-cost paper-based substrates for RFID and WSN applications. *IEEE Antennas and Propagation Magazine*, 51(3):13–23, June 2009.

[3] Hsien-Hsueh Lee, Kan-Sen Chou, and Kuo-Cheng Huang. Inkjet printing of nanosized silver colloids. *Nanotechnology*, 16(10):2436–2441, October 2005.

[4] Yoshihiro Kawahara, Steve Hodges, Benjamin S. Cook, Cheng Zhang, and Gregory D. Abowd. Instant inkjet circuits: Lab-based inkjet printing to support rapid prototyping of UbiComp devices. In *Proceedings of the 2013 ACM International Joint Conference on Pervasive and Ubiquitous Computing*, UbiComp '13, pages 363–372, New York, NY, USA, 2013. ACM.

[5] Frederik C. Krebs, Mikkel Jrgensen, Kion Norrman, Ole Hagemann, Jan Alstrup, Torben D. Nielsen, Jan Fyenbo, Kaj Larsen, and Jette Kristensen. A complete process for production of flexible large area polymer solar cells entirely using screen printingfirst public demonstration. *Solar Energy Materials and Solar Cells*, 93(4):422–441, April 2009.

[6] Kamran ul Hasan, Omer Nur, and Magnus Willander. Screen printed ZnO ultraviolet photoconductive sensor on pencil drawn circuitry over paper. *Applied Physics Letters*, 100(21):211104, 2012.

[7] Analisa Russo, Bok Yeop Ahn, Jacob J. Adams, Eric B. Duoss, Jennifer T. Bern-

hard, and Jennifer A. Lewis. Pen-on-paper flexible electronics. *Advanced Materials*, 23(30):3426–3430, August 2011.

[8] Bok Y. Ahn, Eric B. Duoss, Michael J. Motala, Xiaoying Guo, Sang-Il Park, Yujie Xiong, Jongseung Yoon, Ralph G. Nuzzo, John A. Rogers, and Jennifer A. Lewis. Omnidirectional printing of flexible, stretchable, and spanning silver microelectrodes. *Science*, 323(5921):1590–1593, March 2009.

[9] Juha Niittynen, Robert Abbel, Matti Mntysalo, Jolke Perelaer, Ulrich S. Schubert, and Donald Lupo. Alternative sintering methods compared to conventional thermal sintering for inkjet printed silver nanoparticle ink. *Thin Solid Films*, 556:452–459, April 2014.

[10] Jacob J. Adams, Eric B. Duoss, Thomas F. Malkowski, Michael J. Motala, Bok Yeop Ahn, Ralph G. Nuzzo, Jennifer T. Bernhard, and Jennifer A. Lewis. Conformal printing of electrically small antennas on three-dimensional surfaces. *Advanced Materials*, 23(11):1335–1340, March 2011.

[11] Tony Whelan. *Polymer Technology Dictionary*. Springer Science & Business Media, 1994.

[12] CELLOSIZE hydroxyethyl cellulose. Technical data sheet, DOW Chemical.

[13] Faith Morrison. *Understanding Rheology*. Oxford University Press, 2001.

CHAPTER 4

PEN-ON-PAPER ELECTRONICS

4.1 Introduction

The Pen-on-Paper flexible electronics (P-o-P) platform enables rapid patterning of electronic devices on paper using rollerball pens filled with conductive silver and resistive carbon inks. Using this platform, paper electronics can be created on-the-fly either by drawing by hand or using an inexpensive pen plotter.[1] To realize this vision, we first created functional inks required for patterning conductive and resistive features, as described in **Chapter 3**.

We identified the optimal pen and paper combination to ensure uniform printed features. We find that rollerball pens, which are available with many tip sizes ranging from 250 μm to 1 mm, are well suited for dispensing the functional inks. Specifically, the Gelly Roll Metallic pen, with a 960 μm tip, is a precision-machined applicator that enables the flow of large glitter or pigment particles. We find that traces printed on photo paper dry quickly and have uniform outlines. Semi-gloss or luster photo inkjet paper offers an ideal writing surface, which is nominally smooth, yet contains micropores which quickly wick ink solvents away from the surface. Together, the rollerball pen and photo paper serve as a model system for studying patterning dynamics.

We investigated the effects of ink rheology and printing speed on printed feature uniformity to ensure uniform and repeatable printed interconnects and resistor elements. Above a critical writing speed, we find that the ink breaks up into multiple menisci, due to the well known printers instability.[2–4] By optimizing the ink composition, rheology, and printing speed, we demonstrate that this platform can be used to create myriad electronic devices including tactile and visual user interfaces, circuits for signal processing, and a programmable paper Arduino circuit board.

Finally, we created auxiliary magnetic connectors to facilitate fabrication of programmable devices including capacitive touch pads, LED arrays, high-pass and low-pass analog filters, and a fully functional paper-based Arduino board fabricated with a desktop pen plotter. The Pen-on-Paper Electronics platform is well suited for use in circuit prototyping, electronic art, and STEM education.

4.2 Experimental Methods

4.2.1 Ink Properties

The apparent viscosity of conductive silver inks is presented in **Chapter 3**. The surface tension of the conductive ink is measured as a function of silver concentration (40 - 60 wt% silver) using the Kruss Drop Shape Analyzer DSA100B with accompanying software. The pendant drop method is employed, in which ink droplet formation from a 510 μm diameter nozzle is imaged and droplet volume is subsequently measured.

4.2.2 Controlled Printing

Rollerball pens (960 μm diameter ball tip) filled with conductive ink of varying silver concentration (40 – 55 wt% silver) are mounted on a custom spring-loaded pen plotter, which maintains contact between the pen tip paper substrate during printing. The same applied pressure is used for all experiments, which allows the pen to write continuous lines on paper without forming a trough-like impression. The pen and holder are translated in the x-y plane by a precise motion-controlled stage (Aerotech) at speeds between 1 and 100 mm/s (i.e., 1, 5, 10, 25, 50, 100 mm/s). The ink meniscus that forms at the trailing edge of the ball tip is observed using a camera attached directly to the printhead, which is translated at the same speed pen tip. The pen tip is cleaned of any built-up residue between printing each line. Printing experiments are performed on both standard printer paper (Office Max 20 lb Copy Paper, 92 bright) and on a model paper (Epson Ultra Premium Photo Paper, Luster), which is composed of a textured polymer film laminated on cardstock.

4.2.3 Printed Feature Morphology

The printed line width and uniformity are assessed using an optical microscope (Leica). To quantify the degree of line edge roughness, image analysis is carried out using Matlab. Each micrograph is converted to a black and white image to highlight the edges of the trace. The high contrast between the dark silver ink and white paper enables a crisp representation of the trace silhouette. Each image is analyzed to obtain the dark pixel count, which represents the coverage of silver ink in each printed trace; a rough line border has <100% coverage by dark pixels.

To assess the extent of ink absorption by the paper, micro computed tomography (micro-CT, Xradia, 40 kV, 8W, 200 μA) is used to obtain three-dimensional representations. The large mismatch between silver and paper densities results in a high contrast representation of the penetration depth of silver ink through the paper fibers. The images are rendered using TXM 3D Viewer and Amira.

4.2.4 Electrical Characterization

The electrical resistance of hand drawn and robotically printed conductive traces is measured using a handheld digital multimeter (Fluke). To assess typical ink drying times on standard Xerox and model photo paper, a series of teardrop shaped electrodes are printed with a silver ink-filled rollerball pen mounted in a desktop pen plotter (Silhouette SD plotter). The test strip is mounted on a steel backing and the leads of a digital multimeter unit (Agilent 34405A) are attached to the test electrodes with magnets. Upon drawing a 4cm long trace between the electrodes using conductive inks of varying silver content (40 – 55 wt% silver), the resistance of the patterned line is continuously measured as the ink dries and the silver concentration within each trace increases.

4.2.5 Mechanical Characterization

To investigate the mechanical integrity of the printed features, we printed a linear array of five silver electrodes (width = 620 μm, and length = 1.5 cm) on paper, which are dried for

24 h at room temperature. The electrode-patterned substrates are then actuated between flat and bent states at a bending rate of 2 cm/s to a specified minimum bend radius (0.5, 1.6 or 2.9 mm) using a custom-built mechanical stage coupled to a computer-controlled 3-axis micropositioning system (Aerotech).[1] The resistance of the printed traces are measured by a handheld digital multimeter (Fluke) after every 500 bend cycles and the trace morphology of both a fresh test strip and a strip actuated 10,000 times is observed using SEM.

4.2.6 Pen-on-Paper Device Fabrication

Electronic Art

An artistic drawing is created by hand using a silver ink-filled rollerball pen (960 μm ball diameter).[1] A paper substrate is prepared by first printing a background color on Xerox paper (Domtar Laser copy Paper, 92 White, 75 g/m^2) using a conventional inkjet printer. As an example, we traced the famous painting Sae-Han-Do by Jung Hee Kim. The printed silver features that overlap form a conductive network upon drying under ambient conditions. The printed feature size is dependent upon writing pressure and speed and ranges from 300 m to 1 mm in width. A surface-mount LED (1.25 mm 2 mm 0.8 mm) is placed within the gap left in a printed pattern. The LED is connected to the patterned conductive features by placing a drop of concentrated silver ink (65 wt% solids loading) on the terminals of the device.

LED Display

To demonstrate large-area flexible paper displays, we fabricated a multi-color 2516 LED array. Specifically, a series of parallel ground lines with a 4 mm center-to-center spacing are printed on a Xerox paper using a silver ink-filled rollerball pen (50 wt% solids loading). These lines are crossed by strips (1.5 mm wide) of adhesive-backed paper containing single silver electrodes (the adhesive paper insulates the power and ground traces) and additional electrodes hand-drawn to accommodate the specific surface mount geometry (LEDs, Avago Co., 1.25 2 0.8 mm). The surface-mount LEDs are adhered to the substrate by placing a drop of superglue on the backside of each LED, yielding a 1625 LED array. The electrical

connections between the LED electrodes and silver traces are reinforced using a drop of concentrated silver ink (65 wt% solids) at each terminal. Although the voltage and current ratings of these LEDs differ by color, they can be integrated into an array powered by a single 9 V battery.

Programmable Display and Capacitive Touch Pad

We have designed magnet-based connectors that interface P-o-P devices with external hardware such as the Arduino platform. Custom connectors are composed of laser-cut acrylic strips or frames with 1/8 inch circular holes that contain cylindrical neodymium magnets via press-fit construction. The nickel-coated magnets provide both mechanical and electrical connection to the printed devices when working on a steel topped table or another magnetic surface.[5] From each cylindrical magnet, individual surface mount components, wires, or pin headers can are attached through press-fit construction and reinforced with epoxy. This construction method can be scaled for a wide range of connector geometries.

To demonstrate the fabrication of programmable P-o-P devices, we first constructed an 8×8 LED display with individually addressable pixels, and a corresponding acrylic and magnet mount consisting of a square frame with eight vertically oriented and eight horizontally oriented magnets. Similar to the construction of the large-scale display, a series of parallel ground lines with a 4 mm center-to-center spacing are printed on copy paper using a silver ink-filled rollerball pen and these lines are crossed by strips (1.5 mm wide) of adhesive-backed paper containing single silver electrodes. Unlike the construction of the large display, surface mount LEDs (1206 package) are then mounted onto each crossed electrode at a 45° angle. LEDs are adhered to the display using superglue between the electrodes and the connections are reinforced with conductive epoxy (Resinlab). The corresponding magnetic mount has wires that map each magnet to a single pin on an Arduino MEGA.

As a second example, we constructed a capacitive touch pad by drawing silver traces on paper. The connector cable for the touch pad consists of a laser cut acrylic plate with five nickel-coated magnets embedded in it. Each of these magnets connects to a header pin that branches into a wire and a 100 kΩ resistor. The opposite end of the cable is connected to ten pins on an Arduino MEGA board that are programmed to function as capacitive sensors.

The traces connected to the pins are simply five conductive keys; touching one or two of the keys at a time changes the time constants of the contacted capacitive sensors, which in turn triggers an output on the LED display described above.[6]

Three-Dimensional RF Antenna

The rollerball pen approach is used for printing and folding three-dimensional (3D) antennas. In one example, radiating antenna traces are composed of eight tapered meanderline arms (650 μm width, 1 mm center-to-center spacing).[7] The meanderline arms are hand drawn by silver ink-filled rollerball pen on adhesive-backed paper using faint inkjet printed nonconductive patterns as guidelines. The pattern was cut to into a pinwheel shape and conformally adhered to the surface of a hollow glass hemisphere (12.7 mm radius). The 3D antenna is completed by attaching the hemisphere to a low-loss laminate substrate (DuroidTM 5880, Rogers Corp.) with copper feedlines. The antenna traces are connected to the feedlines using conductive epoxy.

Reflection coefficient measurements are taken using a vector network analyzer (E8363B, Agilent Technologies)[1]. After recording its radiation characteristics, a Wheeler cap is placed over the antenna and electrical connection to the ground plane is ensured. The Wheeler cap is a metallic box that shorts out the antennas far-field radiation, enabling separate measurement of the radiation and loss mechanisms. A variety of Wheeler cap sizes are explored to avoid cavity resonances that result in erroneous measurements in certain frequency ranges. Using the measurements from the Wheeler cap and free-space, the efficiency is calculated using methods from the literature.[1, 7]

RC Filters

We created simple resistor-capacitor (RC) circuits by drawing conductive and resistive inks on copy paper, with no additional pre-manufactured components attached. The circuits utilize silver conducting lines, a carbon resistor, and a paper capacitor. Paper capacitors are constructed by printing a square patch of silver ink on paper through a stencil; the patch is then overlaid with a strip of adhesive-backed paper and another electrode of the same size is

[1]Antenna characterization work was performed by Jacob J. Adams.

drawn on the top surface. Five capacitor areas ranging size from 0.5 to 1.5 cm edge length are tested using a digital power supply in capacitance mode (Agilent).

In the RC circuit, the carbon resistor and silver/paper capacitor are arranged in series and the circuit acts as either a low-pass or a high-pass filter, depending on the orientation of the electrodes.[9] In the low-pass filter orientation, an input sine waveform (V_{in}, amplitude 500 mV) is applied across the entire circuit using a function generator (Agilent). An output waveform is measured by oscilloscope (Tektronix) across the capacitor component. Conversely, when the circuit operates in a high pass filter mode, the output signal is measured across the resistor component. In both configurations the input waveform is a sine wave and takes on frequencies between 50 Hz and 100 kHz.

4.2.7 Paperduino

We mounted a conductive ink–filled rollerball pen on an inexpensive craft plotter (Silhouette SD Plotter) and fabricated an intricate programmable circuit board. We printed conductive traces for an Arduino Pro Mini on glossy photo paper and populated the circuit with surface-mount components. The schematic for an Arduino Pro Mini is first modified in circuit board design software (EAGLE CAD) to be printable in a single layer format.[8] We added large round pads in the location where pin headers usually reside on a rigid printed circuit board; the large pads allow connection of input and output devices (sensors, LEDs, etc.) with magnets or alligator clips. Next, an exported DXF file is loaded into the Silhouette SD plotter software, where it is properly re-sized. The slowest printing speed (10 mm/s) is selected and the entire circuit pattern is printed in a single step. During printing, the Silhouette SD plotter software doubles over the printed lines, which serves to improve the trace conductivity.

Surface mount components, including LEDs, resistors, capacitors, and a 32–pin integrated circuit are hand–placed in the circuit.[10] In the first attachment method, a small drop of superglue is placed between the pads and the component is pressed down. This method alone provides electrical contact between the component and traces. To reinforce the traces and make the circuit more robust to flexing and bending, the connections are reinforced

by pumping conductive epoxy over the junction with syringe or electric fluid dispenser. In another attachment method, a strip of z–axis conductive tape (Z-tape, 3M) is placed over several component pads at the same time and the components are placed on top.[9] Instructions for creating the Paperduino are presented in **Appendix A**.

4.3 Results and Discussion

4.3.1 Pen-on-Paper Patterning

We investigated the rollerball pen writing mechanism to ensure optimal device fabrication. Specifically, we aimed to understand how the ink properties, writing speed, and paper surface texture control ink flow through the pen tip. Commercial rollerball pens containing viscous water-based gel ink are available with ball diameters ranging from 250 to 960 μm.[10] The ball tip floats in a cavity that is slightly larger than the ball bearing ($\sim$30 μm gap). SEM images of the 960 μm ball tip of the Sakura Gelly Roll pen are shown in **Figure 4.1**. During printing, the ink is supplied to the tip via capillary forces and gravity. The ink lubricates the ball tip and is transferred from the ball to paper. Rotation of the ball tip relies on friction between the ball bearing and the rough paper substrate. As such, rollerball pens do not deposit ink on slick surfaces and are highly suited for paper substrates.

We find that silver inks with a solids loading of 45-55 wt% are printable using a Sakura Gelly Roll rollerball pen with 960 μm ball tip.[1] The apparent viscosity of inks composed of 40, 45, 50, and 55wt% silver as a function of shear rate is provided in **Figure 3.3** (**Chapter 3**). Inks with viscosities of 0.1-10 Pa-s (measured at a shear rate of $1s^{-1}$) reliably flow through the ballpoint tip without leaking, skipping, or clogging. Notably, three commercial gel inks evaluated (Sakura and Pilot brands) are also strongly shear thinning (**Figure 4.2**).

A summary of ink properties as a function of solids loading (40, 45, 50, and 55 wt% silver) is provided in **Table 4.1**. The ink density is calculated directly from the constituent components of the ink (ρ_{Ag} = 10.49 g/ml and $\rho_{water-cellulose}$ = 1.0 g/ml). The ink density ranges from 1.567 (40 wt% silver ink) to 1.99 g/ml (55 wt% silver ink). The surface tension of the ink ranges from 64 to 57 mN/m, which is lower than pure water (72 mN/m). Variations

in surface tension of this magnitude are consistent with reported values for HEC viscosifier solutions of various concentration[11].

To determine the range of characteristic shear rates associated with rollerball pen writing, typical printing speeds are measured by directly evaluating lines that were hand-drawn with a commercial rollerball pen. Writing of both straight and wavy lines is observed with a video camera and the video is analyzed to measure the characteristic writing time for each trace drawn. The range of characteristic printing speeds is determined by the ratio of *contourlength / writingtime*. We found that a typical writing speed is roughly 50 mm/s. To determine the spacing between the steel rollerball tip and its housing, we observed a polished cross-section of the rollerball tip as well as SEM images of the intact rollerball tip (**Figure 4.1**). We estimate that the gap is $\sim$30 μm wide at its narrowest point. Using this information, we can represent the flow of ink between the ball tip and housing as Couette flow between two plates. **Eq. 4.1** represents the boundary conditions for ink flow: the ink is stationary at edge of the pen tip and flows with velocity V at the ball bearing, which rotates at the same speed as the pen writing. **Eq. 4.2** indicates that the flow of ink occurs only parallel to the rotating ball. **Eq. 4.3** represents the velocity of the ink at all distances y between the two surfaces with respect to the gap spacing h. The maximum shear rate occurs at the moving boundary (the ball tip) and is equal to U/y, yielding **Eq. 4.4**. Based on the measured printing speed and gap width, we estimate that these inks experience a typical shear rate ($\dot{\gamma}$) of $\sim$1666 s^{-1} during writing.

Boundary conditions:

$$U(0) = 0; U(h) = V \tag{4.1}$$

$$\frac{d^2U}{dy^2} = 0 \tag{4.2}$$

$$U = V\frac{y}{h} \tag{4.3}$$

Maximum shear rate:

$$\dot{\gamma}_m = \frac{V}{h}[s^{-1}] \tag{4.4}$$

4.3.2 Meniscus Formation

In roller-based printing methods, multiple menisci can form above a critical rotation speed, resulting in the formation of ridges or stripes in a printed feature. This phenomenon is commonly referred to as the "Printers Instability."[12] In pioneering work by Pitts and Greiller,[4] two rollers are submerged in a Newtonian fluid and rolled in opposite directions. In each test, the critical speed for meniscus formation is found. The study compares the product of velocity (V), viscosity (η), and roller radius (R) to the product of surface tension (σ) and separation distance (d). For all combinations of roller size, fluid viscosity, and surface tension, the critical rotation speed is related to the capillary number (Ca) of the system:

$$Ca = \frac{\eta V}{\sigma} \tag{4.5}$$

Their study demonstrated that instability occurs when the ratio $\eta VR/\sigma T$ or CaR/T is equal to 10 (R = roller radius, T = roller spacing).

The three-dimensional problem, which relates to a lubricated ball bearing, is significantly more complex. Bico *et al.* conducted an experimental study of instability formation when a ball bearing rolls down a lubricated inclined plane (**Figure 4.3**).[13] In these experiments, a flat plane is coated with a Newtonian fluid and a metal ball bearing slides down the coated

plane. Under certain conditions, two finlike menisci form on the trailing end of the rolling bearing. In their experiment, the speed of the rolling ball is determined by the angle of the inclined ramp. The results indicate that a transition between a "circular" meniscus (a round meniscus at the bottom of the ball) to a "cusp" meniscus (two finlike ridges) occurs near translation speeds where the capillary number (Ca) of the system is approximately equal to 1. In addition to observing a change in meniscus shape, there is also a step increase in the speed of the ball translation as the incline of the plane increases; the capillary pressure of the cusp meniscus is smaller than that of the circular meniscus, thus reducing the drag on the ball bearing.

To assess the effects of ink composition, rheology, and printing speed on the morphology of printed lines, we set up an automated test rig that allows direct visualization of the meniscus shape at the trailing edge of the ball tip during printing. We find that a balance between viscous and surface forces determines the shape of the meniscus as well as the corresponding morphology of the printed traces on model paper (Epson Luster photo paper). In addition, a strong solvent wicking effect on the model paper may increase the local viscosity of ink around the ball tip, which complicates our analysis. Still images of meniscus formation at the trailing edge of the ball tip are shown in **Figure 4.4**. Conductive silver inks with solids loading of 40, 45, 50, and 55 wt% silver are printed on model paper using a robotic stage that moves the pen at speeds of 1, 5, 10, 25, 50, and 100 mm/sec. Under proper printing conditions, the ink and ball tip undergo a lubrication and transfer process. The two extreme conditions observed (40 wt% silver, 1 mm/s; 55 wt% silver, 100 mm/s) illustrate the limits of the appropriate ink concentration range for printing. The lowest viscosity ink (40 wt% silver) flows freely from the pen tip and at slow writing speeds, the ink pools around the tip. By contrast pens containing 55 wt% silver ink and translated at 100 mm/s are unable to adequately supply ink to the rollerball to maintain the desired lubrication ink and transfer process. In this case, the pen "skips" on the paper, leading to the formation of discontinuous printed traces. Both printing conditions are shown in **Figure 4.4**. Importantly, we observed a change in meniscus shape at high printing speeds. As shown in **Figure 4.4**, the meniscus at the trailing edge of the ball tip undergoes a clear transformation in shape from a single meniscus to a double meniscus above a critical printing speed. The critical speed, which

ranges from 10 to 100 mm/s, is demarcated by a dotted line in **Figure 4.4**. The critical speed increases as the silver content of the ink increases.

We find that the meniscus shape is dependent on ink viscosity (η), surface tension (σ), and printing speed (V), These parameters comprise the dimensionless value of capillary number (Ca), which represents a balance between viscous and surface forces in a fluid system.[13] The writing speeds of interest are 1, 5, 10, 25, 50, and 100 mm/s. The corresponding shear rates, which were calculated using the Couette flow model, are 33, 166, 333, 826, 1666, and 3333 s^{-1}, respectively and the associated viscosities are obtained from the plot in **Figure 4.5a**. The capillary number for each experiment is plotted as a function of printing speed in **Figure 4.5b** and the meniscus shape associated with each experiment is marked on the plot. The transition in meniscus shape consistently occurs around $Ca = 0.1$ for each ink concentration. We can obtain a general equation for the capillary number of our ink and pen system, and the meniscus transformation threshold, using the shear thinning power law fit $\eta = m(\dot{\gamma})^{n-1}$ presented in **Ch. 3**. The intermediate expression in **Eq. 4.6** is obtained by replacing the viscosity with the shear thinning power law (parameters m and $n-1$ provided in **Table 3.2**). Next, the final expression **Eq. 4.7** is obtained by replacing the shear rate $\dot{\gamma}$ by the printing velocity, V divided by the narrow gap spacing in the pen tip, d ($\sim$30 μm). The threshold occurs when this value is equal to 0.1.

$$Ca = \frac{m(\dot{\gamma})^{n-1}V}{\sigma} \tag{4.6}$$

$$Ca = \left(\frac{mV}{\sigma}\right)\left(\frac{V}{d}\right)^{n-1} = 0.1 \tag{4.7}$$

There is an anomalous double meniscus that forms for the 55 wt% silver ink at a printing speed of 1 mm/s. We believe that the observed meniscus instability arises from the balance of viscous and surface forces, but is also complicated by the rapid absorption of ink and solvent into the paper. The phenomenon has not been systematically explored, however one would expect a rapid rise in viscosity as the ink makes contact with the paper, thus increasing the viscosity and, concomitantly, the value of Ca in all experiments. This effect is further addressed in the next section.

The critical capillary number at which the transition from a single to double meniscus occurs is an order of magnitude lower than that observed by previous studies. However, there are several important differences between our rollerball experiments and the two systems studied previously: (1) the rollerball diameter is less than 1 mm, (2) the ink is fed to the ball tip from an internal reservoir, (3) the conductive ink is non-Newtonian, and (4) the writing surface is highly porous.

4.3.3 Ink Drying Kinetics

The drying time of conductive ink (50wt% silver) patterned on two types of paper is quantified by measuring the electrical resistance of the traces after writing. The resistance of a freshly drawn line (4 cm) is plotted as a function of time for the two types of paper in **Figure 4.7a**. Upon connecting the test electrodes with conductive ink on photo paper, the digital multimeter (DMM) immediately registers a measurable resistance, indicating that the ink solvent rapidly wicks into the paper upon contact, leaving behind a conductive particle mat. The electrical resistivity of the printed ink trace continues to decrease over a period of 5 minutes due to a combination of additional wicking and water evaporation. By contrast, ink drawn on standard Xerox paper remains insulating for approximately 10 seconds before the DMM registers a resistance measurement. High magnification images of Xerox and photo paper reveal their distinct surface textures, as shown in **Figure 4.7b-c**. The nominally smooth photo paper actually consists of a polymer film with micropores that rapidly wick water through the surface.

The rapid solvent wicking is readily observed in the direct visualization of pen writing. At low writing speeds (1-10 mm/s), the ink drying front can clearly be seen (**Figure 4.4**). In experiments where a single meniscus is formed, the edges of the trace dry rapidly and the pointed drying front in the center of the trace extends several mm behind the ball tip. For the 50 wt% ink printed at 5 mm/s, the drying front extends 5 mm behind the pen tip, indicating that the trace dries in approximately one second after deposition. Our observations suggest that the trailing ink meniscus is rapidly increasing in concentration on time scales relevant to printing. Hence, we expect that the ink viscosity and corresponding capillary number (Ca)

will rapidly increase upon deposition. To determine whether this effect could account for the surprisingly low value of $Ca \sim 0.1$ at the onset of meniscus transformation, we performed the following analysis in which we assume a 50% reduction in water content upon printing primarily due to absorption by the underlying substrate.

First we determine the effective composition of each of the original four inks (40, 45, 50, 55 wt% silver) if half of the water is absorbed by the paper. This rapid water extraction results in increased ink compositions of 56, 62, 66, and 70 wt% silver, respectively. The adjusted ink compositions, including the respective HEC and water volume percentages, are outlined in **Table 4.2**. Next we predict the rheological properties that are associated with these concentrated ink compositions. We make an interesting observation that at the shear rates of interest to rollerball pen writing (30–3500 s^{-1}) all inks studied are in a shear thinning regime. Within this range of shear rates and ink concentrations, the increase in viscosity with solids loading roughly follows a power law function. Plots of ink viscosity as a function of silver content at the six shear rates corresponding to the controlled printing experiments are shown in **Figure 4.6a**. Power law fits, marked by dotted lines, are extended to silver concentration of 70 wt%. We use the new predicted values of viscosity of the partially dried inks to re-calculate an effective capillary number for each printing experiment outlined in **Section 4.3.2**. The resulting Ca values are shown as a function of printing speed and ink composition in **Figure 4.6b**. We observe that there is still a clear Ca threshold across which meniscus transformation occurs when partial drying is considered, however the characteristic Ca increases by about a factor of four to ∼0.4 for each ink type. We conclude that rapid absorption of water during printing is a likely factor contributing to the differences between our ink printing system an previously studied systems in which meniscus formation occurs at $Ca \sim 1.0$.[13]

4.3.4 Printed Feature Morphology

Several non-uniformities can arise in the printed traces, including skipping, smudging, or the buildup of ink at the edges with a bare strip along the central axis. These defects may be acceptable for handwriting of text, but printed functional electronic devices must ideally contain traces with uniform morphology.

Double meniscus formation at high printing speed results directly in buildup of the ink at the edges of the printed line. Representative images of 50 wt% silver ink printed on both Xerox paper and Luster photo paper (model paper) are shown in **Figure 4.8a-b**. At printing speeds of 1 and 10 mm/s, the traces exhibit uniform coverage from edge to edge on both types of paper. At the highest printing speed (100 mm/s), ink accumulation leads to the formation of two parallel tracks at the trace edges. While meniscus formation is studied solely on model photo paper, a variety of paper types find use in printed electronics. The type of paper has a significant effect on the resistance and width of the printed traces. As shown in **Figure 4.8c-d**, the printed line width in Xerox paper decreases at higher speed, whereas trace width is relatively constant on photo paper. Micro-CT images of silver ink traces on both Xerox paper and Luster photo paper, shown in **Figure 4.9**, illustrate the difference in ink attachment to the two paper types. We note that the surface of the photo paper is hydrophobic, yet contains microscale pits that quickly absorb liquid. Hence, this surface pins the edges of the printed trace to a relatively constant width and draws the solvent downward through the porous coating. On the other hand, the randomly oriented fibers of the Xerox paper wick the ink outward from the central axis of the trace as well as through the top 15 μm of the fibrous mat. Since a higher volume of ink is deposited per unit length at slow printing speeds, the effective line width on Xerox paper is wider at slow speeds.

4.3.5 Electrical Properties

Observations of hand-drawn lines indicate that silver traces have a resistance of 15-60 Ω/cm. This range of values likely reflects natural variation in the speed and angle of hand writing and the differences in paper texture. The effects of print speed and paper type on silver ink

trace resistance is further studied for the conductive silver ink. Resistance increases with printing speed on both paper types, as shown in **Figure 4.8e-f**. In addition, printed lines have lower resistance on the model photo paper than on conventional Xerox paper. We find that on all paper types, silver particles form a conformal coating on the paper surface, as shown in **Figure 4.8a-b**. Papers containing microscale cellulose fibers, like Xerox paper, interrupt the conductive network, which raises the resistance of printed features. Again, the micro-CT scan acquired for 50 wt% silver ink traces drawn on both paper types illustrate the differences in ink attachment. The silver ink penetrates a maximum of 15 μm into the fibrous mat of the Xerox paper. By contrast, the printed ink traces reside on top of the photo paper's micro-textured polymer coating because only the solvent (water) is drawn through the surface (**Figure 4.9**).

4.3.6 Mechanical Behavior of P-o-P electrodes

A key advantage of Pen-on-Paper electronics is that these devices are highly flexible and can be folded to form 3D origami-based architectures.[14] To investigate their mechanical performance, hand-drawn silver ink traces are repeatedly bent to three different minimum radii of curvature. Optical images of new test specimens at minimum bend radii (r) of 2.9 mm, 1.6 mm, and 0.5 mm are shown in **Figure 4.10a**.[1] Corresponding SEM micrographs reveal that there is no noticeable crack formation or delamination during the first bend cycle (**Figure 4.10b**). We measured the electrical resistance (R) as a function of bend radius and number of bend cycles. Average values of R obtained from the five electrodes are reported in **Figure 4.10d**. For bending radius (r) of 2.9 mm and 1.6 mm, the silver electrodes exhibit a robust response over 10,000 bending cycles with a slight increase in their electrical resistance to their initial, as-printed state. For the most extreme bend radius of 0.5 mm, the electrical resistance increases gradually after many cycles. Two electrodes cracked and failed after 6,000 cycles, while three electrodes survived after 10,000 cycles. After 10,000 cycles at a bend radius of 0.5 mm, their microstructure is observed by SEM in both flat (top) and bent configurations, with bend radii of 1.6 mm (middle), 0.5 mm (bottom), respectively (**Figure 4.10c**). Repeated fatigue in a nearly folded state (r = 0.5 mm) leads to crease

formation in the underlying paper substrate in the direction perpendicular to the printed silver electrode(s). Ultimately, cracks form within the electrodes along this crease. This crease, which is barely visible in the flat (unbent) state, is easily observed when the paper is bent. Notably, upon returning to the flat state, the conductive pathway along the electrode is restored. The SEM image of the flat test strip suggests the formation of a cold joint between the two surfaces.

4.3.7 Pen-on-Paper Electronic Devices

Electronic Art

A first demonstration of our P-o-P platform is a freehand drawing of the Korean painting Se Han Do (**Figure 4.11a**). During hand writing of conductive silver ink by rollerball pen, natural variations in pressure, angle, and speed result in various line widths and weights. A lightly shaded region of the sketch can be seen in **Figure 4.11b**. The sketch is composed to accommodate a blue surface-mount LED (1206 package). Concentrated silver ink is used to bind the LED to the center of the drawing (**Figure 4.11c**) and a 9V battery is used to illuminate the LED through the conductive ink.[1] Although concentrated silver ink works as a temporary adhesive, more robust methods of component attachment have been found and are presented below.

LED Display

To demonstrate creation of large-area electronics using the P-o-P approach, we constructed a 16x20 LED array with individually addressable pixels. A schematic of the interconnect design and magnified optical images of the LED display are shown in **Figure 4.12a-b**. In this device, adhesive backed paper is used to separate the power and ground lines corresponding to each LED. The letters U-I-U-C are illuminated by turning all of the constituent pixels on at the same time using a 9V battery.[1] The text, shown in **Figure 4.12c**, is composed of four different colored LEDs (9 red, 8 green, 9 blue, and 8 orange). The pixels in the center of a block letter (for example the center of the C) are not illuminated because the connection to these LEDs has been deliberately broken. In subsequent iterations of the LED display

motif, complex patterns have been created by illuminating 1, 2, or 3 LEDs at a time using a pulse width modulation (PWM) scheme.

Programmable LED Display

We have created several P-o-P devices that demonstrate interfacing pen drawn circuits with existing hardware control systems. One such system that is very commonly used among engineers, hobbyists, and educators is the Arduino platform. The Arduino platform consists of a microcontroller board that is programmed with a high-level programming language.

An 8×8 LED display is shown in **Figure 4.13a**. The LED display is constructed in a similar manner as described above. However, rather than drawing additional conductive traces off of the ground and power grid lines to the surface mount LED, the LEDs are oriented at a 45° angle to directly contact the grid (**Figure 4.13b**). This orientation eliminates the need for drawing extra traces to accommodate different LED sizes (see schematic, **Figure 4.12a**). The LEDs are individually addressed during operation using the custom magnetic frame described in **Section 4.2.3**. To display a rectangular block of pixels (for example a 2×3 array or the entire 8×8 display), all LEDs in the pattern can be directly addressed at the same time. To display more complex patterns, such as a letter, pulse width modulation (PWM) is used. In this scheme, the character is broken into several blocks of pixels that can be expressed at the same time, and each segment is rapidly flashed on an off in sequence; to the human eye, it looks as though all LEDs in the pattern are turned on at the same time. PWM makes many complex patterns possible.

Capacitive Touch Pad

A capacitive touch pad, connected to the 8×8 LED display, is shown in **Figure 4.13a**. In this example, 5 conductive pads are used to track finger motion and activate nine different 2×2 regions of the display. The electrodes are arranged so that 9 individual areas are defined according to the color map shown in **Figure 4.13e**. When one or two of the electrodes are touched, the corresponding region of the LED display is activated (**Figure 4.13a**). The mechanism behind the capcitive touch sensor is shown in **Figure 4.13d**. Each discrete pad is connected to two pins on the Arduino called the send and receive pins that contain a 100

kΩ resistor between them. When a finger or another conductive object comes in close proximity to the sensor (nearly touching), the two surface act like parallel plates in a capacitor. The presence of this capacitive element changes the measured time constant of the circuit.[6] Using a 5-pad design and corresponding 5-magnet plug (**Figure 4.13c**), many touch pad designs are possible. Since the Arduino code can be written to distinguish between touching 0, 1, 2, 3, 4 or 5 pads at the same time, a 5-pad design can map to 32 individual outputs, as follows:

$$\sum_{i=1}^{5} \binom{5}{i} = 32 \tag{4.8}$$

The conductive ink printing and magnetic mount motif can be extended to other types of touchpad prototypes such as interdigitated sliders or interfaces with custom icons. A tutorial for the programmable display and touchpad are presented in **Appendix B**.

Three-Dimensional (3D) Antenna

A 3D antenna drawn on Xerox paper and wrapped around a glass hemisphere is shown in **Figure 4.14a**. The reflection coefficient of a 3D antenna is measured using a network analyzer. The reflected power quantifies how well energy is coupled from the transceiver to the antenna and vice-versa.[1], [8][7] The measured center frequency was 1.87 GHz with efficiency of 20-30% (**Figure 4.14b**). Although the reflected power of the paper antenna (-4.9 dB at 1.85 GHz) is low, we demonstrated that a functioning antenna can be made by this simple fabrication approach.

RC Filter

Passive components such as capacitors and resistors make up the majority of most printed circuit board assemblies (PCBAs). The ability to print these components directly onto a flexible substrate using functional inks would eliminate the need to surface mount many individual components and greatly simplify Pen-on-Paper printed circuit board assemblies (PCBAs). We first created capacitors, composed of silver ink patches separated by adhesive-backed paper, as shown in **Figure 4.15a**. The capacitance of square-shaped capacitors with

edge lengths of 0.5 to 1.5 cm ranges from 0.08 to 0.28 nF. The capacitance scales roughly linearly with edge length.

To fabricate a RC filter circuit we printed silver conductive lines and carbon resistive lines, and a paper capacitor, as shown in **Figure 4.16a**. The resistance of the combined silver and carbon lines is 1.23 MΩ and the silver/paper capacitor has a capacitance of 0.157 nF. The RC circuit serves as a low-pass or high-pass filter depending on the orientation of the input and output power lines. The diagram shown in **Figure 4.16b** specifies the electrode orientation for a low-pass (top) and a high-pass (bottom) filter.[15] The frequency response of the filter in low-pass and high-pass modes is shown in **Figure 4.16c-d**. The low-pass filter, in which the output wave is measured over the capacitor, attenuates the sine wave signal at high frequency (10 kHz shown). At high frequencies, the capacitor only has time to charge up partially before the input waveform switches its direction. The high pass filter, in which the output is measured over the resistor, behaves in the opposite manner. At high frequency, the capacitor acts like a break in the circuit, and current flows through the resistor.[15]

By plotting the output voltage of each filter is against different values of input frequency, we obtain a Frequency Response Curve or Bode plot. The Bode plots for both an ideal filter and the paper RC filter are shown in **Figure 4.17a**. The amplitude is expressed in decibels (dB) with relation to the maximum possible output voltage (Vin = 1000 mV).

$$amplitude[dB] = 20 \times log(\frac{V_{out}}{V_{in}}) \tag{4.9}$$

The cutoff frequency for ideal high pass or low pass filters are computed using the values of the resistor and capacitor in the circuit.[15]

$$f_c = \frac{1}{2\pi RC} \tag{4.10}$$

The cutoff frequency of the ideal filter is 824 Hz. In practice, the cutoff frequency occurs at the point where the output signal amplitude is attenuated to a value of $1/\sqrt{2}$ or ∼70.7% of the maximum attainable voltage. Since the low-pass and high-pass filters use the same resistor and capacitor, we can also estimate a cutoff frequency of ∼1500 Hz from the crossover point between the high pass and low pass Bode plots.[15]

There is a phase lag between the input and output waveform that ranges between 0° and 90°. In the low-pass filter, the output signal lags behind the input waveform. This corresponds to the time required to charge the capacitor plates. In the high-pass filter, the output wave leads ahead of the input, so it has a negative phase lag.[15] Both trends can be seen in the input and output waveforms presented in **Figure 4.16c-d** and in the plots shown in **Figure 4.17b**. The phase lag at the cutoff frequency should be equal to 45° or -45°. The equations governing the behavior of ideal filters are shown below (in the ideal filter, $f_c = 824$ Hz).

Low-pass filter

$$\varphi = -\arctan(2\pi f_c RC) \tag{4.11}$$

High-pass filter

$$\varphi = \arctan(\frac{1}{2\pi f_c RC}) \tag{4.12}$$

The phase lag of the paper RC filter are compared to those of the ideal filter in **Figure 4.17b**. In the ideal filter, a phase lag of 45° aligns perfectly with the cutoff frequency. However, the 45° phase lag occurs at a slightly higher frequency for the low-pass filter and at a slightly lower frequency for the high-pass filter. (**Figure 4.17b**)

Paperduino

An Arduino Pro Mini is printed by mounting our conductive rollerball pen in a desktop pen plotter, as shown in **Figure 4.18**. This fully functioning board is programmed to blink the on-board LED as well as turn on, blink, and fade an LED connected to two input/output pins. Our observations from the controlled printing experiments motivated many design

choices for the printed Arduino. For example, we adjusted the Arduino circuit schematic specifically to work with the Pen-on-Paper platform (**Figure 4.18a**). The components and traces are laid out in a single layer to enable printing in a single step. To achieve this, we frequently used the surface mount components as jumpers. In addition, the line width is set to 0.6 mm in the circuit schematic software (EAGLE CAD) to match the actual printed line width on photo paper. In the schematic design, three digital pins are cut off from the rest of the circuit. To make use of these pins in the future we could adhere a strip of adhesive backed paper as an insulating layer and draw connections to these pins.

The surface mount components are attached using two different techniques shown in **Figure 4.18d-e**. The first method relies on placing superglue in the gap between the component electrodes and reinforcing the connections with conductive epoxy. This method is permanent and the circuit is highly resistant to bending. The second method utilizes z-axis conductive tape to attach the components. Z-axis tape conducts electrical current through the thickness of the film via metallic micro-pillars, so it directly connects the components to the drawn pads without shorting the component electrodes. This approach is a cheaper and faster method of attachment, but does not form a permanent bond between the components and traces.[9]

The Paperduino is powered and programmed by placing on a steel surface and attaching custom cables with single magnets on the end. The board is programmed to flash an LED, which is attached to two of the analog output pins on a magnetic circuit board (**Figure 4.18c**). Future iterations of the printed Arduino will incorporate printed passive components such as resistors and capacitors instead of using corresponding SMD components. A tutorial for creating a Paperduino board is presented in **Appendix A**.

4.4 Conclusions

We have developed a new platform known as Pen-on-Paper electronics. Rollerball pen writing of conductive silver and resistive carbon inks offers an inexpensive and intuitive approach to creating programmable electronics on paper. We find that a balance between viscous and surface forces determines the shape of the meniscus as well as the corresponding

morphology of the printed line.[4, 13] Specifically, the threshold speed above which the meniscus shape changes corresponds to $Ca \sim 0.1$ to 0.4 depending on which ink viscosity (initial or partially dried) is used in this analysis. These values are lower than expected based on prior studies of lubricated ball bearings. This discrepancy likely arises from absorption and drying of the ink solvent during printing, which leads to a pronounced increase in local ink viscosity. Mechanical pen plotting can be implemented for the low-cost, large-area production of paper electronics devices; in this case, lower viscosity inks should be used due to their ability to form uniform lines at high printing rates. Finally, we demonstrated the facile construction of myriad P-o-P devices, including electronic art, antennas, printed circuit boards, and programmable displays.

4.5 Tables

Table 4.1: Conductive silver ink properties

Ink Composition (wt% Ag)	Density (g/ml)	Surface Tension (mN/m)
40	1.567	64
45	1.686	62
50	1.826	54
55	1.99	59

Table 4.2: Composition of conductive silver inks (See **Table 3.2** for more compositions). *Ink index # is the weight percentage of silver in the ink, as mixed. **The value in parentheses is the concentration of HEC in the viscous HEC-water carrier fluid in g/ml. ***Values below the second line correspond to inks partially dried on model photo paper.

Ink index # *wt% silver*	Silver conc. *vol% silver in ink*	HEC conc. *vol% HEC in ink*	Water conc. *vol% water in ink*
40*	6.0	1.4 (2.0)**	92.6
45	7.3	1.6 (2.4)	91.1
50	8.8	2.0 (3.0)	89.2
55	10.5	2.4 (3.6)	87.1
57***	11.3	2.5 (3.9)	86.1
62	13.6	3.1 (4.9)	83.3
66	15.8	3.6 (5.8)	80.6
70	18.5	4.2 (7.0)	77.3

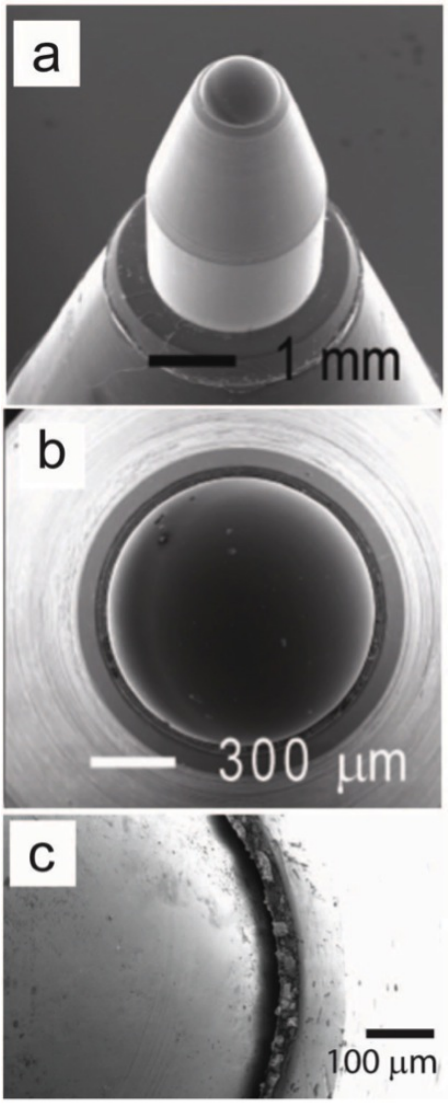

Figure 4.1: Rollerball pen geometry. (a-b) SEM micrographs of the pen tip. The ball diameter is approximately 960 μm. (c) Close-up view of the gap between the rollerball tip and housing. The gap spacing is approximately 30 μm.

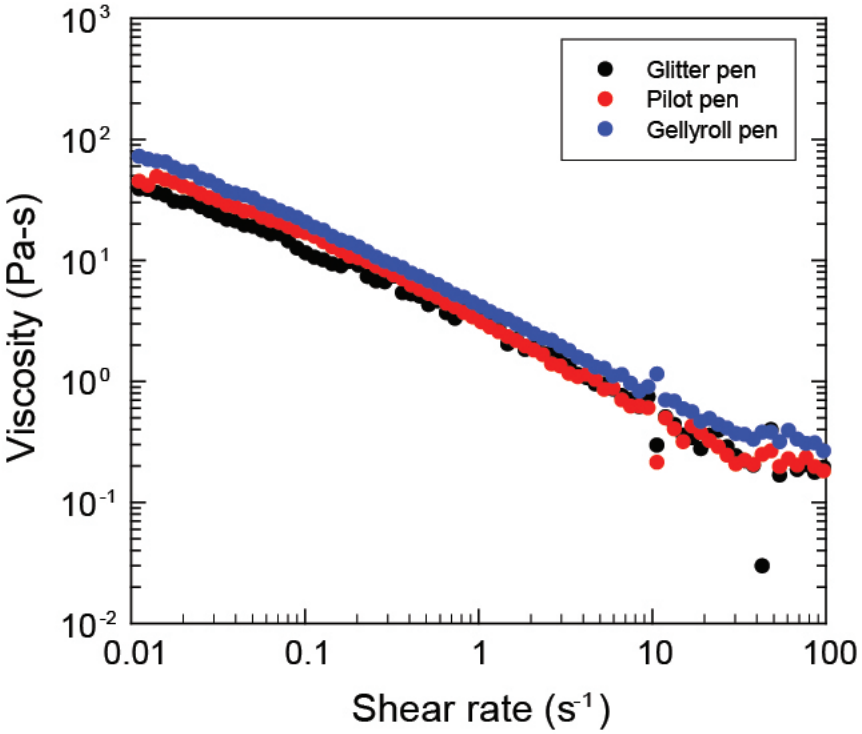

Figure 4.2: Commercial pen ink rheology. Apparent viscosity as a function of shear rate for inks housed three pen types: Glitter pen (960 μm diameter tip), Gelly Roll pen with solid colored ink (600 μm tip), and Pilot fine tipped pen (250 μm tip).

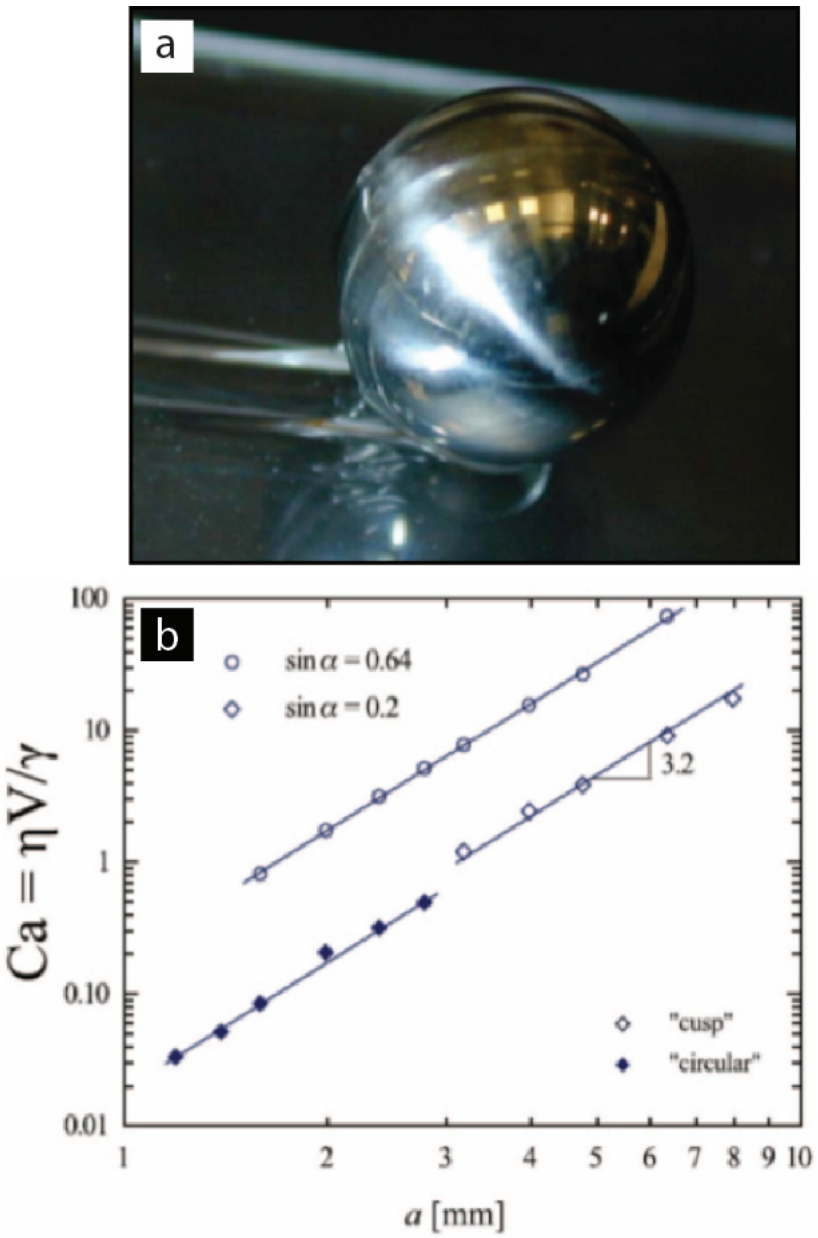

Figure 4.3: Printing instability in roller-based systems. (a) An optical image of a ball bearing rolling down a lubricated ramp. The meniscus breaks into two trails ("cusp") at high rolling speed. (d) A plot of capillary number v. ball radius for two different ramp angles.

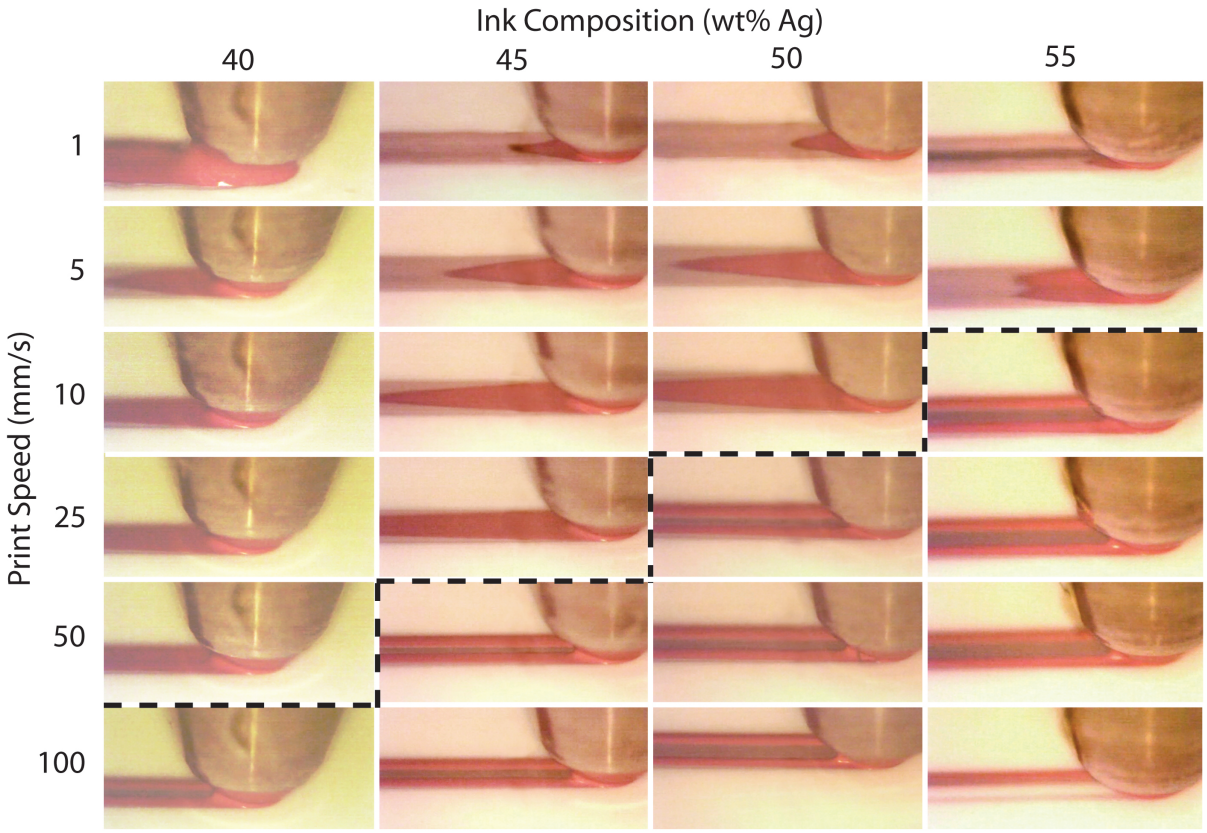

Figure 4.4: Conductive silver inks composed of 40, 45, 50, and 55 wt% silver are printed on model paper using a robotic stage at printing speeds of 1, 5, 10, 25, 50, and 100 mm/sec. The meniscus at the trailing edge of the ball tip undergoes a transformation in shape at a critical printing speed, denoted by the dotted black line.

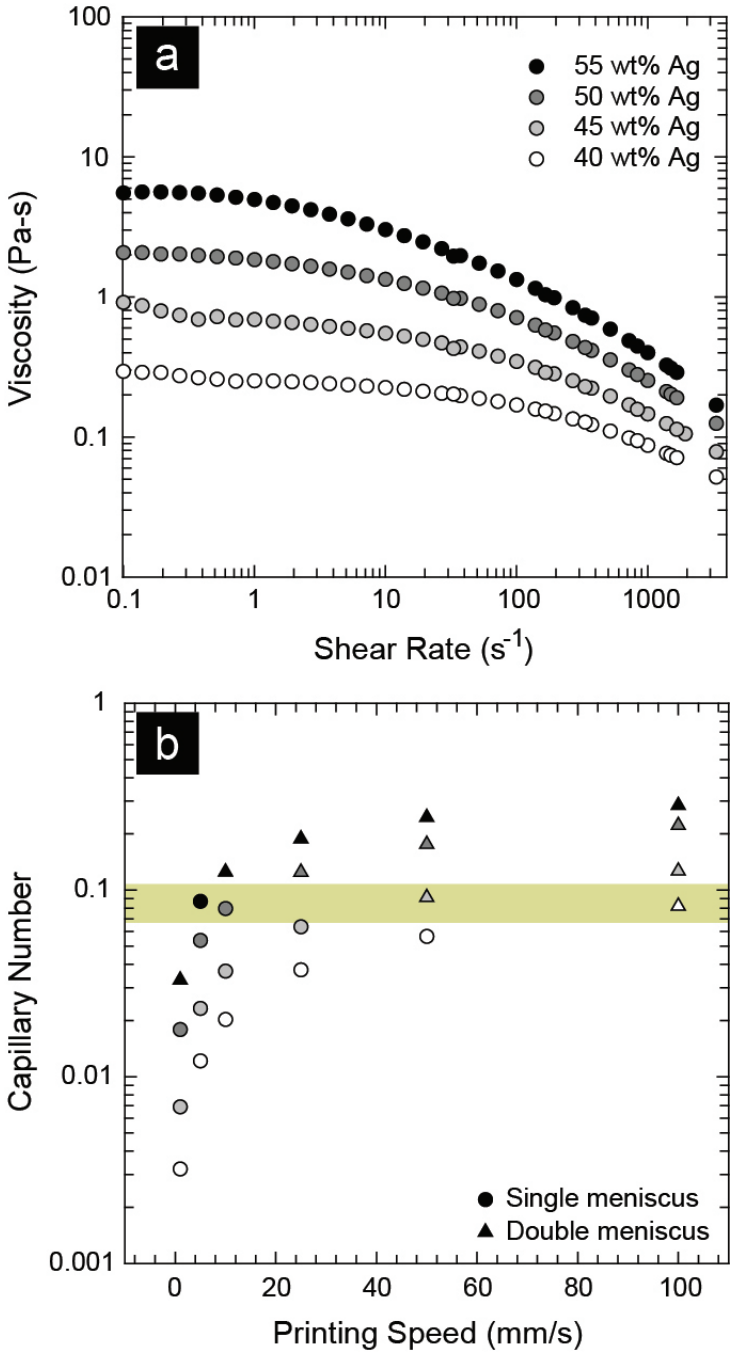

Figure 4.5: Silver inks printed on model Luster photo paper. (a) Apparent viscosity (η) of silver inks as a function of shear rate. (b) Capillary number of silver inks (Ca) as a function of printing speed. Transformation in meniscus shape occurs around $Ca = 0.1$ for each ink concentration.

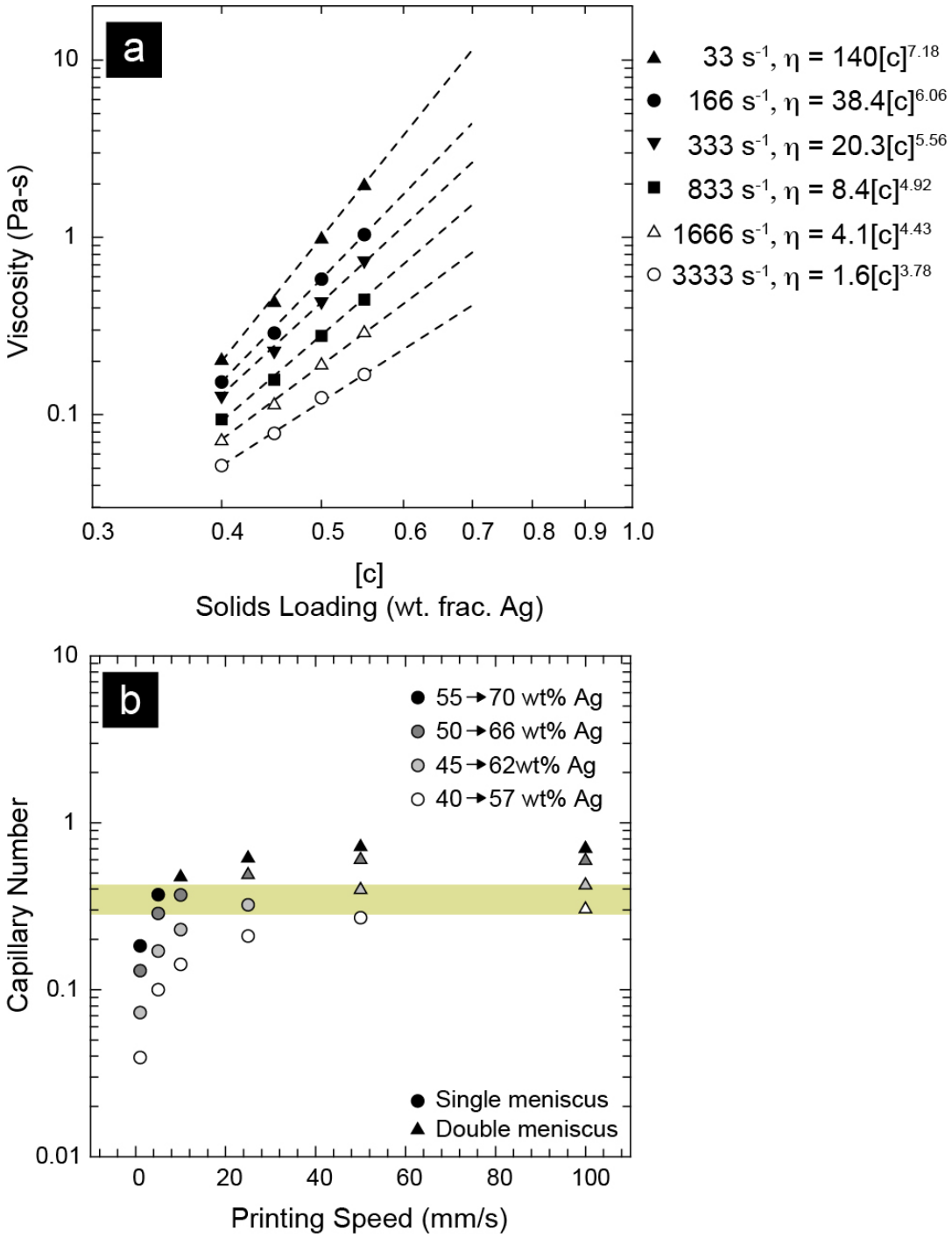

Figure 4.6: (a) Apparent viscosity as a function of ink solids loading (wt. fraction silver) for six shear rates relevant to pen printing. (b) Capillary number (Ca) of partially dried silver inks as a function of printing speed. Original and effective solids loading is shown in the legend.

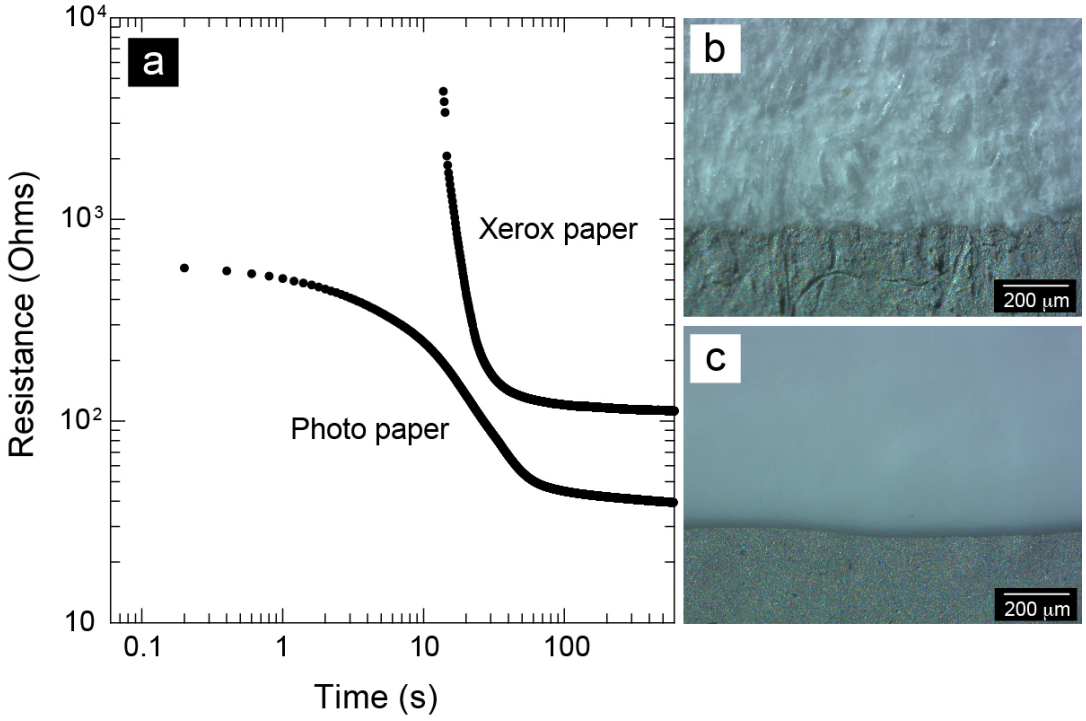

Figure 4.7: Conductive ink drying kinetics. (a) Resistance of 50 wt% silver ink lines (4 cm) drawn on Xerox copy and Luster photo paper as a function of drying time. *The ink printed on Xerox paper remains saturated with water for 10 seconds before a conductive particle mat forms. (b–c) High-magnification images of conductive ink printed on Xerox copy (b) and Luster photo paper (c).

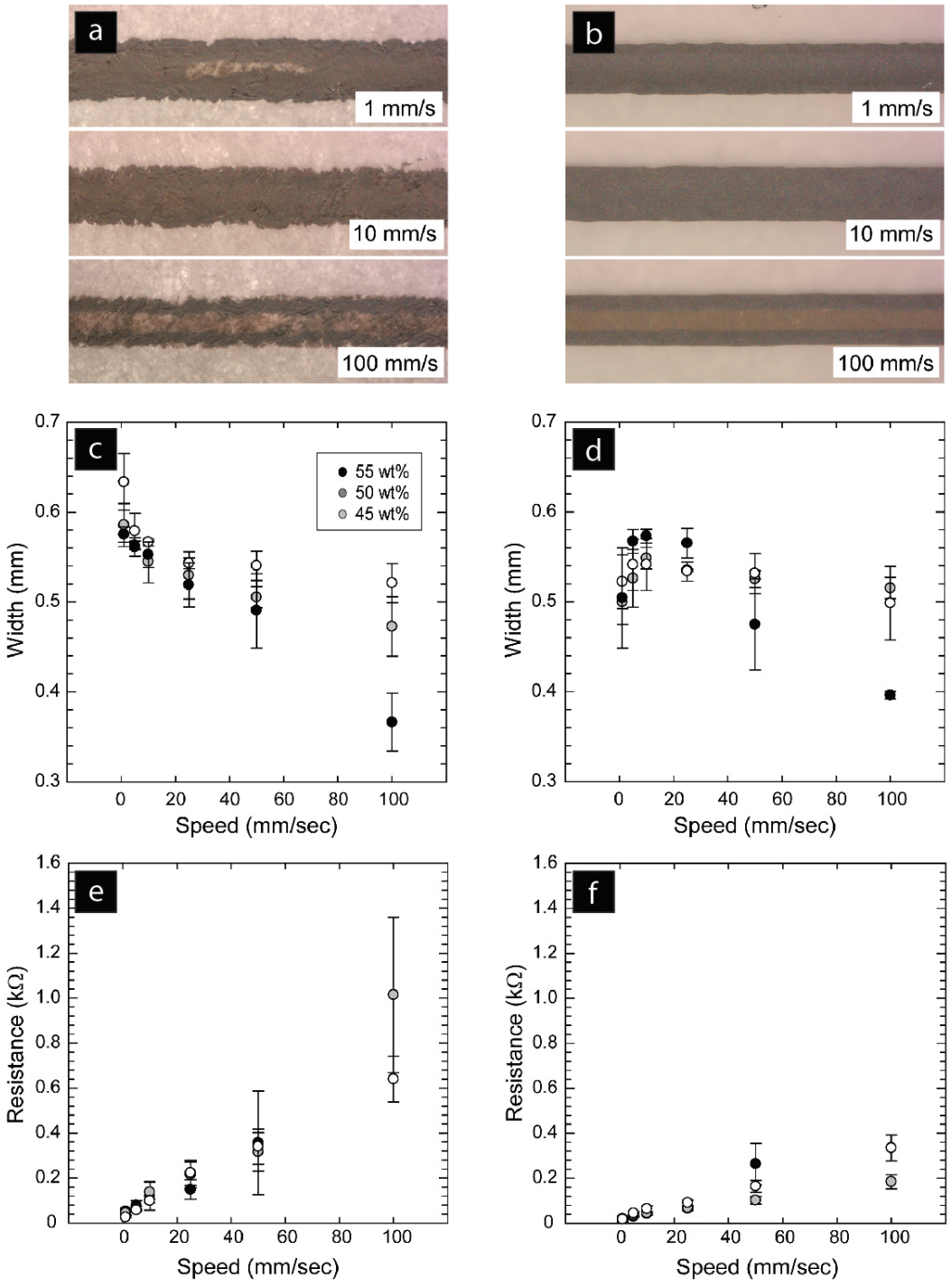

Figure 4.8: Silver ink with 50 wt% solids loading printed on (a) Xerox paper and (b) photo paper at three different printing speeds. (c–d) Width of printed lines as a function of printing speed on Xerox paper (c) and photo paper (d). (e) Resistance of a 5 cm long printed line as a function of printing speed on Xerox paper and (f) photo paper.

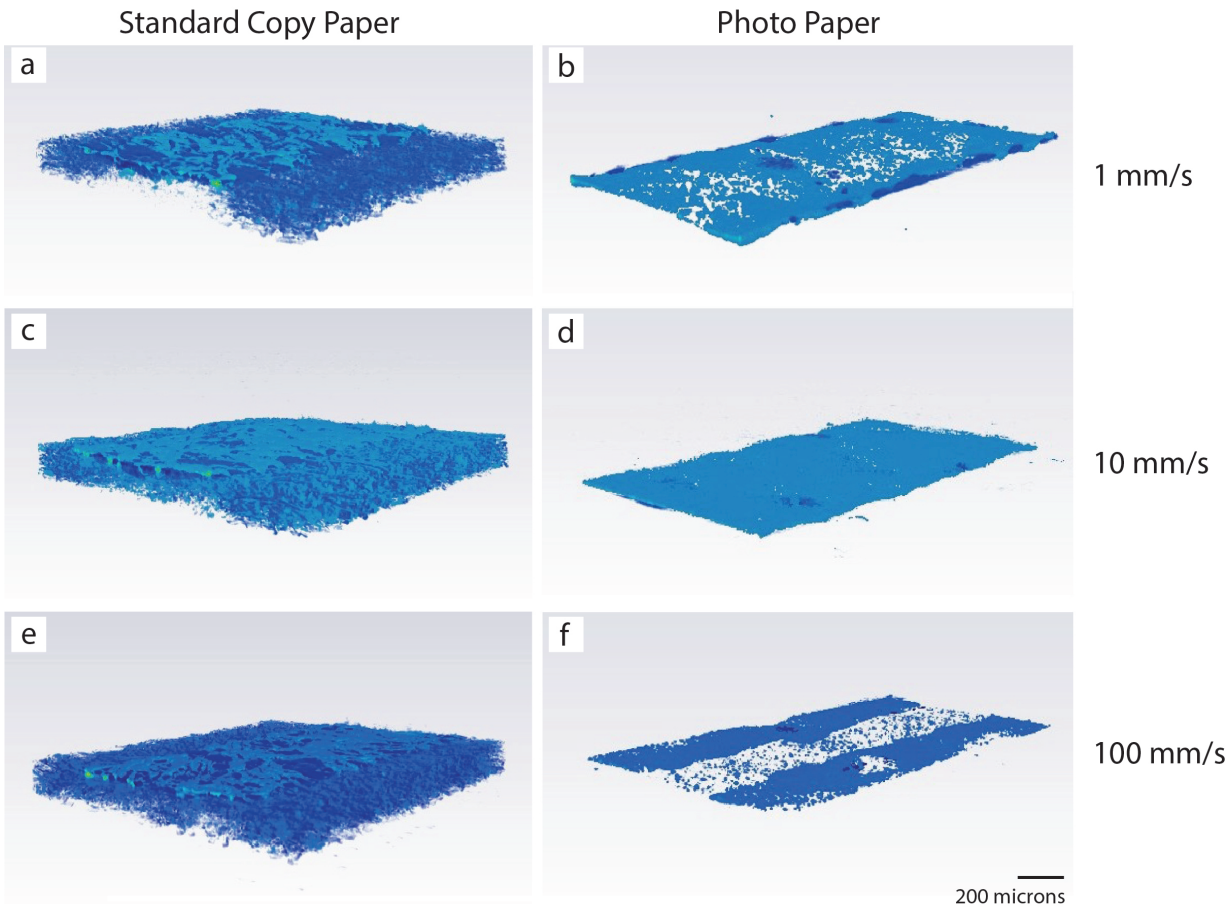

Figure 4.9: Micro-CT renderings of 50 wt% silver ink printed on Luster photo paper and standard copy (Xerox) paper at various printing speeds. (a–b) 1 mm/sec; (c–d) 10 mm/sec; (e–f) 100 mm/sec.

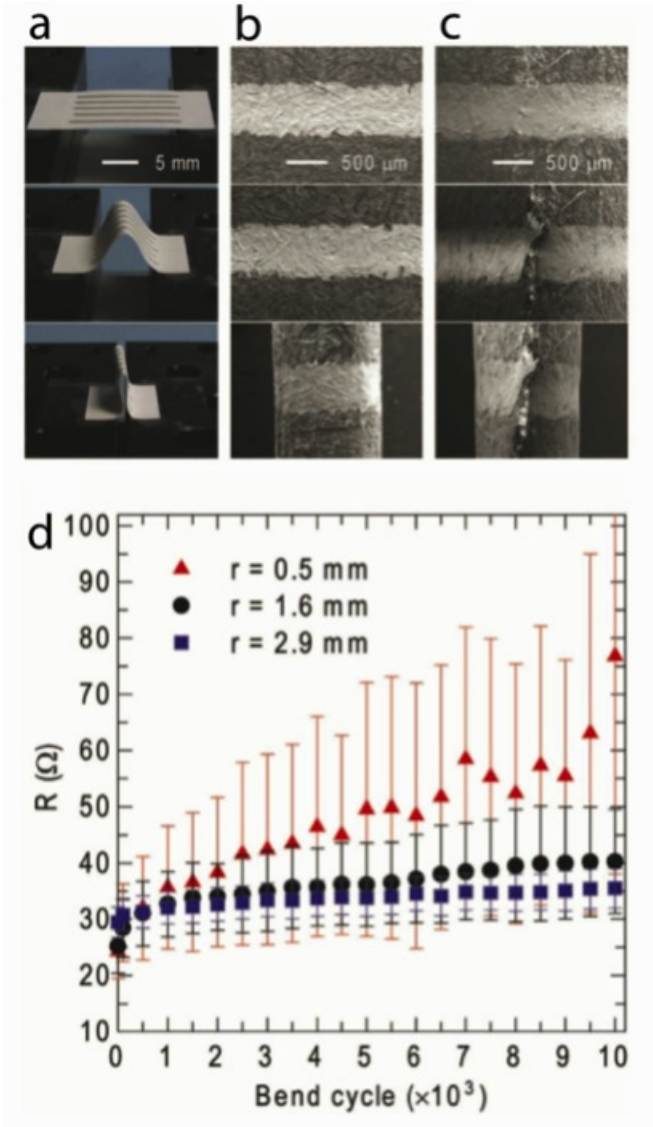

Figure 4.10: Bending behavior of printed electrodes. (a) Optical images of silver electrode arrays in flat (top) and bent states with bend radii of 1.6 mm (middle), 0.5 mm (bottom). (b) SEM micrographs of the silver electrodes in flat and bent states during the first bend cycle. (c) SEM micrographs of the silver electrodes in flat and bent states after 10,000 bend cycles. (d) Electrical resistance as a function of bend cycle of the printed silver electrodes of varying bend radius. Measurements are taken while paper is in flat orientation.

Figure 4.11: Artistic drawing with P-o-P platform. (a) Optical image of conductive electronic art drawn by a silver-ink filled rollerball pen on Xerox paper. (b) SEM image at the root of the a tree, showing a conductive silver network. (c) SEM image of the LED chip, adhered to the paper substrate with the conductive silver interconnects.

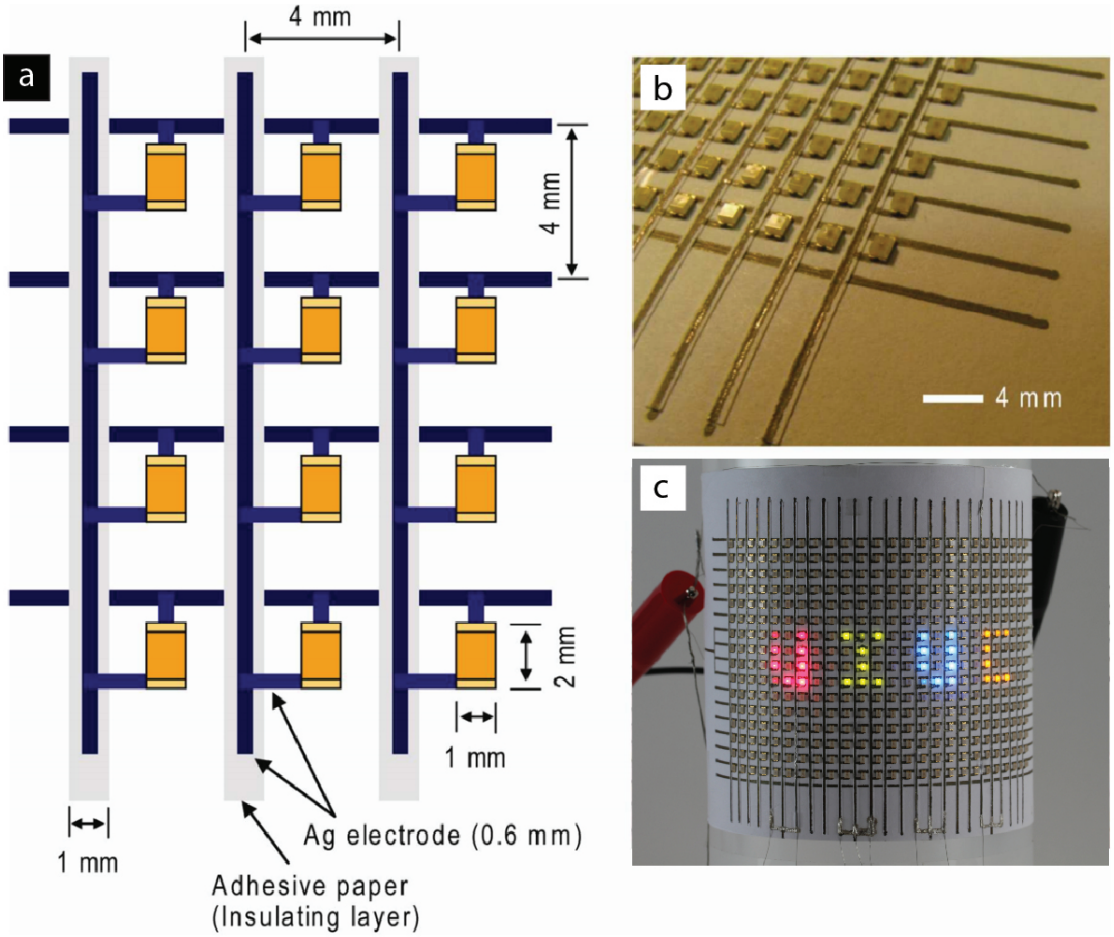

Figure 4.12: (a) Schematic of a pen-on-paper LED display. A two-layer device is produced by using strips of adhesive-backed paper as an insulating layer. (b–c) Optical images of the LED array construction and illuminated text.

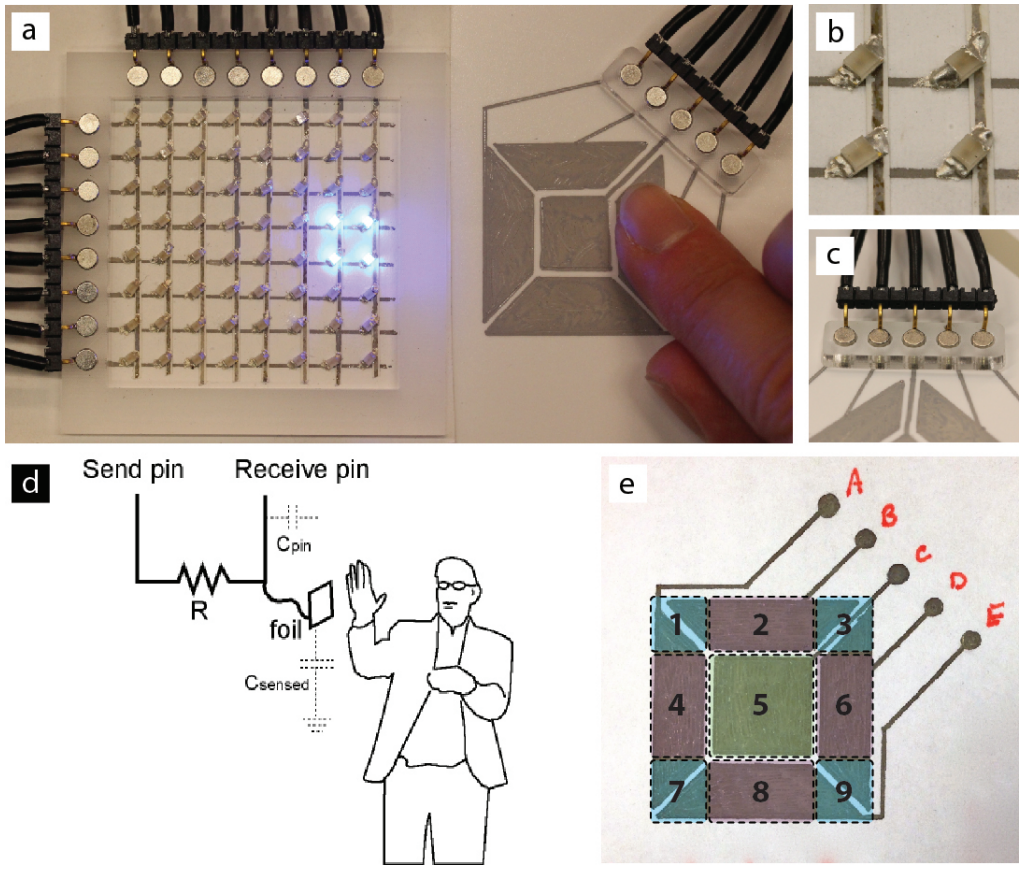

Figure 4.13: Display and Touchpad. (a) Individually addressable 8x8 LED display controlled by a capacitive touch pad. (b) Magnified view of 4 surface mount LEDs connected to printed traces by conductive epoxy. (c) Magnetic connector is composed of laser cut acrylic, 1/8 neodymium magnets and pin headers. (d) Schematic of a capacitive touch sensor including a send and receive pin separated by a resistor of value ~10,000 kΩ. (e) Pen-drawn touchpad containing five electrodes and nine distinct sensitive regions.

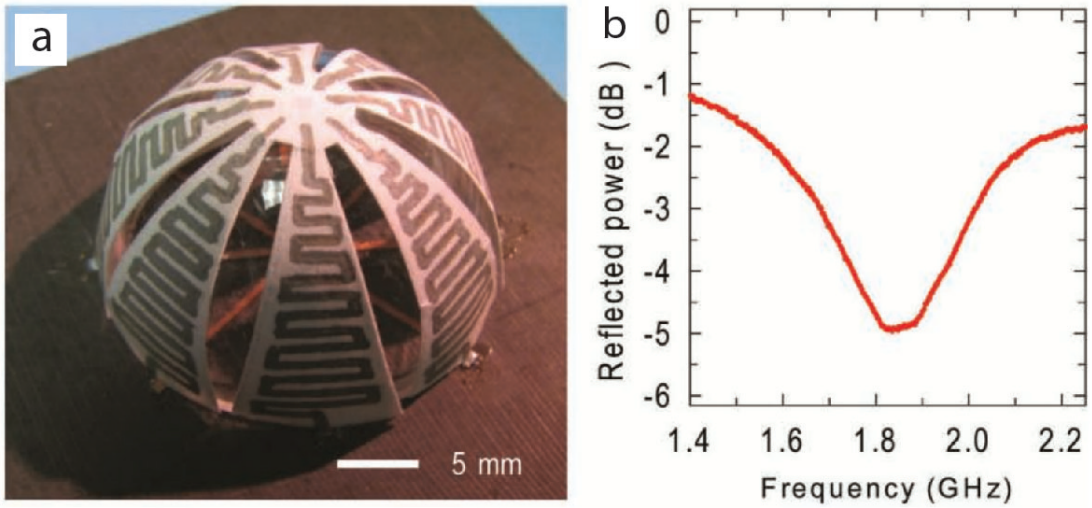

Figure 4.14: Three dimensional RF antenna. (a) Optical image of the 3D antenna, fabricated by drawing periodic conductive silver tracks on adhesive-backed paper, followed by conformally adhering it to a hemispherical hollow glass substrate. (b) Reflected power of the 3D antenna as a function of frequency.

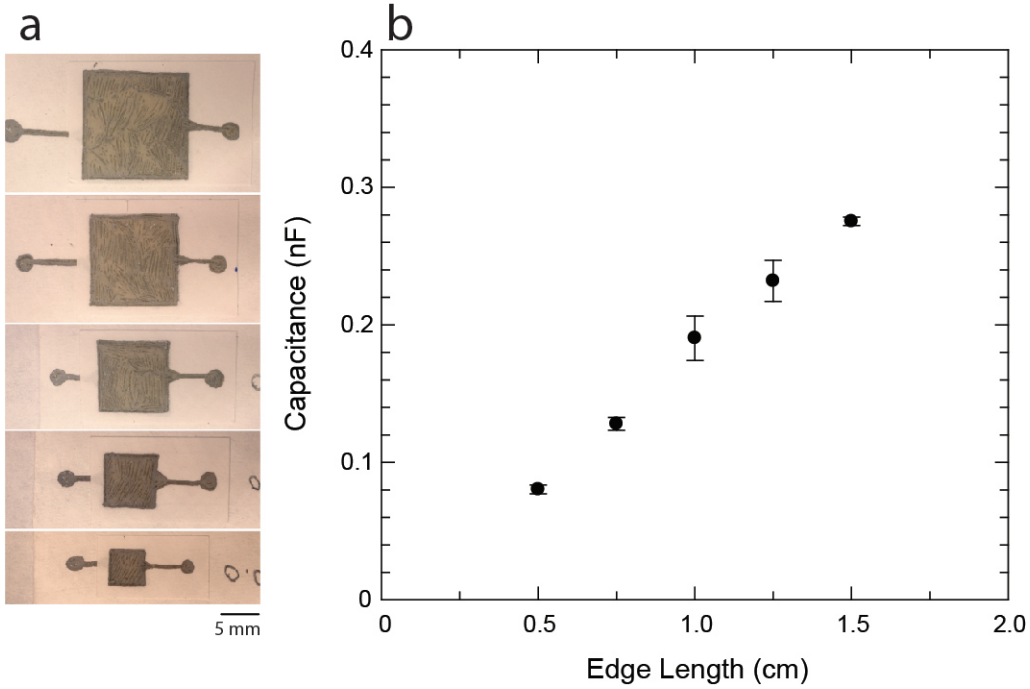

Figure 4.15: (a) Paper capacitors are constructed from patches of silver ink, laminated with adhesive backed paper. (b) Capacitance is a function of the capacitor edge length.

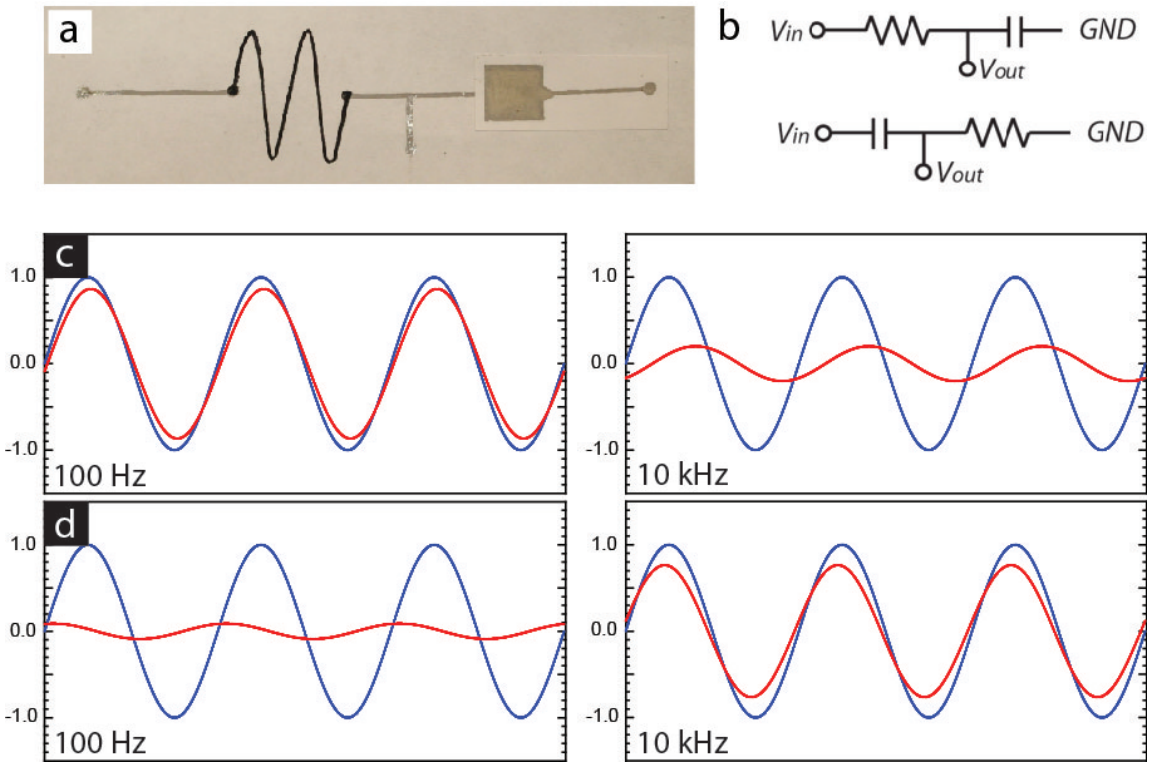

Figure 4.16: Low pass and high pass filters. (a) Pen-drawn RC filter containing a 1.23 MΩ carbon resistor and a 1.57 nF paper capacitor. (b) Circuit schematics for the RC device operated as a low-pass (top) or a high-pass (bottom) filter. (c) Frequency response of the low-pass filter (input = blue and output = red). (d) Frequency response of the high pass filter.

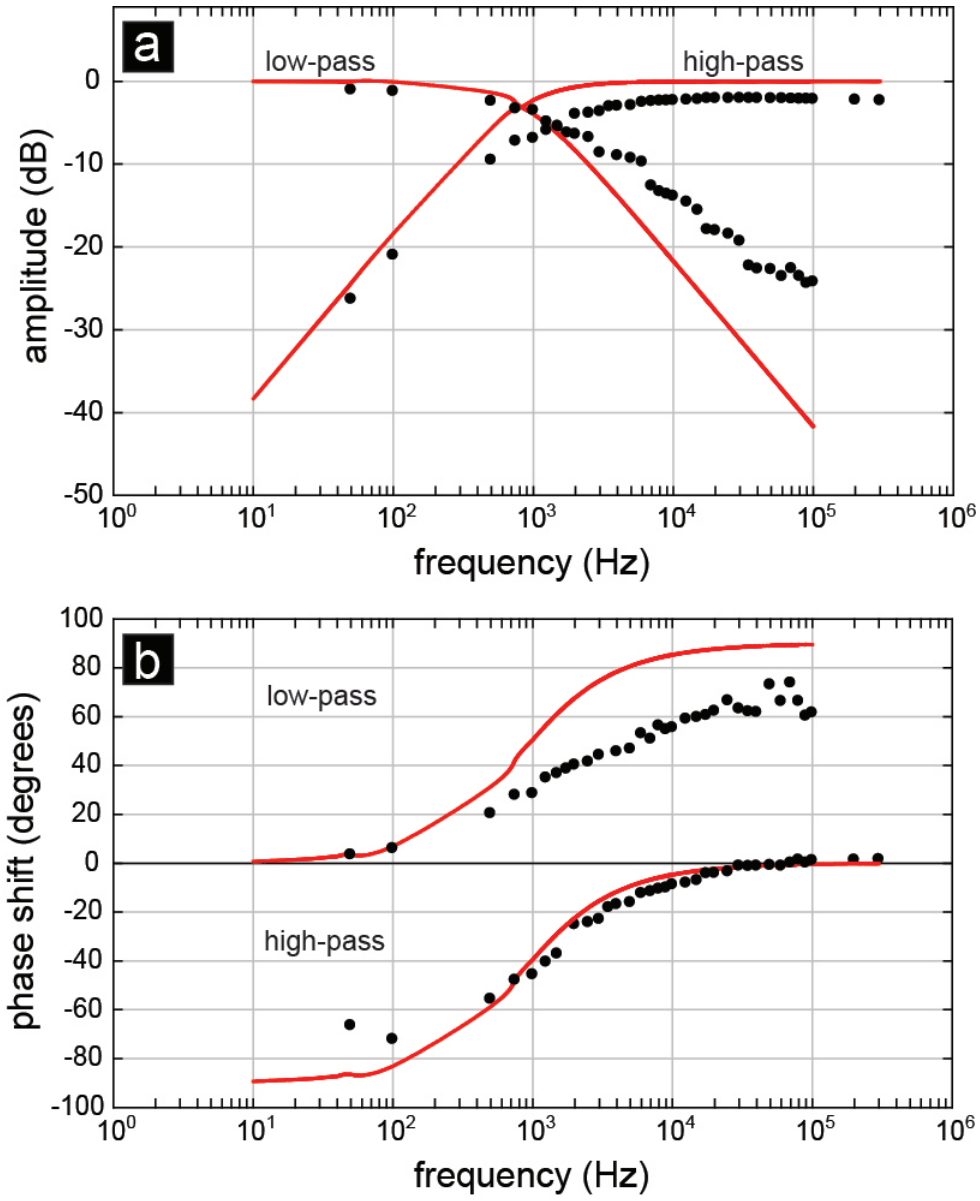

Figure 4.17: RC Filter. a) Bode plot of the high and low pass paper filters and amplitude predictions of ideal filters. b) Phase lag of the high and low pass filters as a function of input wave frequency and predictions of ideal filters. [15]

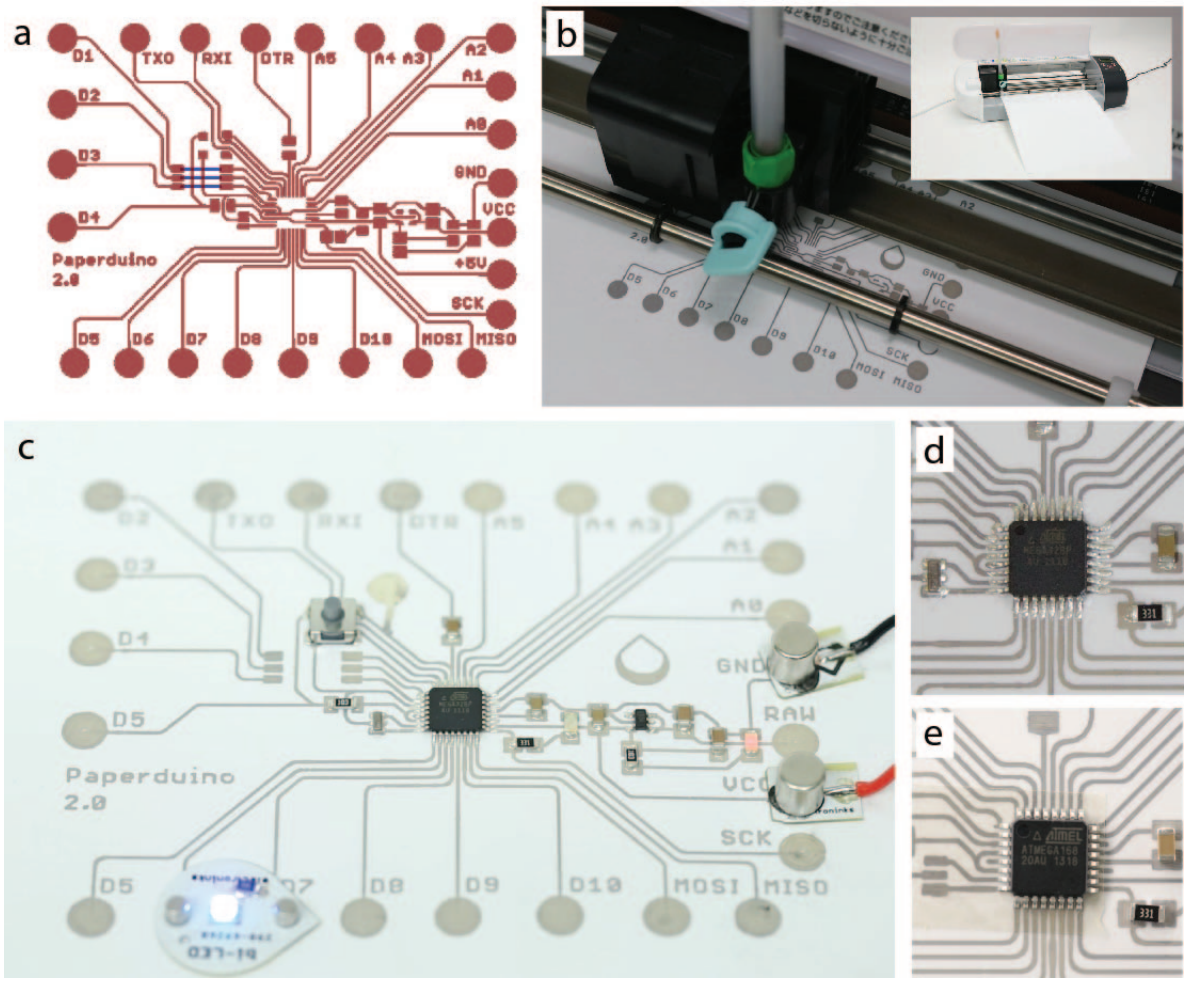

Figure 4.18: Printed Arduino Pro Mini. (a) Circuit schematic for an Arduino Pro Mini board, adapted for printing on paper. (b) Silver ink–filled rollerball pen mounted in a pen plotter, inset: the low–cost plotter with pen and paper mounted. (c) Fully functioning Arduino board. (d) An integrated circuit (IC) chip, capacitor, resistor, and resonator are attached to the pen traces using conductive epoxy. (e) An IC, capacitor, and resistor are attached to the circuit using z–axis conductive tape.

4.7 References

[1] Analisa Russo, Bok Yeop Ahn, Jacob J. Adams, Eric B. Duoss, Jennifer T. Bernhard, and Jennifer A. Lewis. Pen-on-paper flexible electronics. *Advanced Materials*, 23(30):3426–3430, August 2011.

[2] L.H. Pan and J.R. Debruyn. Broken-parity waves at a driven fluid-air interface. *Physical Review Letters*, 70(12):1791–1794, March 1993.

[3] R. L. Santos, U. Agero, and J. M. A. Figueiredo. Pattern dynamics in a perturbed printer's instability experiment. *Physical Review. E, Statistical, Nonlinear, and Soft Matter Physics*, 77(6 Pt 2):066310, June 2008.

[4] E. Pitts and J. Greiller. The flow of thin liquid films between rollers. *Journal of Fluid Mechanics*, 11(01):33–50, 1961.

[5] Leah Buechley, S. Hendrix, and M. Eisenberg. *3rd International Conference on Tangible and Embedded Interaction*, 2009.

[6] Paul Badger. Capacitive sensing library.

[7] Jacob J. Adams, Eric B. Duoss, Thomas F. Malkowski, Michael J. Motala, Bok Yeop Ahn, Ralph G. Nuzzo, Jennifer T. Bernhard, and Jennifer A. Lewis. Conformal printing of electrically small antennas on three-dimensional surfaces. *Advanced Materials*, 23(11):1335–1340, March 2011.

[8] Arduino pro mini, 2014.

[9] Yoshihiro Kawahara, Steve Hodges, Benjamin S. Cook, Cheng Zhang, and Gregory D. Abowd. Instant inkjet circuits: Lab-based inkjet printing to support rapid prototyping of UbiComp devices. In *Proceedings of the 2013 ACM International Joint Conference*

on Pervasive and Ubiquitous Computing, UbiComp '13, pages 363–372, New York, NY, USA, 2013. ACM.

[10] Henry Gostony and Stuart L. Schneider. *The Incredible Ball Point Pen: A Comprehensive History & Price Guide*. Schiffer Pub Ltd, Atglen, PA, January 1998.

[11] CELLOSIZE hydroxyethyl cellulose. Technical data sheet, DOW Chemical.

[12] J. R. A. Pearson. The instability of uniform viscous flow under rollers and spreaders. *Journal of Fluid Mechanics*, 7(04):481–500, 1960.

[13] J. Bico, J. Ashmore-Chakrabarty, G. H. McKinley, and H. A. Stone. Rolling stones: The motion of a sphere down an inclined plane coated with a thin liquid film. *Physics of Fluids (1994-present)*, 21(8):082103, August 2009.

[14] Adam C. Siegel, Scott T. Phillips, Benjamin J. Wiley, and George M. Whitesides. Thin, lightweight, foldable thermochromic displays on paper. *Lab on a Chip*, 9(19):2775–2781, October 2009.

[15] M. J. Roberts. *Fundamentals of Signals and Systems*. McGraw-Hill Science/Engineering/Math, Boston, 1 edition edition, February 2007.

CHAPTER 5

DIRECT WRITING OF SILVER NANOPARTICLE INKS FOR FLEXIBLE PHOTOVOLTAIC METALIZATION

5.1 Introduction

Photovoltaic (PV) devices typically consist of silicon wafers that are flat, rigid, and brittle. Recently, new PV architectures have emerged in the form of lightweight, flexible, and portable devices.[1] Rogers, Nuzzo and coworkers pioneered the development such devices consisting of a sparse array of microcells (1–5 mm length) on a flexible substrate. These PV devices are highly flexible although the active material is rigid.[2] Illustrative examples of these two motifs are shown in **Figure 5.1**. In addition to enabling flexibility, a discrete cell architecture minimizes the amount of costly active material that is used. Although the area coverage of PV material is greatly reduced in a sparse array format, the device can be married with a solar concentrator to significantly increase its efficiency.[2–4]

We have developed a new method for patterning interconnects on flexible PV devices that employs many efficiency enhancing mechanisms in a single package (schematic, **Figure 5.2**)[1]. The first mechanism is adding a luminescent solar concentrator (LSC) that focuses a narrow range of wavelengths on the PV cells. The concentrator is composed of a film containing dye or quantum dots. The film absorbs a broad spectrum of light but emits light at long wavelengths close to the band gap of the PV cell. The dye is embedded in a high refractive index polymer which total internal reflection guides light to the PV cell.[3–12] In the second mechanism, two microcell/LSC layers are laminated together to broaden the spectrum of light that is converted.[13] One layer of microcells absorbs light at 850 nm wavelength, and the other absorbs at 630 nm. Finally, a micro-textured antireflective "moth-eye" coating is added to minimize losses due to light reflection from the top surface of the device.[14–19]

[1]This work was carried out in collaboration with Semprius and SAIC.

The new flexible PV array motif poses several challenges to wiring the individual cells. In each layer of the solar panel, the microcells are connected in series via narrow interconnects (<50 μm), and columns of interconnected PV cells are connected in parallel with wide bus bars (∼1 mm). The short interconnects between microcells are narrow to minimize the area coverage to the LSC, while the relatively long bus bars remain wide to act as current collectors for the device as a whole. The traditional methods of patterning silver interconnects and bus bars on Si wafers, such as screen printing, lack the precision required for patterning interconnects on sparse PV arrays. Most ink patterning techniques require a constant offset height between the printhead and substrate to ensure a uniform electrode line width. The flexible substrate in this study is warped and the discrete PV cells (∼5 μm height) of the PV cells introduce discrete vertical steps across the device. For example, screen printing requires a globally flat substrates, while inkjet printing does not provide conformal coverage over discrete steps in a PV array due to the wetting and spreading of the ink.[20] Here we explore the use of direct ink writing (DIW) as a low-cost approach to metallizing this new class of flexible PV devices. We demonstrate a strategy for printing over rough and contoured substrates as well as provide assessment of print quality and PV device performance.

5.2 Experimental Methods

5.2.1 Materials

The silver conductive ink used to wire flexible PV arrays is from the same family of conductive inks presented in **Chapter 3**. The solids loading of the silver ink is 60 wt% silver, which falls within the DIW printing regime (**Figure 3.1**).

PV arrays, provided by Semprius, are composed of polyimide films populated with a 10x8 grid of InGaP micro solar cells. Each microcell is a 1×5 mm rectangle with a 5 μm thickness. The populated polyimide film is mounted on a rigid glass carrier wafer using PDMS as a dry adhesive (schematic, **Figure 5.2**) and the total area of the film is 10×10 cm.

5.2.2 Optical Profilometry

To maintain a constant offset height between the ink deposition nozzle and substrate, the topography of the populated polyimide film is mapped using a chromatic confocal profilometer (Nanovea) prior to printing. This non-contact profilometer, or optical pen, is mounted on the same 3-axis positioning stage (Aerotech) used for DIW. Height measurements are taken at 500 μm intervals as the profilometer is rastered across the substrate. The rastering speed is 1 mm/sec and motion is paused for 0.25 seconds prior to each measurement to reduce the effect of stage vibration on the measured values. To reduce the total scan time, rapid continuous motion (10 mm/sec) is used in areas where no printing will occur and, thus, surface topography data is not needed. These areas are registered with an arbitrary value of "5000 μm" in the data set. After scanning each horizontal line, the individual data points populate a data matrix, which is then used as a calibration file that dynamically adjusts the height of the nozzle during printing.

5.2.3 Direct Ink Writing

The PV cells are connected in series by printing 50 μm wide silver interconnects. The silver ink is extruded through a 30 μm glass tapered nozzle using air pressure. The filament wets and spreads slightly on the substrate to conform to the raised PV cell contacts. The columns of PV cell array are connected in parallel by 1 mm wide bus bars. The bus bars are printed using a 610 μm diameter nozzle. Flat and wide ribbon-like traces are created by positioning the deposition nozzle 10 μm above the substrate. The low offset height defines the trace thickness and causes the ink to spread to the outer diameter of the nozzle, which is approximately 1 mm wide.

A gcode generator was written to produce interconnect patterns for multiple versions of the PV cell layout. The Visual Basic editor has inputs for array size, cell spacing, and pitch of the interconnect lines. The wired PV array layout is shown in **Figure 5.3**. Although there are dips and bumps in the substrate, the electrode pattern is programmed as though the substrate is perfectly flat. As the nozzle translates across the substrate surface, the nozzle moves up and down in accordance with the measured surface topography to deposit ink conformally over the rough substrate.

5.2.4 Annealing of Printed Features

The wired microcell array is annealed on an aluminum hotplate (Torrey Pines) at 175°C for 30 minutes. Annealing the printed traces on a hot plate does no visible or electrical damage to the traces or PV array. Although the polyimide substrate, PV microcells, and glass carrier wafer can withstand higher annealing temperatures, the limiting factor in the system is the adhesive used to attach the PV cells to the substrate.

5.2.5 Lamination of Integrated Devices

In the full production of the integrated PV array and LSC device, a series of spin coating, lamination, and embossing steps occur. To mimic this process, we spin coat a thin layer of polydimethylsiloxane (PDMS, Sylgard 184) on the surface of the interconnected array and allow it to cure at 80°C for 6 h. With this protective layer, we can gently peel the wired PV array off of its glass carrier wafer with silver traces intact. A fully wired, un-mounted PV array is shown in **Fiugre 5.4**.

5.3 Results and Discussion

5.3.1 Quantifying Substrate Topography

The tilt and bow of the substrate as well as bubbles in PDMS coating account for large height variations across the substrate. Typically, there is a 150 μm height difference between the

lowest and highest points across the substrate and bubbles or defects in the polyimide are ∼8 μm high, as shown in **Fiugre 5.5**. For our printing protocol, the surface roughness is large compared to the smallest nozzle size used (30 μm). To maintain a 10–15 μm offset height between the printing nozzle and substrate, a height calibration file obtained from profilometry is preprogrammed into the toolpath.

The profilometer or "optical pen" uses a white light source to probe the distance between the pen and the substrate. The pen contains a series of lenses that spatially separates the light spectrum so that narrow wavelength bands have a unique focal point. The wavelength that corresponds with the substrate surface reflects back to the pen sensor with highest intensity; this distance is recorded **Figure 5.6**. When working with laminated transparent materials, such as our polyimide film and carrier wafer, the profilometer can incorrectly identify another surface in the laminate as the top surface. For this reason, we used the profilometer in a non-standard mode. The confocal "thickness" mode measures both the bottom and the top surface; these surfaces reflect light with greatest and second greatest intensity. The output data stream contains five values that we can analyze (two surface heights, two intensities, and a thickness calculation). For every set of data points collected, we select the value that is the closest distance to the optical pen (i.e., the top surface of the substrate). The gcode that is used to scan the substrate and select the proper data stream is presented in **Appendix B**.

Another challenge in mapping the substrate optically is that the PV microcells themselves are very good absorbers. Often the optical pen cannot collect a reflection from the surface of the PV cell; in this case, a value of 0 is inputted into the calibration matrix. Data for the PV microcell region is extrapolated by averaging measurements 1 mm to the left and right of the microcell and adding 5 μm to compensate for the cell thickness. A topography map of both a region with missing cells and with cells added back in is shown in **Figure 5.7**.

Finally, the scan time is drastically reduced by selectively scanning the substrate where ink will be printed and actuating the optical pen very quickly over the areas that will remain blank. The two areas that can be scanned are shown in **Figure 5.8**. By reducing the total scan area from 10,000 mm^2 to 4000 mm^2 the scan time is significantly decreased from 16 hours to 6 hours.

5.3.2 Substrate Metalization

A fully connected electrode pattern along with representative examples of interconnect and bus bar printing are shown in **Figure 5.9**. The narrow interconnect printing is performed using a 30 μm tapered glass nozzle (**Figure 5.9b**). The offset height between the substrate and glass nozzle is set at 15 μm. If the nozzle is too high, the ink meniscus that forms at the nozzle tip does not make contact with the substrate; this results in a skipping or dotted line. If the nozzle height is too low, it can make contact with the surface and can break. The optical profilometer scan, described in **Section 4.2.1**, successfully maintains the nozzle height required over the entire substrate area (10×10 cm^2) During printing, the ink wets the substrate and spreads to a width of 50 μm and a thickness of 5 μm. An interconnect traces conformally printed onto the PV cell electrodes is shown in **Figure 5.10a**. A cross-section of a representative printed trace is shown in **Figure 5.10b**.

The wide bus bars are printed using a cylindrical metal nozzle of diameter 610 μm (**Figure 5.9c**). The offset height between the metal nozzle and polyimide substrate is also set at 15 μm; the large nozzle used to pattern bus bars does not print over the PV cells. Shallow printing with a wide nozzle results in a thin ribbon-like trace. Since the wetting angle between the silver ink and polyimide substrate is close to 90°, the ink is confined by the outer edge of the nozzle. As such, the width of the printed traces ($\sim$1 mm) corresponds roughly to the outer diameter of the nozzle (910 μm). Representative bus bars using four different sized nozzle (100, 200, 330, 610 μm) are shown in **Figure 5.11**.

5.3.3 Wired PV Devices

A single solar cell was tested in the dark in a forward bias condition. Under forward bias, a voltage is applied to the solar cell so that the native electric field within the P-N junction of the solar cell decreases. This removes the barrier to current flow that normally exists in the P-N junction and diffusion current can be measured across the solar cell. The maximum diffusion reached, the dark saturation current, is a measure of how well charge recombination occurs in the depletion region.[2]

[2]Forward bias measurement performed by Semprius.

We use the forward bias measurement to compare our printed silver ink interconnects to sputter-coated gold interconnects. A single PV microcell test strip is shown in **Figure 5.12a**. Before the printed silver ink is annealed, the cell does not reach its saturation current. After annealing interconnects at 175°C for 30 min, the microcell performs as well as a microcell connected by gold electrodes. A plot of bias voltage as a function of diffusion current for three interconnect types is shown in **Figure 5.12b**. The excellent conductivity (2×10^{-5} Ω-cm) achieved upon annealing at modest temperatures is central to achieving the desired device performance.

5.4 Conclusions

Direct writing of concentrated silver nanoparticle inks enables creation of complex interconnects and bus bars across sparsely populated arrays of PV microcells on polyimide. By predefining the substrate topography using optical profilometry, we have successfully demonstrated conformal printing of silver electrodes on substrates with highly non-uniform topography and optical properties. By implementing a more concentrated version of the highly conductive silver ink developed for Pen-on-Paper Electronics **(Chapter 4)**, we have demonstrated for the first time, a low-cost patterning route for metallizing 3D printed flexible photovoltaic devices.

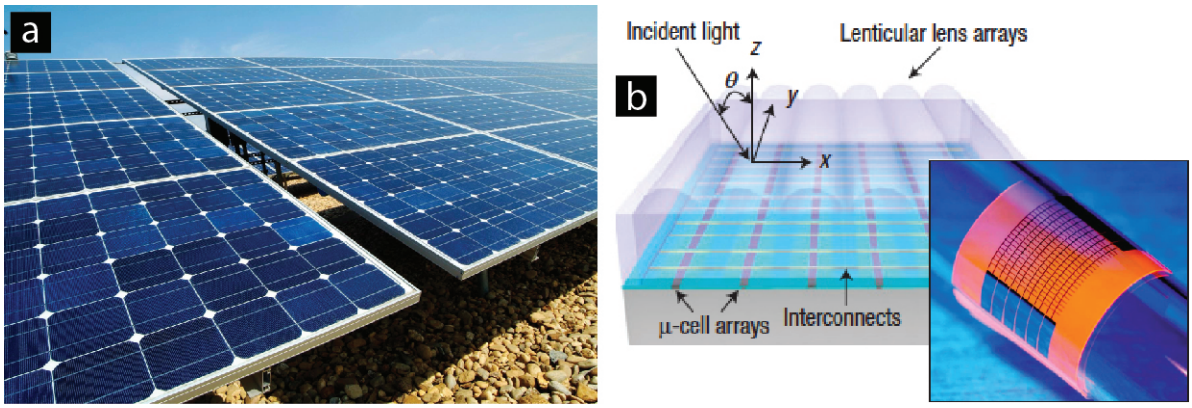

Figure 5.1: Examples of solar cell architectures. (a) Rigid solar cell panel and (b) a flexible PV array with a light-concentrating lenticular array.[2]

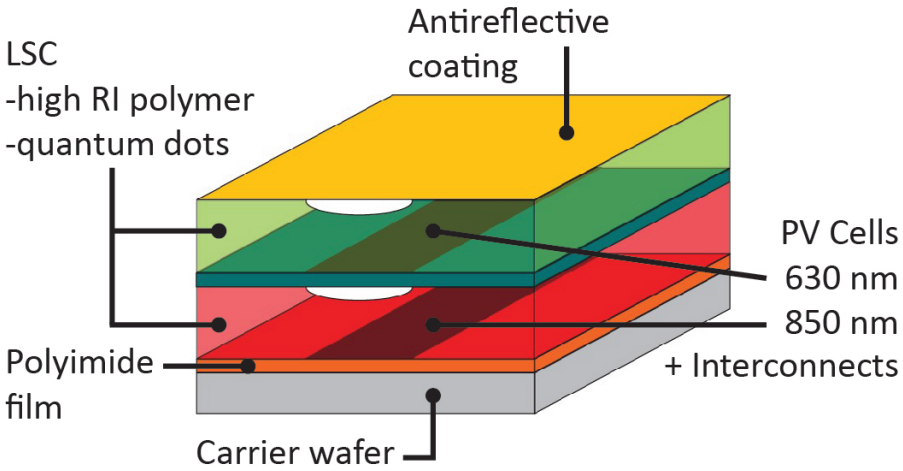

Figure 5.2: Multilayer solar cell array, containing two layers of solar cells and luminescent solar concentrators (LSCs).

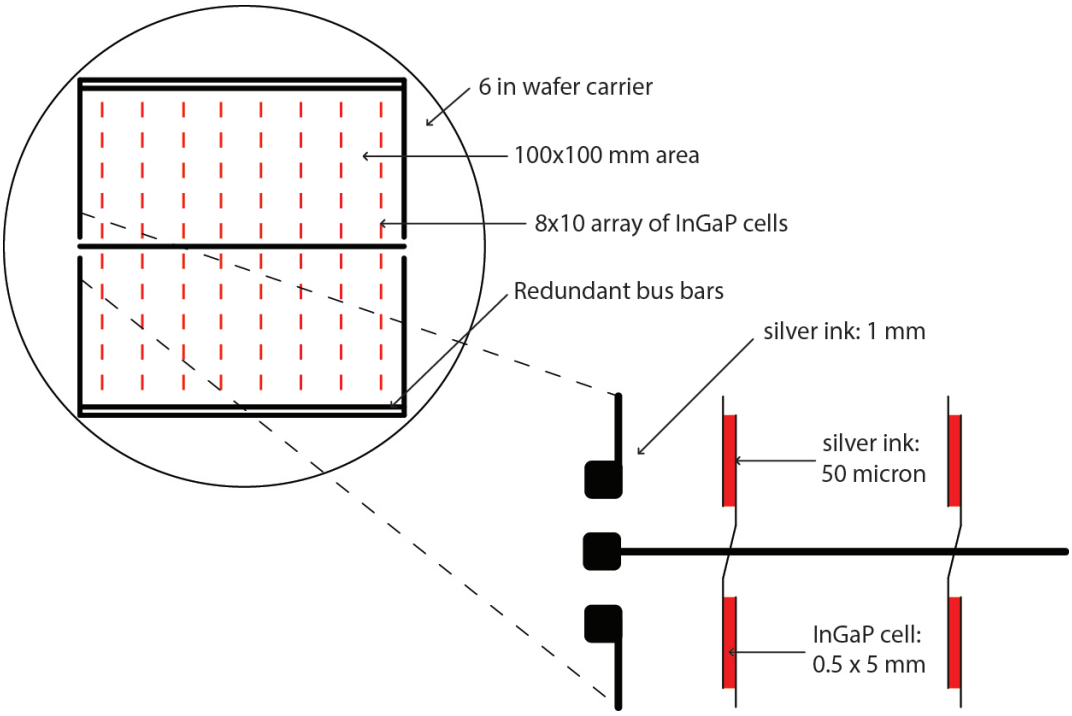

Figure 5.3: PV cell, interconnect, and bus bar layout on the 6 inch glass carrier wafer.

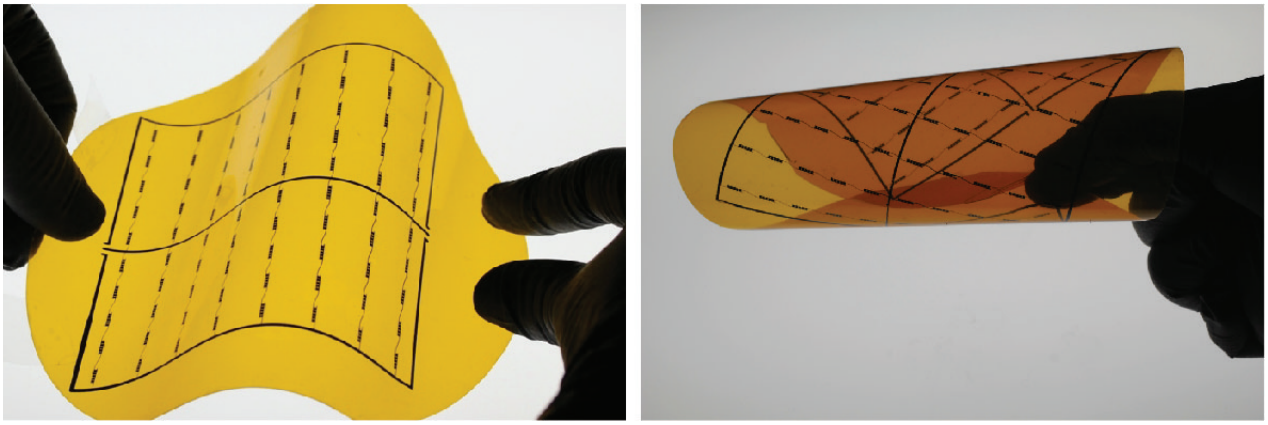

Figure 5.4: Un-mounted flexible PV microcell array after electrode printing and lamination with PDMS layer.

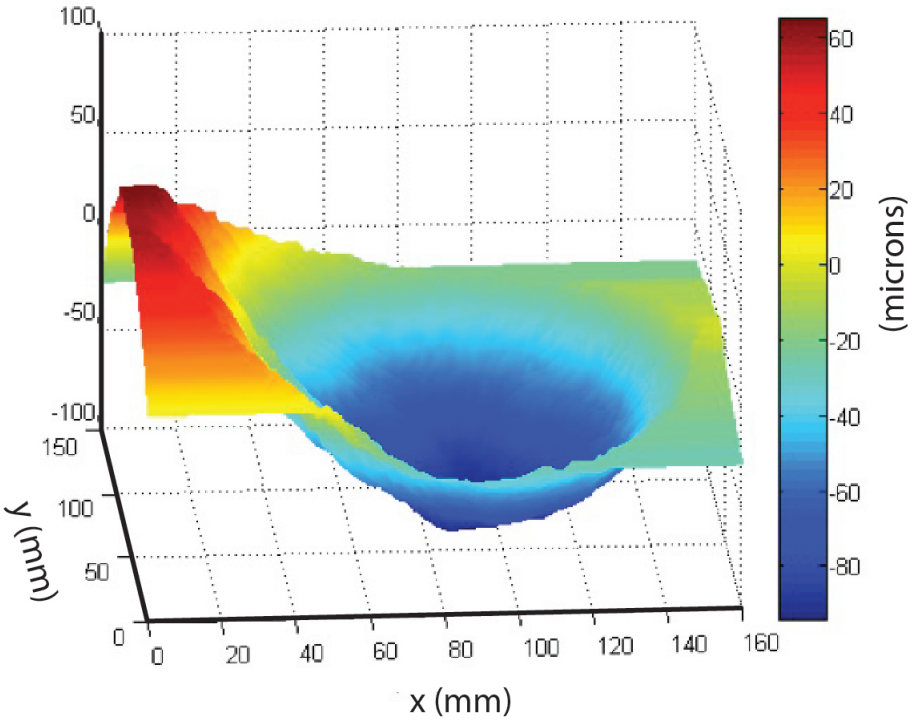

Figure 5.5: Optical profilometry scan of the laminated substrate. The glass carrier wafer has a concave shape and the pitch of the substrate spans 150 μm from the lowest to the highest point.

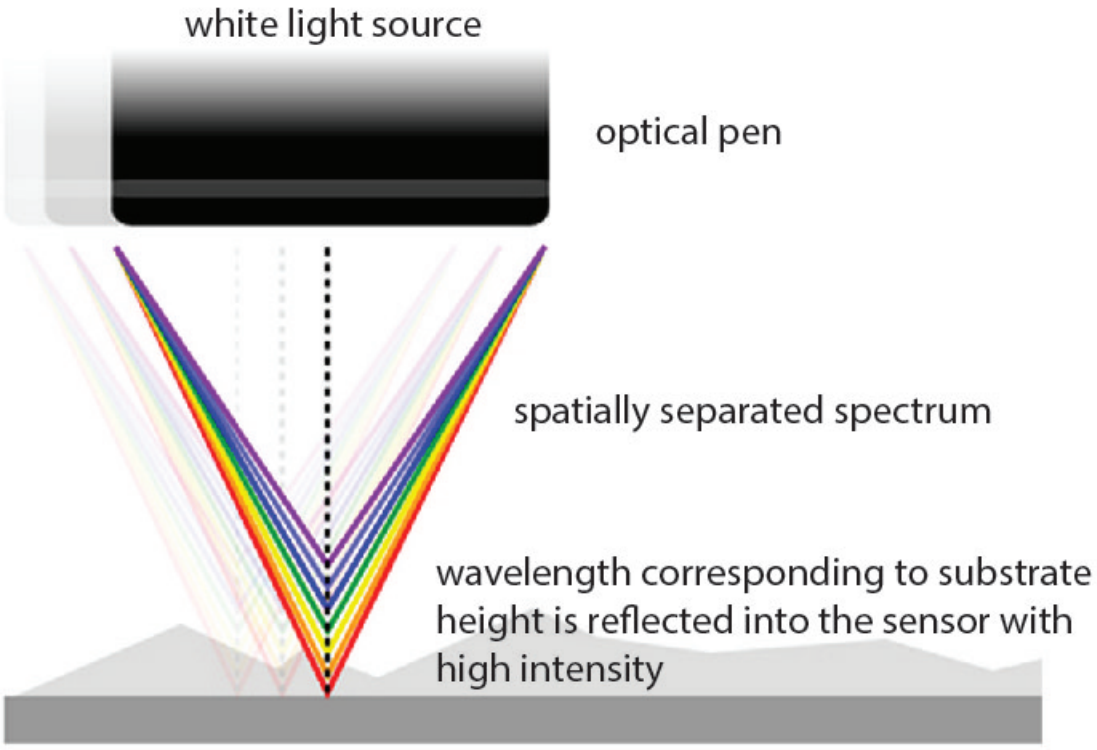

Figure 5.6: Chromatic confocal profilometry (Nanovea).

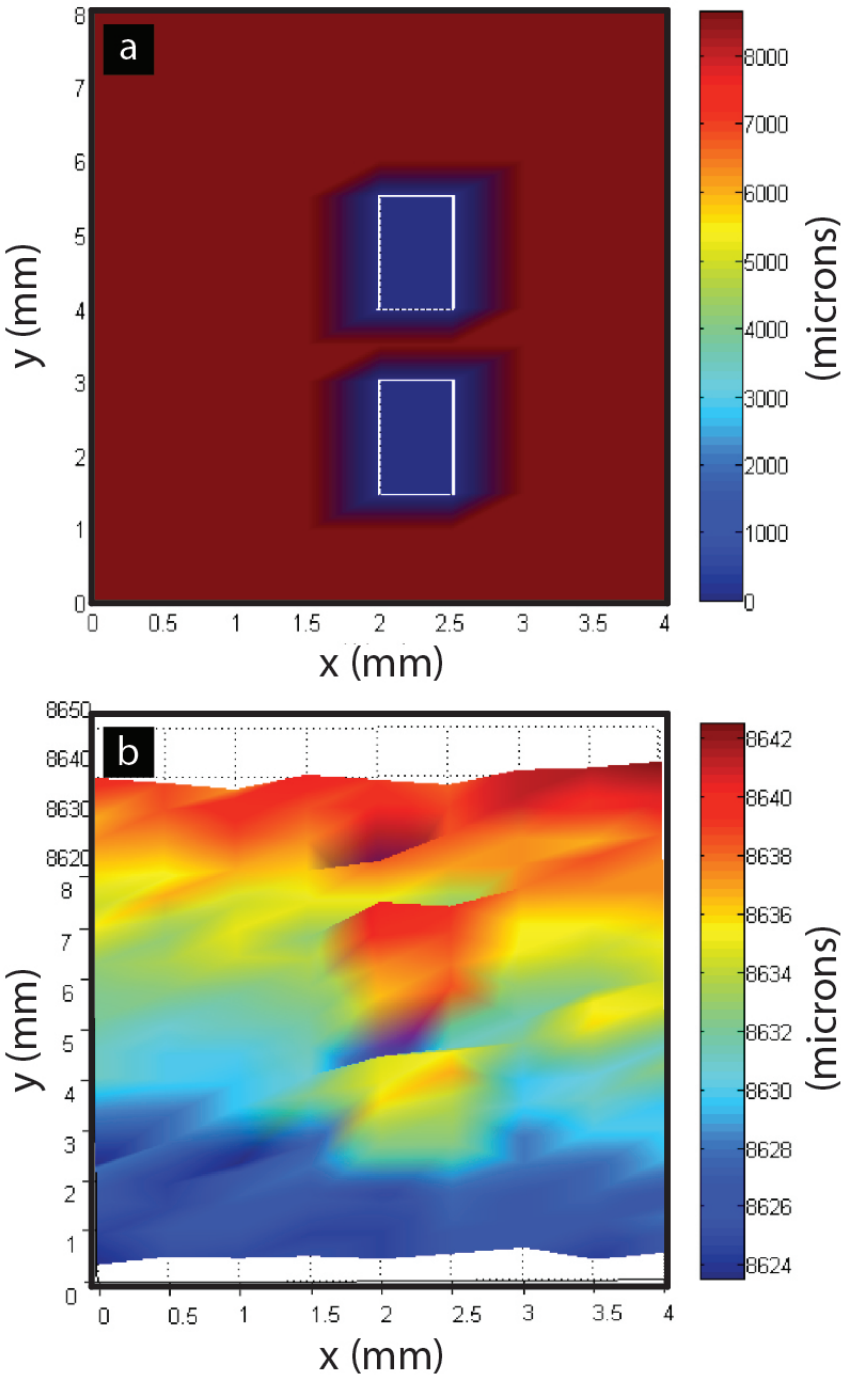

Figure 5.7: Optical scans of area over PV microcells. (a) On a first pass with the profilometer, data is not collected from the area over the PV cells; a value of 0 is inputted into the data matrix. (b) Afterwards, data is interpolated for the area covering the cells using the surrounding data points.

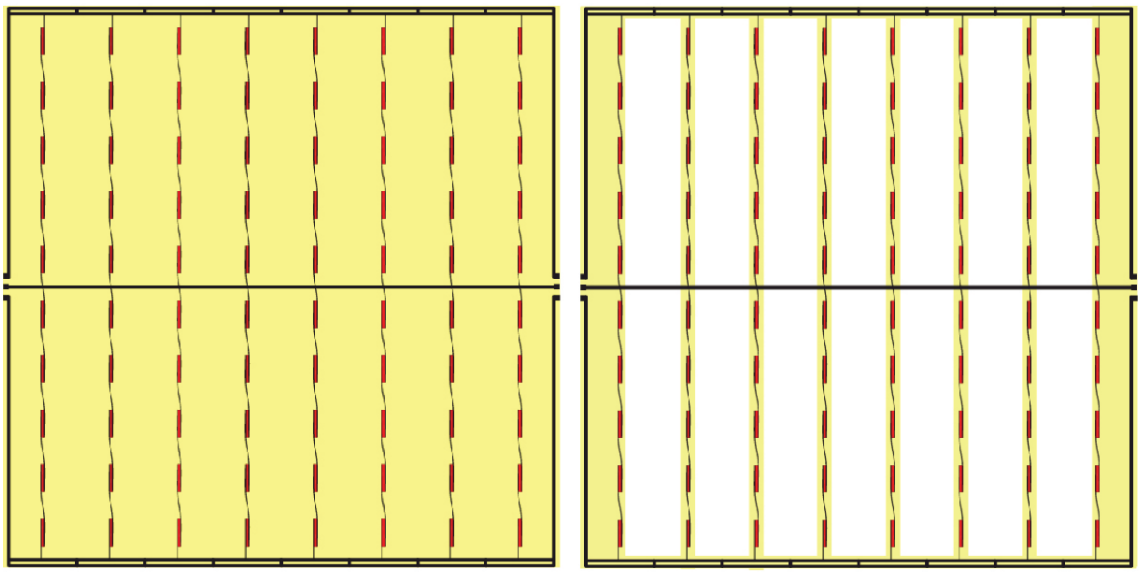

Figure 5.8: Optical profilometry patterns. Rastering the entire substrate requires a16 hour scan time. Selectively rastering over the printing areas reduces the scan time to 6 hours.

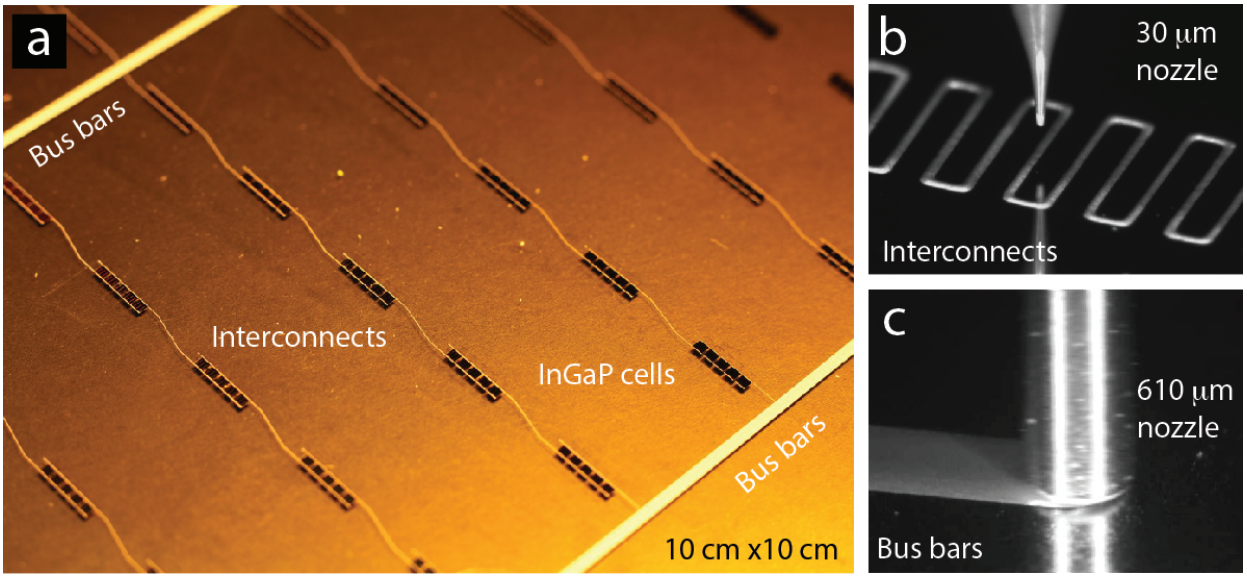

Figure 5.9: Solar cell array and direct ink writing images. (a) PV populated array wired with silver interconnects and bus bars. (b) Bus bar ribbons printed by a flat metal nozzle with 610 μm inner diameter and 1 mm outer diameter. (c) Narrow interconnects printed by a 30 μm glass nozzle.

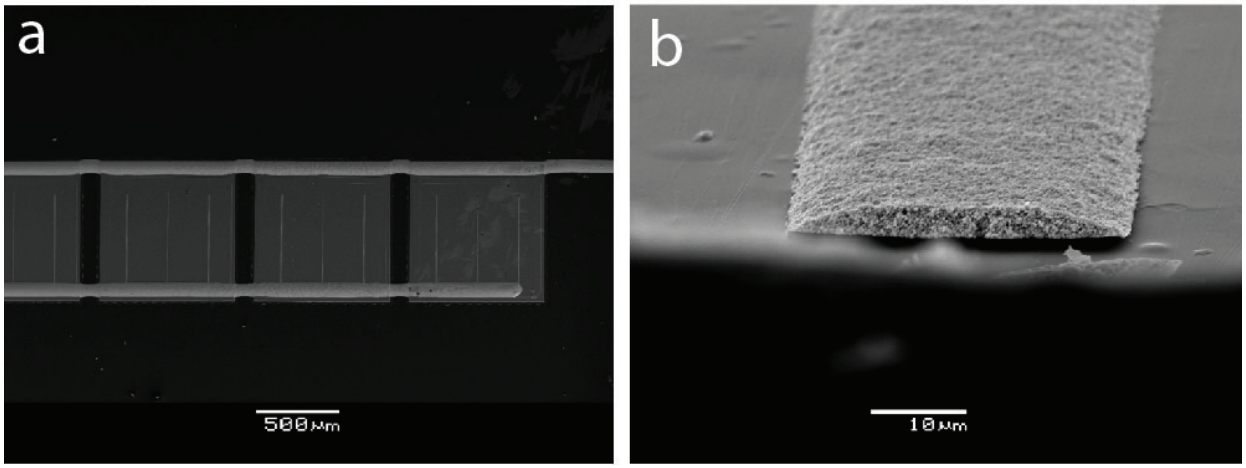

Figure 5.10: Printed silver interconnects. (a) Printed 50 μm interconnects on a PV cell. (b) Cross-section view of a printed silver interconnect trace.

Inner diameter	Outer diam. (mm)
0.10	0.24
0.20	0.42
0.33	0.65
0.61	0.91

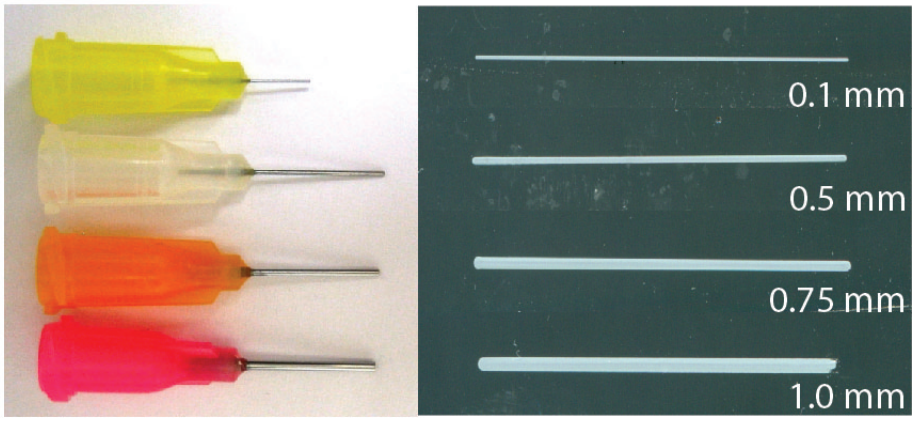

Figure 5.11: Printing with metal nozzles of various diameters (left). Shallow printing with wide-tipped nozzles (middle) result in ribbon-like traces in which the trace width (right), is approximately set by the outer diameter of the nozzle.

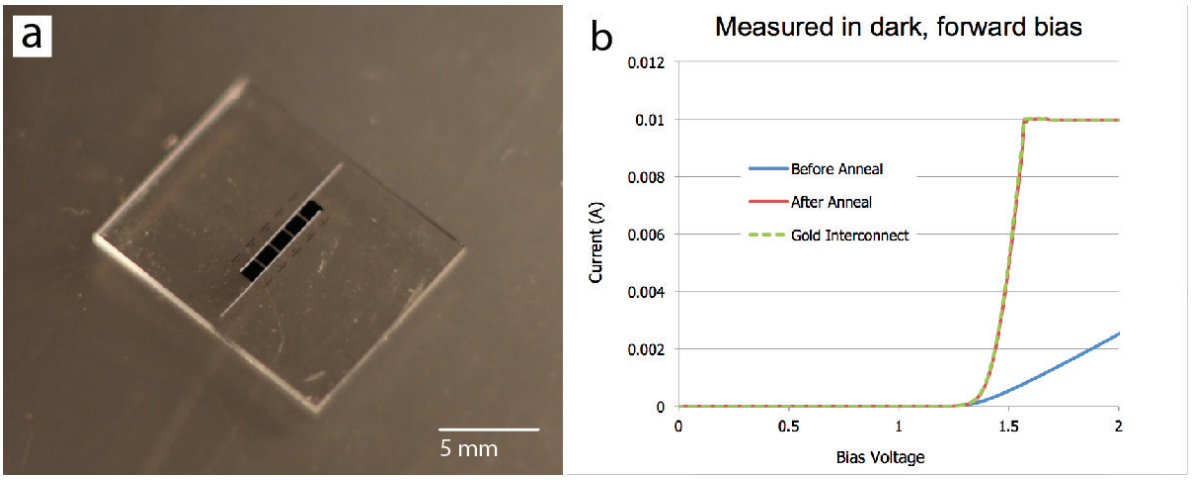

Figure 5.12: Solar cell measured in forward bias. (a) A test strip with a 1x5 array of PV cells. (b) Cells wired with annealed silver interconnects (175°C for 30 minutes) perform as well in forward bias as cells connected by sputter coated gold electrodes.

5.6 References

[1] Frederik C. Krebs, Mikkel Jrgensen, Kion Norrman, Ole Hagemann, Jan Alstrup, Torben D. Nielsen, Jan Fyenbo, Kaj Larsen, and Jette Kristensen. A complete process for production of flexible large area polymer solar cells entirely using screen printingfirst public demonstration. *Solar Energy Materials and Solar Cells*, 93(4):422–441, April 2009.

[2] Jongseung Yoon, Lanfang Li, Andrey V. Semichaevsky, Jae Ha Ryu, Harley T. Johnson, Ralph G. Nuzzo, and John A. Rogers. Flexible concentrator photovoltaics based on microscale silicon solar cells embedded in luminescent waveguides. *Nature Communications*, 2:343, June 2011.

[3] A. A. Earp, G. B. Smith, P. D. Swift, and J. Franklin. Maximising the light output of a luminescent solar concentrator. *Solar Energy*, 76(6):655–667, 2004.

[4] A. J. Chatten, K. W. J. Barnham, B. F. Buxton, N. J. Ekins-Daukes, and M. A. Malik. Quantum dot solar concentrators. *Semiconductors*, 38(8):909–917, August 2004.

[5] Francesco Meinardi, Annalisa Colombo, Kirill A. Velizhanin, Roberto Simonutti, Monica Lorenzon, Luca Beverina, Ranjani Viswanatha, Victor I. Klimov, and Sergio Brovelli. Large-area luminescent solar concentrators based on /'stokes-shift-engineered/' nanocrystals in a mass-polymerized PMMA matrix. *Nature Photonics*, 8(5):392–399, May 2014.

[6] Makoto Tsubokawa and Shinjo Tateyama. A novel fiber-optic light concentrator with scattering parts. *Ieice Transactions on Electronics*, E97C(2):93–100, February 2014.

[7] Michael G. Debije, Christopher Menelaou, Laura M. Herz, and Albertus P. H. J. Schenning. Combining positive and negative dichroic fluorophores for advanced light man-

agement in luminescent solar concentrators. *Advanced Optical Materials*, 2(7):687–693, July 2014.

[8] Igor Coropceanu and Moungi G. Bawendi. Core/shell quantum dot based luminescent solar concentrators with reduced reabsorption and enhanced efficiency. *Nano Letters*, 14(7):4097–4101, July 2014.

[9] Xing Sheng, Ling Shen, Taehwan Kim, Lanfang Li, Xinran Wang, Ryan Dowdy, Paul Froeter, Kazuki Shigeta, Xiuling Li, Ralph G. Nuzzo, Noel C. Giebink, and John A. Rogers. Doubling the power output of bifacial thin-film GaAs solar cells by embedding them in luminescent waveguides. *Advanced Energy Materials*, 3(8):991–996, August 2013.

[10] Andrea L. Rodarte, Fredy Cisneros, Linda S. Hirst, and Sayantani Ghosh. Dye-integrated cholesteric photonic luminescent solar concentrator. *Liquid Crystals*, 41(10):1442–1447, October 2014.

[11] Steve Collins, Dominic C. O'Brien, and Andrew Watt. High gain, wide field of view concentrator for optical communications. *Optics Letters*, 39(7):1756–1759, April 2014.

[12] Noah D. Bronstein, Lanfang Li, Lu Xu, Yuan Yao, Vivian E. Ferry, A. Paul Alivisatos, and Ralph G. Nuzzo. Luminescent solar concentration with semiconductor nanorods and transfer-printed micro-silicon solar cells. *Acs Nano*, 8(1):44–53, January 2014.

[13] Chun-Chao Chen, Letian Dou, Jing Gao, Wei-Hsuan Chang, Gang Li, and Yang Yang. High-performance semi-transparent polymer solar cells possessing tandem structures. *Energy & Environmental Science*, 6(9):2714–2720, August 2013.

[14] Sung Yeon Heo, Jong Kwan Koh, Gumin Kang, Sung Hoon Ahn, Won Seok Chi, Kyoungsik Kim, and Jong Hak Kim. Bifunctional moth-eye nanopatterned dye-sensitized solar cells: Light-harvesting and self-cleaning effects. *Advanced Energy Materials*, 4(3):1300632, February 2014.

[15] Jung Woo Leem, Sehwan Kim, Soo Hyun Lee, John A. Rogers, Eunkyoung Kim, and Jae Su Yu. Efficiency enhancement of organic solar cells using hydrophobic antireflective inverted moth-eye nanopatterned PDMS films. *Advanced Energy Materials*, 4(8):1301315, June 2014.

[16] Chia-Hsing Liu, Pei-Lun Niu, and Cheng-Kuo Sung. Integrating anti-reflection and superhydrophobicity of moth-eye-like surface morphology on a large-area flexible substrate. *Journal of Physics D-Applied Physics*, 47(1):015401, January 2014.

[17] Ju-Hyeon Shin, Yang-Doo Kim, Hak-Jong Choi, Sang-Woo Ryu, and Heon Lee. Multifunctional SiO2 moth-eye pattern for photovoltaic applications. *Solar Energy Materials and Solar Cells*, 126:1–5, July 2014.

[18] Asa Asadollahbaik, Stuart A. Boden, Martin D. B. Charlton, David N. R. Payne, Simon Cox, and Darren M. Bagnall. Reflectance properties of silicon moth-eyes in response to variations in angle of incidence, polarisation and azimuth orientation. *Optics Express*, 22(5):A402–A415, March 2014.

[19] Kyoo-Chul Park, Hyungryul J. Choi, Chih-Hao Chang, Robert E. Cohen, Gareth H. McKinley, and George Barbastathis. Nanotextured silica surfaces with robust superhydrophobicity and omnidirectional broadband supertransmissivity. *ACS Nano*, 6(5):3789–3799, May 2012.

[20] Brian Derby. Inkjet printing of functional and structural materials: Fluid property requirements, feature stability, and resolution. *Annual Review of Materials Research*, 40(1):395–414, 2010.

CHAPTER 6

CONCLUSIONS

The Pen-on-Paper (P-o-P) electronics platform is an intuitive, low-cost approach to patterning circuits on paper. Central to this approach is the creation of conductive silver and resistive carbon inks for rollerball pen that have highly tunable rheological and electrical properties. P-o-P electronics are well suited for applications ranging from STEM education to prototyping of complex circuit boards and programmable devices. This conductive silver ink, when concentrated, is also suitable for direct writing of fine electrodes (50 μm) and wide bus bars (1 mm) for flexible photovoltaic devices. The key findings are summarized below:

(i) A water-based silver microparticle ink is synthesized that enables printing of high conductivity features, approximately 1% the conductivity of bulk silver, at ambient conditions. Stripping the silver particles of their polymer capping agent (PAA) via a sequence of washing steps is critical to ensuring high conductivity. Annealing to modest temperatures (175°C for 30 min) yields ink traces with an electrical resistivity of 3.5×10^{-5} Ω-cm.

(ii) The viscosity of silver inks can be tuned over a wide range (0.1 to 100 Pa-s) to enable printing by rollerball pen and direct ink writing. At shear rates relevant for these patterning approaches, the ink viscosity is well fitted by a power-law model for fluid viscosity. Under these same conditions, the pure HEC solutions exhibit a linear dependence on concentration (when the HEC content is below 1 vol%) and a power law dependence with an exponent of ~ 4.0 (when the HEC content is between 1-8 vol%). It is found that both the silver solids loading and the HEC viscosifier content have a strong influence on the rheological properties, however the HEC-water carrier fluid dominates the rheological properties.

(iii) Carbon nanoparticle resistive ink is developed for printing passive components (resistors) in flexible circuit boards. The conductivity is six orders of magnitude lower than that of the silver ink ($\sim$200 Ω-cm). In addition, carbon and silver inks can be blended in various ratios to yield composite inks with highly tunable resistivity between that of pure inks. The ink blends can be used for rollerball pen and direct ink writing.

(iv) Conductive silver and resistive carbon inks have been optimized for use with rollerball pens. The flow behavior of silver inks is studied by directly imaging the formation of an ink meniscus at the trailing edge of the ball tip during printing. We find that a balance between viscous and surface forces determines the shape of the meniscus as well as the morphology of the printed trace. Specifically, the threshold printing speed at which a change in meniscus shape occurs corresponds to $Ca \sim 0.1 - 0.4$, depending on which ink viscosity (initial or partially dried) is used in the analysis. This behavior is akin to the classic printers instability in roller-based printing systems.

(v) The effect of the paper surface texture on printed line morphology and conductivity was studied. On standard copy paper, the ink wicks through the paper fibers resulting in a rough trace border. On the other hand, semi-gloss photo paper quickly wicks the water through micropores in the surface coating. This rapid wicking pins the edges of the printed trace, resulting in a uniform outline. In addition, the conductive particle mat lies entirely on the top surface of the paper, resulting in significantly higher conductivity traces compared to those printed on copy paper. Semi-gloss photo paper is used as a model paper for meniscus formation studies as well as an ideal substrate for many P-o-P devices.

(vi) We have demonstrated numerous applications for P-o-P Electronics including electronic art, high and low-pass filters (incorporating carbon ink resistors and paper capacitors), LED displays, capacitive touch pads, and programmable circuit boards.

(vii) Finally, direct writing of silver particle inks enables creation of interconnects (<50 μm) and bus bars (1 mm) to wire an array of PV microcells on polyimide. By mapping the substrate topography using optical profilometry, we successfully demonstrate conformal printing of silver electrodes on substrates with highly non-uniform surfaces.

APPENDIX A

"PAPERDUINO"

by Analisa Russo and Michael A. Bell (2013)

A.1 Bill of Materials

Materials

- Conductive ink pen
- Silhouette SD plotter
- Magnet-terminated cables
- FTDI cable
- USBtinyISP bootloader or pre-bootloaded Arduino chip
- Gel superglue or Z-tape

Software

- EAGLE PCB software
- ARDUINO IDE
- Silhouette Studio

Electrical Components (surface mount)

- 2x 10 μF capacitors (1206 package)
- 3x 0.1 μF capacitor (1206)
- 2x 10 KΩ resistors (1206)
- 330 Ω resistor (1206)
- ATmega328P-AU

- Red LED (1206)
- Green LED (1206)
- 5V voltage regulator (5 pin)
- 8 MHz resonator
- Tactile switch

A.2 Editing the Layout in EAGLE

Our Paperduino design is based on the open source design for the Arduino Pro Mini. We used EAGLE PCB to design the board. The board schematic can be downloaded from the Arduino website. The board layout and schematic are shown in **Figure A.1**.

Adapting the board for paper

In order to make the schematic paper-friendly, we replaced the blocks of pin headers with our own custom round pad. Through-hole components such as the pin headers are difficult to use on flexible surfaces like paper. Since the pen plotter only prints lines, but not fill patterns, the pads were composed of overlapping concentric circles. The tool path for plotting will be shown in Step 3.

We also replaced the package for many of the small components with the 1206 package (meaning 1.2mm long x 0.6mm wide) so they would be easier to mount later on.

Designing the board layout

In the board layout, we set the top layer line width to 0.6 mm to match the width of the pen trace.

We designed the board layout so the Paperduino could be printed on one layer. In many cases, the surface mount components act as jumpers. It is important to keep components close together to minimize line resistance between them.

In EAGLE PCB, the component pads will not be filled in by the pen plotter when exported as a DXF – only the outlines will be drawn. To solve this issue, overlay the pads with meandering line features so they will be filled by a raster pattern.

Finally, if any lines require a paper jumper (like our digital pins 1, 2, and 3), they can be created in the bottom layer (blue). After the first layer is printed, paper stickers can be place over the lines and the bottom DXF layer can be used to print over the stickers.

A.3 Export the Board Layout

Before exporting the board as a DXF file, only have the top layer (red) selected in EAGLE. If you have more than the top layer selected you may end up drawing more on the board then you desire. If you'd like to create text, vector fonts can be printed out on the pen plotter. If you use the tnames layer to separate traces and text, then select both the top layer and tnames before exporting the DXF file.

When prompted after selecting export as DXF (file – export – DXF), deselect the wire width and fill area options and then save the file to the appropriate directory.

A.4 Import Layout to Silhouette Studio

Import the file

Import the DXF file into Silhouette Studio by dragging the file onto the blank page. You can see that all of the pads are composed of either raster line patterns or concentric circles. The imported file is shown in **Figure A.2**

Adjust the layout

After importing the DXF file to Silhouette Studio, it may need to be rescaled. Go back to the EAGLE board layout and measure the pattern from top to bottom. Then "select all" in Silhouette Studio and rescale the pattern to match. Next, position the Arduino pattern on the page where desired.

Select print settings

Open up the plotting window. If you aren't using a cutting mat, that option can be de-selected. A printing speed of 1 (the slowest speed) works well. Glossy photo paper can be used with a thickness level 15. Finally, make sure the "sketch pen" option is selected.

A.5 Print the Arduino

Getting the plotter ready

To prepare the Circuit Scribe for plotting, wrap the pen in masking tape, then wedge it into the plotter head and lock it. Load the plotter with glossy photo paper, which will enhance the conductivity of the ink, compared to standard paper. This step is represented in **Figure A.3**.

Printing

Now simply hit "cut" in Silhouette Studio! The tool path that Silhouette Studio creates tends to double over most of the lines. This is to our advantage – drawing over the traces twice reduces their electrical resistance.

A.6 Placing Components

Method 1: superglue

Place a drop of superglue between the component pads. It's ok if glue gets on one of the traces that runs between the pads. Then carefully place a component with tweezers and press in the center. This placement method is shown in **Figure A.4**.

This method is permanent and the connection between components and pads should be good. However, we sometimes reinforce the connections using conductive epoxy applied with a syringe or an electric fluid dispenser. The fully populated and programmed board is shown in **Figure A.5**.

Method 2: z-axis tape

Place a strip of z-axis tape over several of the component pads. Then press the surface mount components in place. The components could be peeled up later and reused. This is by far the quickest and easiest method to attach components.

A.7 Burning the Arduino Bootloader and Programming

Burning the Arduino bootloader

An Arduino chip isn't ready to program straight from Atmel's factory (the company that makes the microcontrollers)! In order to get the ATMEGA328 to run any Arduino sketches, the Arduino firmware has to be loaded in a process known as bootloading (akin to loading an operating system such as Windows 7). There are a many programmers available, but we use a USBtinyISP from Adafruit. First connect 5 pads on the Paperduino (GND, VCC, MOSI, MISO, SCK and DTR) to the programmer. Once connected, select the correct board type in Arduino IDE (an Arduino Pro Mini 328 at 5V), and then click "burn bootloader." If it works, the bootloader will be uploaded.

Uploading a sketch to the Paperduino

Our Arduino does not have an FTDI chip built on the board. The FTDI essentially bridges the gap between USB and the serial communication of the ATMEGA328 chip. What we need is the simple FTDI chip, which can be found packaged in a USB cable, and purchased from Sparkfun. In future versions of the Paperduino we'll actually integrate an FTDI chip and make a paper USB connector to plug directly into a USB port on your computer.

Once you have the FTDI cable in hand, the connection is simple. Wire up the GND, VCC, TXD, RXD and DTR to the appropriate spots on the cable. Once wired, all you have to do is upload a sketch. Uploading the blink example will blink the green surface mount LED.

We uploaded a simple sketch that changes the direction of a magnetic bi-direction LED component from blue to green. Using two digital outputs, the direction is changed easily by making output 6 low, and 7 high. And to reverse, make output 6 high and 7 low.

A.8 Figures

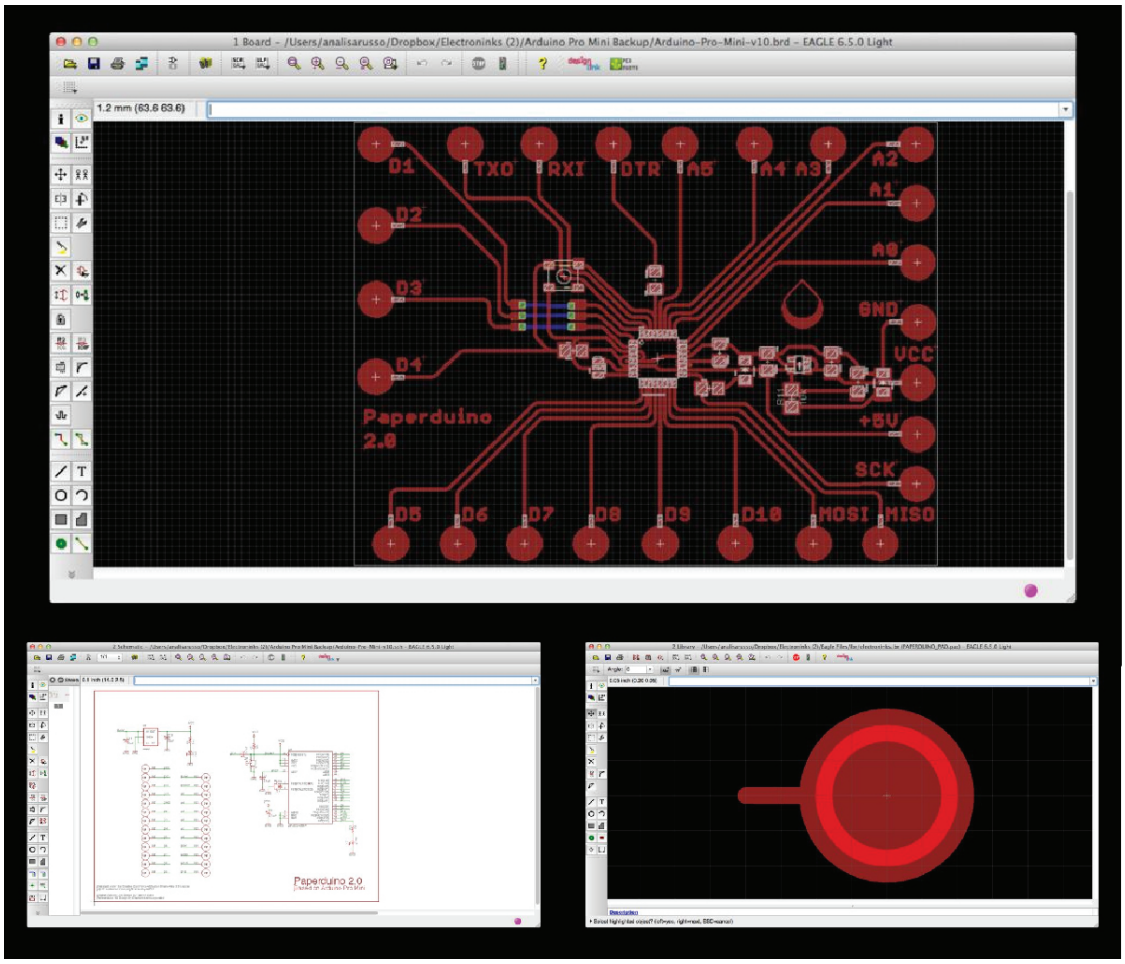

Figure A.1: Arduino Pro Mini board schematic and layout in EAGLE Cad.

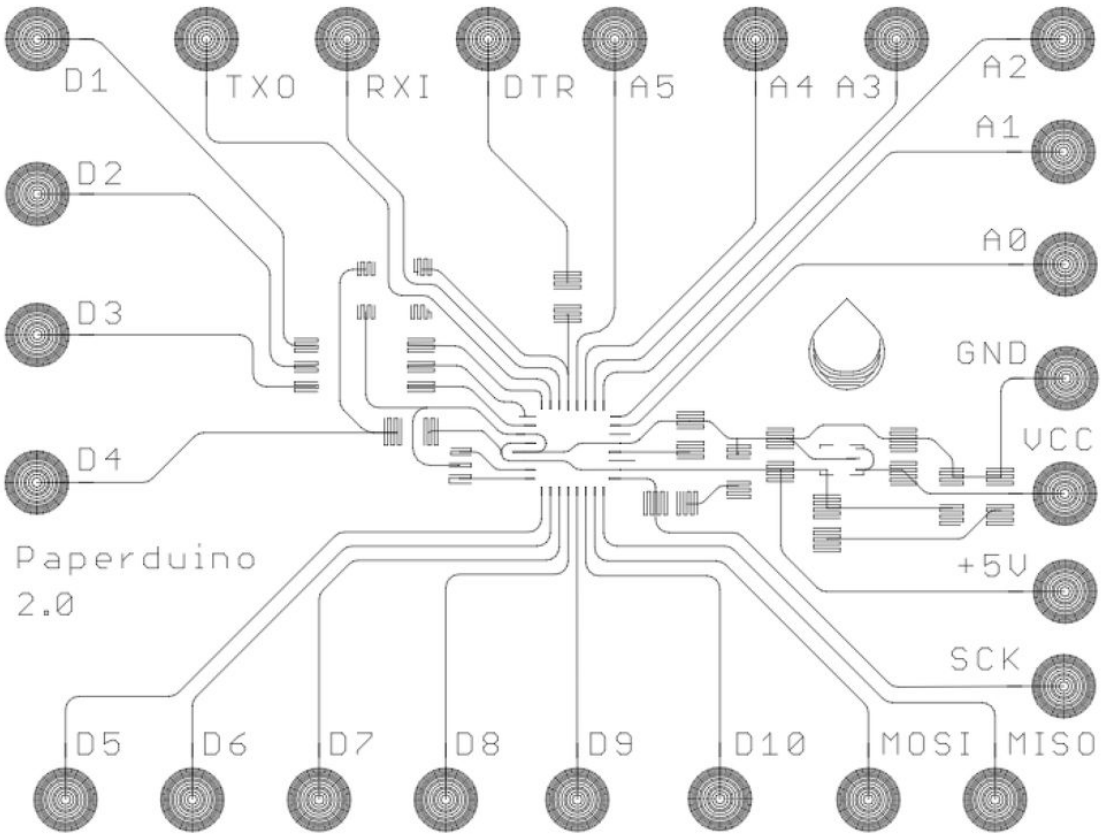

Figure A.2: Paperduino board layout in Silhouette Studio

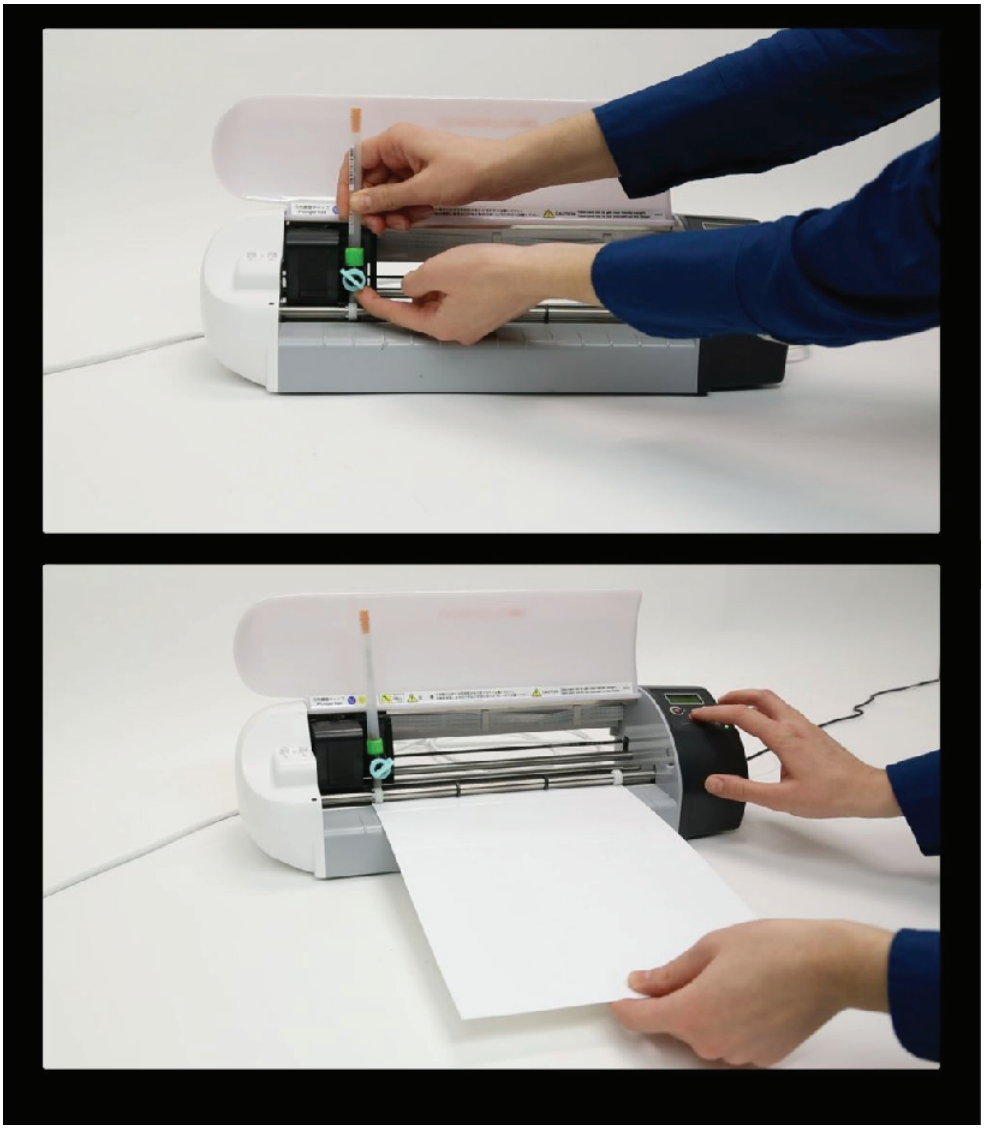

Figure A.3: Loading pen and paper into the Silhouette pen plotter.

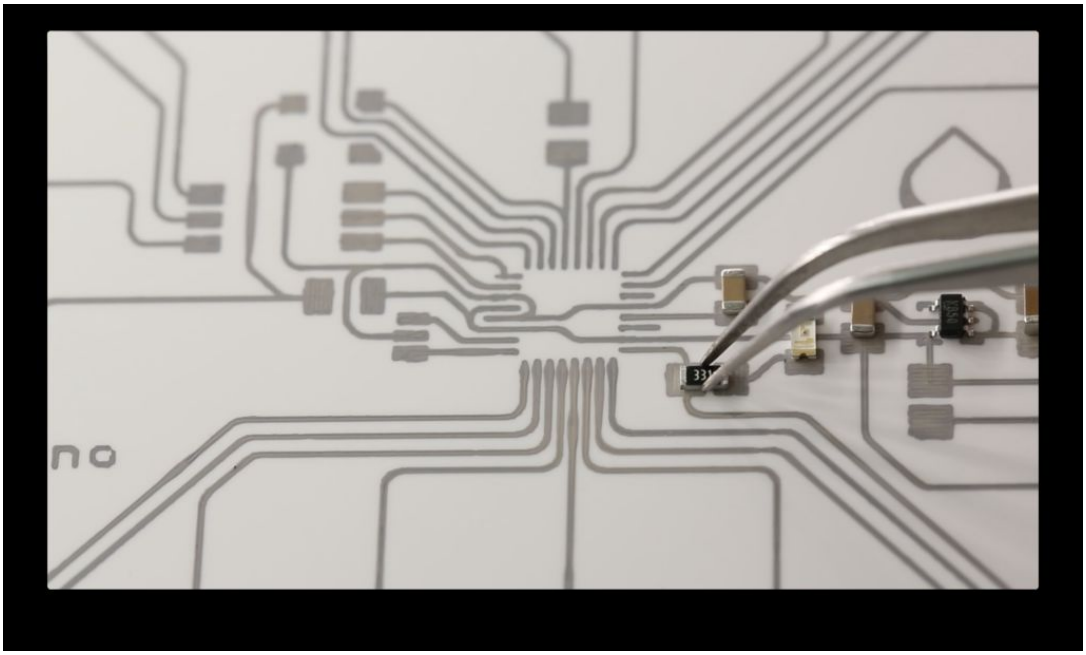

Figure A.4: Populating the Paperduino with surface mount components using a drop of superglue between electrodes.

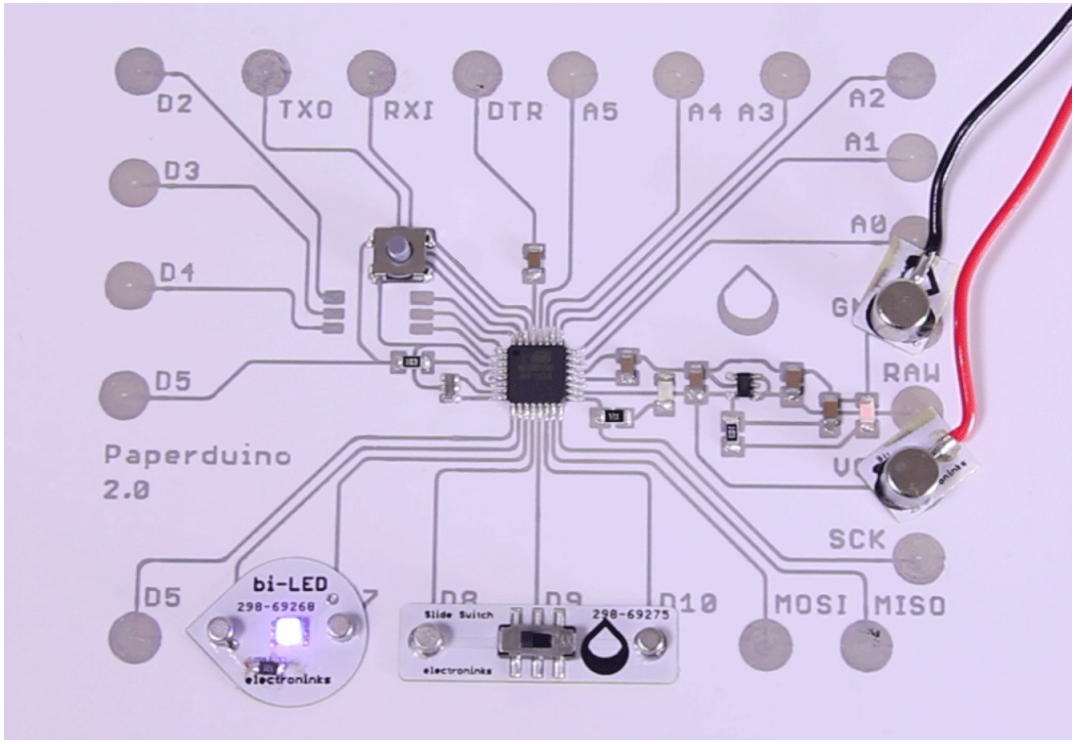

Figure A.5: The programmed board.

APPENDIX B

ARDUINO CODE FOR TOUCHPAD AND DISPLAY

The following instructions correspond to the 8×8 LED display and 5-segment capacitive touch pad described in **Chapter 4.** The devices are controlled using an Arduino MEGA board.

B.1 Pin Mapping

Display

The display is composed of an 8×8 grid of LEDs that are individually addressed using 8 ground pads and 8 power pads. The pin mapping is shown in **Figure B.1**.

Touchpad

The touch pad cable terminates in a row of 10 pin headers. Each of the 5 segments of the touchpad are connected to two pins: the "send" pin, which has a 10 kΩ resistor in series, and the "receive" pin, which contains no resistor. The mapping for the send and receive pins for each capacitive key is shown in **Figure B.1**.

Listing B.1: Touchpad Arduino Code

```
#include <CapacitiveSensor.h>


CapacitiveSensor cs_51_53 = CapacitiveSensor(51, 53);
CapacitiveSensor cs_47_49 = CapacitiveSensor(47, 49);
CapacitiveSensor cs_43_45 = CapacitiveSensor(43, 45);
CapacitiveSensor cs_39_41 = CapacitiveSensor(39, 41);
CapacitiveSensor cs_35_37 = CapacitiveSensor(35, 37);

int hpin[8] = {52,50,48,46,44,42,40,38};
int vpin[8] = {36,34,32,30,28,26,24,22};
int x=3;
int y=3;


void setup() {
  cs_51_53.set_CS_AutocaL_Millis(0xFFFFFFFF);
  cs_47_49.set_CS_AutocaL_Millis(0xFFFFFFFF);
  cs_43_45.set_CS_AutocaL_Millis(0xFFFFFFFF);
  cs_39_41.set_CS_AutocaL_Millis(0xFFFFFFFF);
  cs_35_37.set_CS_AutocaL_Millis(0xFFFFFFFF);

  for (int thisPin = 0; thisPin <  8 ; thisPin++) {
    pinMode(vpin[thisPin], OUTPUT);
    digitalWrite(vpin[thisPin],LOW);
  }
  for (int thisPinx = 0; thisPinx < 8; thisPinx++) {
```

```
28      pinMode(hpin[thisPinx], OUTPUT);
29      digitalWrite(hpin[thisPinx], HIGH);
30    }
31
32    Serial.begin(9600);
33 }
34
35
36 void loop(){
37
38    long A =   cs_51_53.capacitiveSensor(53);
39    long B =   cs_47_49.capacitiveSensor(49);
40    long C =   cs_43_45.capacitiveSensor(45);
41    long D =   cs_39_41.capacitiveSensor(41);
42    long E =   cs_35_37.capacitiveSensor(37);
43
44    if (A > 100 && B > 80 && C < 80 && D < 80 && E < 50){
45      for (int thisPin1 = 0; thisPin1 <  8 ; thisPin1++) {
46        digitalWrite(vpin[thisPin1],LOW);
47      }
48      for (int thisPinx1 = 0; thisPinx1 < 8; thisPinx1++) {
49        digitalWrite(hpin[thisPinx1], HIGH);
50      }
51
52      digitalWrite(hpin[0],LOW);
53      digitalWrite(hpin[1],LOW);
54      digitalWrite(vpin[7],HIGH);
55      digitalWrite(vpin[6],HIGH);
56    }
```

```
57  else if (A > 100 && B < 80 && C < 80 && D < 80 && E < 50 ){
58    for (int thisPin1 = 0; thisPin1 <  8 ; thisPin1++) {
59        digitalWrite(vpin[thisPin1],LOW);
60    }
61    for (int thisPinx1 = 0; thisPinx1 < 8; thisPinx1++) {
62      digitalWrite(hpin[thisPinx1], HIGH);
63    }
64
65    digitalWrite(hpin[0],LOW);
66    digitalWrite(hpin[1],LOW);
67    digitalWrite(vpin[3],HIGH);
68    digitalWrite(vpin[4],HIGH);
69  }
70  else if (A > 100 && B < 80 && C < 80 && D < 80 && E > 50){
71     for (int thisPin1 = 0; thisPin1 <  8 ; thisPin1++) {
72       digitalWrite(vpin[thisPin1],LOW);
73     }
74     for (int thisPinx1 = 0; thisPinx1 < 8; thisPinx1++) {
75       digitalWrite(hpin[thisPinx1], HIGH);
76     }
77
78     digitalWrite(hpin[1],LOW);
79     digitalWrite(hpin[0],LOW);
80     digitalWrite(vpin[0],HIGH);
81     digitalWrite(vpin[1],HIGH);
82  }
83  else if (A < 100 && B > 80 && C < 80 && D < 80 && E < 50){
84    for (int thisPin1 = 0; thisPin1 <  8 ; thisPin1++) {
85      digitalWrite(vpin[thisPin1],LOW);
```

```
86      }
87      for (int thisPinx1 = 0; thisPinx1 < 8; thisPinx1++) {
88          digitalWrite(hpin[thisPinx1], HIGH);
89      }
90
91      digitalWrite(hpin[3],LOW);
92      digitalWrite(hpin[4],LOW);
93      digitalWrite(vpin[7],HIGH);
94      digitalWrite(vpin[6],HIGH);
95    }
96    else if (A < 100 && B < 80 && C > 80 && D < 80 && E < 50){
97      for (int thisPin1 = 0; thisPin1 <  8 ; thisPin1++) {
98        digitalWrite(vpin[thisPin1],LOW);
99      }
100     for (int thisPinx1 = 0; thisPinx1 < 8; thisPinx1++) {
101       digitalWrite(hpin[thisPinx1], HIGH);
102     }
103
104     digitalWrite(hpin[3],LOW);
105     digitalWrite(hpin[4],LOW);
106     digitalWrite(vpin[3],HIGH);
107     digitalWrite(vpin[4],HIGH);
108   }
109   else if (A < 100 && B < 80 && C < 80 && D < 80 && E > 50){
110     for (int thisPin1 = 0; thisPin1 <  8 ; thisPin1++) {
111       digitalWrite(vpin[thisPin1],LOW);
112     }
113     for (int thisPinx1 = 0; thisPinx1 < 8; thisPinx1++) {
114       digitalWrite(hpin[thisPinx1], HIGH);
```

```
115     }
116
117     digitalWrite(hpin[3],LOW);
118     digitalWrite(hpin[4],LOW);
119     digitalWrite(vpin[0],HIGH);
120     digitalWrite(vpin[1],HIGH);
121   }
122   else if (A < 100 && B > 80 && C > 80 && D > 80 && E < 50){
123     for (int thisPin1 = 0; thisPin1 <  8 ; thisPin1++) {
124       digitalWrite(vpin[thisPin1],LOW);
125     }
126     for (int thisPinx1 = 0; thisPinx1 < 8; thisPinx1++) {
127       digitalWrite(hpin[thisPinx1], HIGH);
128     }
129
130     digitalWrite(hpin[7],LOW);
131     digitalWrite(hpin[6],LOW);
132     digitalWrite(vpin[7],HIGH);
133     digitalWrite(vpin[6],HIGH);
134   }
135   else if (A < 100 && B < 80 && C < 80 && D > 80 && E < 50){
136     for (int thisPin1 = 0; thisPin1 <  8 ; thisPin1++) {
137       digitalWrite(vpin[thisPin1],LOW);
138     }
139     for (int thisPinx1 = 0; thisPinx1 < 8; thisPinx1++) {
140       digitalWrite(hpin[thisPinx1], HIGH);
141     }
142
143     digitalWrite(hpin[7],LOW);
```

```
144     digitalWrite(hpin[6],LOW);
145     digitalWrite(vpin[3],HIGH);
146     digitalWrite(vpin[4],HIGH);
147   }
148   else if (A < 100 && B < 80 && C < 80 && D > 80 && E > 50){
149     for (int thisPin1 = 0; thisPin1 <  8 ; thisPin1++) {
150       digitalWrite(vpin[thisPin1],LOW);
151     }
152     for (int thisPinx1 = 0; thisPinx1 < 8; thisPinx1++) {
153       digitalWrite(hpin[thisPinx1], HIGH);
154     }
155
156     digitalWrite(hpin[6],LOW);
157     digitalWrite(hpin[7],LOW);
158     digitalWrite(vpin[0],HIGH);
159     digitalWrite(vpin[1],HIGH);
160   }
161   else{
162     for (int thisPin1 = 0; thisPin1 <  8 ; thisPin1++) {
163       digitalWrite(vpin[thisPin1],LOW);
164     }
165     for (int thisPinx1 = 0; thisPinx1 < 8; thisPinx1++) {
166       digitalWrite(hpin[thisPinx1], HIGH);
167     }
168   }
169
170   delay(10);
171
172 }
```

B.3 Figure

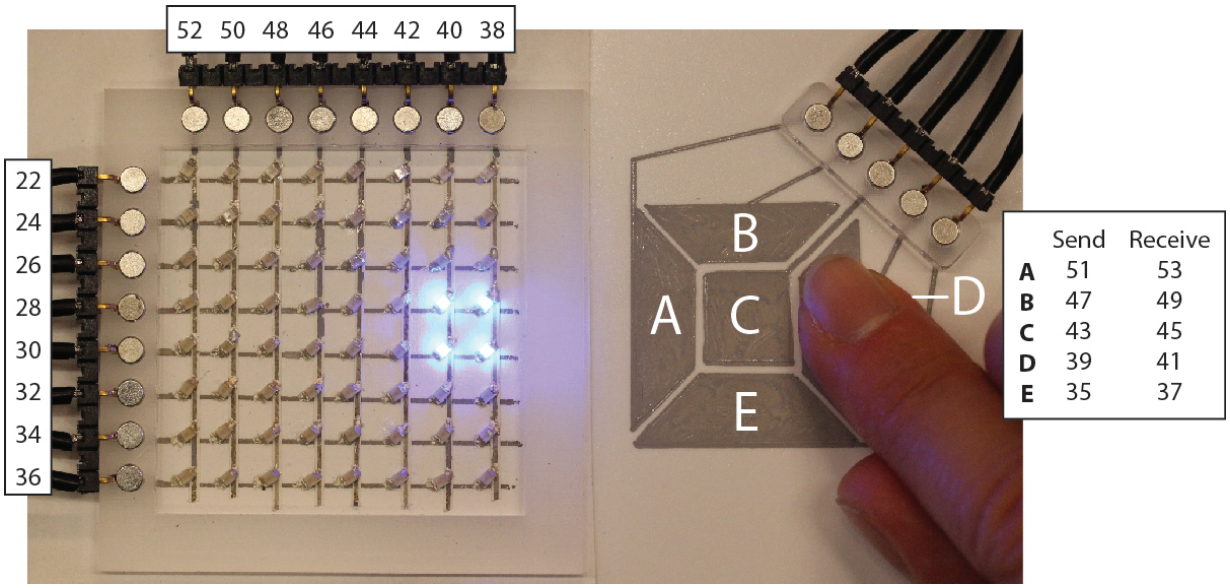

Figure B.1: Pin mapping for programmable display and touchpad.